# ANALYSIS OF LASER CLAD REPAIRED TI-6AL-4V FATIGUE LIFE

A Thesis

Submitted to the Faculty

of

Purdue University

by

Samuel J. Noone

In Partial Fulfillment of the

Requirements for the Degree

of

Masters of Aeronautics and Astronautics

December 2019

Purdue University

West Lafayette, Indiana

# THE PURDUE UNIVERSITY GRADUATE SCHOOL
# STATEMENT OF THESIS APPROVAL

Dr. Michael D. Sangid, Chair

School of Aeronautics and Astronautics

Dr. Alten Grandt

School of Aeronautics and Astronautics

Dr. Tyler N. Tallman

School of Aeronautics and Astronautics

**Approved by:**

Dr. Gregory A. Blaisdell

Head of the School Graduate Program

ACKNOWLEDGMENTS

- Dr. Michael Sangid, Purdue University, advice and direction throughout
- Dr. Kevin Walker, Defence Science and Technology Group, specimen preparation, fatigue simulations and general advice
- Royal Australian Air Force and Defence Aviation Safety Authority for support and funding
- Dr. Igor Switala, Defence Science and Technology Group, laser slotting of specimens
- Yi-Rye Choi, Royal Melbourne Institute of Technology, laser cladding of specimens
- Dr. Simon Barter, Royal Melbourne Institute of Technology, advice on Marker Band techniques
- Ritwik Bandyopadhyay, Purdue $ACME^2$ research group, for assistance throughout
- Greg Scofield, Purdue $ACME^2$ research group, for assistance throughout
- Imad Hanhan, Purdue $ACME^2$ research group, for assistance throughout
- Jun-Sang Park, Advanced Photon Beam, for assistance and technical advice
- Andrew Chihpin Chuang, Advanced Photon Beam, for assistance and technical advice

- Use of the Advanced Photon Source was supported by the US Department of Energy, Office of Science, Office of Basic Energy Sciences, under contract No. DE-AC02-06CH11357.

TABLE OF CONTENTS

Page

# LIST OF FIGURES

Figure Page

Figure Page

# ABSTRACT

Noone, Samuel J. MSAAE, Purdue University, December 2019. Analysis of Laser Clad Repaired Ti-6Al-4V Fatigue Life. Major Professor: Michael Sangid.

Laser cladding is a more recent approach to repair of aviation components within a damage tolerant framework, with its ability to restore not simply the geometric shape but the static and fatigue strength as well. This research analysed the fatigue performance of Ti-6Al-4V that has undergone a laser clad repair, comparing baseline specimens with laser clad repaired, and repaired and heat treated specimens. First an understanding of the microstructure was achieved by use of BSE imagery of the substrate, clad repaired region and post heat treated regions. The substrate of the material was identified with large grains which compared to a repaired clad region with a much finer grain structure that did not change with heat treatment. Next, performance of the specimens under tensile fatigue loading was conducted, with the clad specimens experiencing unexpectedly high fatigue performance when compared to baseline samples; the post heat treated specimen lasting significantly longer than all other specimens. It is theorised that the clad may have contributed to an increase in fatigue resilience due to its fine microstructure, when compared to the softer, more coarse substrate. The heat treatment is likely to have relaxed any residual stresses in the specimens leading to a reduction in any potential undesirable stresses, without impacting the microstructure. Residual stress analysis using EDD was unproductive due to the unexpected coarse microstructure and did not provide meaningful results. Fractography using the marker-band technique was explored with some success, proving a feesable method for measuring fatigue crack growth through a specimen post failure. Unfortunately fatigue crack growth throughout the entire fatigue life was not possible due to the tortuous fracture surface and potentially due to the fine

micro-structure of the clad, resulting in interrupted marker-band formation. Future research shall expand on this work with a greater focus on residual stress analysis and its impact on fatigue.

# 1. INTRODUCTION

Aviation repair methodology has been an ever evolving practice seeking the greatest combination of cost, efficiency and safety. Early repair methodologies focused on safe life and fail safe methodologies, allowing for complete or partial component failure before repair or replacement; these systems often required over engineered components of excessive size and/or weight, or relied on the removal of components well before their useful life was consumed. In the modern era, with designs requiring much more lightweight and efficient structures, along with the acknowledgement that components will often be introduced to service with flaws existing from manufacture, a damage tolerance approach was founded. Whilst this damage tolerance approach allows structures to be pushed further towards their limit, carrying known damage of acceptable size with confidence, there is the issue of certain materials with a comparatively low tolerance for any size of defect; these materials are especially prevalent in high strength safety critical components. High strength safety critical components are often some of the most expensive components, and due to their small critical flaw size can be frequently retired from service well before reaching their intended design life, thus severely impacting sustainment costs and inflicting significant maintenance downtime.

In the overall scheme of aircraft operation the initial cost of an aviation system may often seem like the most significant investment an operator will incur; however what is often not completely understood is the cost of sustainment of these aircraft where the initial purchase cost can be a small percentage of total life cycle costs, especially when aircraft can be operated anywhere up to 90 years as is the case with the recently extended B-52 Strategic Bomber [1]. To minimise the impact of these costs profits must outweigh their burden, this is achieved through efficient use of aircraft relying on the ability to consistently turn-around flights; effectively the more time aircraft

spend on the ground the more money is lost. The most detrimental factor to this equation is the occurrence of unanticipated component unserviceability, this can be as a result of simple and common factors such as debris on the runway or a mistake by maintenance personnel. In order to counteract this, aviation companies ensure their warehouses are stocked with spare components throughout all their aircraft operating locations, many of which go underutilised and are only there in case of unexpected unserviceability. This is where effective repair strategies may reduce this overhead. The ability to repair an item on-site, and potentially on-aircraft, with laser cladding technology reduces the significant logistic overhead of managing the supply chain and supporting warehouses full of underutilized items, it also reduces the consumption of extremely expensive components over an aircraft, and its fleets, potential 90 year life, providing airline companies with a significant amount of potential profit retention.

This effect can be compounded in the military environment as aircraft are often operated away-base on operations and military deployments. Due to this, the majority of spares are maintained and stored at a single home-base location, whilst aircraft are operating throughout the world unsupported or with limited critical spares. When a component is noted as no longer within serviceable limits, due to unexpected damage or degradation (highly likely when operating on rudimentary desert runways or remote pacific islands), it is likely that a spare component may not be at the current away-base operating location. This results in the aircraft being grounded, leading to mission failure, or the aircraft being operated at an increased risk to aircrew, if the mission is critical. It is not practical or realistic to have every structural component with the aircraft at all times, however it would be highly practical to carry a specific set of tools which could replace a large portion of structural components. Laser cladding is a potential solution, where a set of repair methodologies could be certified across a range of structural components, where-by an aircraft technician deployed with the aircraft could conduct in-situ repairs as soon as damage or degradation is identified, returning the geometry and fatigue/static strength of the component, al-

lowing the aircraft to complete critical missions, enabling the generation of air power and potently preventing loss of life.

Titanium alloys are being utilized more consistently in the design of these high strength safety critical components, including engine components, landing gear systems and flight control support structure. The most widely used titanium alloy is Ti-6Al-4V, with a microstructure consisting of a low temperature hexagonal close-packed (hcp) $\alpha$ phase, which is stabilized by aluminium, and a high temperature body-centered cubic (bcc) $\beta$ phase, which is stabilized by vanadium [2]. The negative aspect of high strength materials, like titanium, is the limits of their acceptable flaw size. These flaws may begin from small discontinuities in the material produced in manufacturing, design inadequacies, scratches from in service damage, or degradation processes such as corrosion and fretting [3]. As stated earlier, once a flaw is introduced, either the component is removed from service or the life of the component is significantly reduced. Due to these factors there is a strong motivation to develop viable and cost-effective repair strategies; laser clad repairs are a more recent approach to aviation component repair. The benefits of laser clad repairs are that once the damage is removed from the component, the clad can return the component to its original geometric shape and may restore a significant portion of its fatigue life, assisting greatly with damage tolerant design.

## 1.1 Aim and Research Questions

There has been a dearth of research into Additive Manufacturing (AM) of aviation alloys, laser clad repairs for various mechanical advantages, even some initial considerations on how these repair methodologies perform in the fatigue environment. The potential of such a repair could reduce logistic management for aviation companies, reduce the amount of component wastage due to disposal of useful, yet damaged critical components, and may also lead to greater flexibility for commercial and military aviation in general. To reap these benefits a greater understanding regarding

the fatigue impact of these repairs on high strength alloys is required. This research intends to contribute to furthering validity of laser clad repairs on Ti-6Al-4V alloys in a fatigue environment. Specifically this is to be conducted through;

- utilizing Back Scatter Electron (BSE) imagery to understand the micro-structure of Ti-6Al-4V, and how this differs from substrate, through the heat affected zone of laser cladding, through the clad itself, and whether or not heat treatment has a significant impact;
- explore residual stress effects and it's impact on fatigue performance;
- tensile fatigue testing utilizing variation of constant amplitude to produce marker band patterns on the fracture surface and use this to formulate fatigue crack growth rates.

# 2. LITERATURE REVIEW

## 2.1 Laser Cladding

Considerable amount of research [4–8] has gone into the understanding of AM in general. AM's popularity is due to its high geometrical flexibility and ability to save both time and cost in comparison to conventional manufacturing technologies [4]. AM distinguishes itself from other processes which employ a form of subtraction in their respective methods i.e. machining. A branch of AM which can provide the same flexibility and cost saving effects of AM is Laser Cladding, with the additional attribute being that it can be applied to an already built and/or installed component.

The introduction of laser cladding as a technique coincided with the development of gas lasers in the 1970's which made laser welding and cutting a possibility [9]. By the time the 1980's arrived research at University of Illinois was being conducted into the development of laser surface alloying and laser surface cladding in order to increase properties such as resistance to wear, erosion, corrosion, and high-temperature oxidation [10]. During this time industry began utilizing laser cladding in turbine blade interlock shrouds and hard-facing of nickel-base alloy turbines [9].

Laser cladding has since been utilized across industry for many years, such-as the field of medicine where calcium phosphate is laser clad to titanium alloys in order to allow more effective bonding between human bone and high strength prosthetic implants [11]. The use of laser cladding in aviation has been limited to small, complex and expensive regions such as engine components, however its greater potential is starting to be recognised. An examples of this has occurred with certification on Australian Defence Force aircraft; these techniques include cold spray technology for repair of magnesium helicopter gear boxes and enhancing corrosion resistance of aluminum alloy components on fixed wing cargo aircraft [12]. In order for certification

of laser cladding in an increased variety of forms and utilizing a greater breadth of materials, further investigation and evidence is required. In regards to this, high strength steel has been an area of considerable focus [13–17], this is likely due to steel being one of the most used high strength materials in modern aviation. This trend is beginning to shift, with Ti-6Al-4V becoming a rapidly growing high strength material in aviation due to its far superior strength-to-weight ratio.

Research into Ti-6Al-4V in the field of laser cladding has been underway for some time, however the focus has primarily been cladding Ti-6Al-4V with other alloys in order to change mechanical properties i.e. improve surface wearing [18], microstructure [19] and hardness [20]. One of the primary concerns, and potential limitations of laser clad repairs in aviation, regards the fatigue life of laser clad products; it is lower than that of wrought material due to microstructure, porosity, surface finish and residual stress within the component [21]. The level at which this effects the fatigue life of the component overall still lacks complete understanding and thus merits further exploration.

The method of laser cladding requires the substrate to be prepared using a technique such as sandblasting, which improves surface bonding, followed by ultrasonic cleaning in order to remove surface contaminants. The clad material to be chosen can be either identical to that of the substrate for ideal bonding or another metallic alloy in order to achieve varying mechanical properties [22]. Compatibility of the laser clad is often considered the most important principle; the clad material and the substrate should have similar physical properties, such as the melting point, coefficient of thermal expansion and modulus of elasticity [22]. Too much distinction in melting point makes it difficult to achieve a metallurgical bond between the clad and substrate. Similarly, if the difference between coefficient of thermal expansion and modulus of elasticity is too large, then the residual stress will be significant, resulting in the formation of cracks and potential separation of the clad layer itself [22]. The material to be clad can be introduced as a powder, wire or strip to be melted onto the substrate and can be pre-positioned ahead of the laser beam or deposited by inert

gas coaxially with the laser beam. The material is then clad to the substrate in a back and forth pattern with the magnitude of layers based on desired depth, with an inert shielding gas utilized to prevent oxidation of the melt pool. Compared to conventional welding techniques laser cladding results in a considerably smaller depth of the melt zone resulting in a smaller heat-affected zone (HAZ) [23]. The case for the potential application of laser cladding technology to aircraft components is due not only to its relatively low HAZ, but also its flexibility, variety of filler materials and ease of automation [12].

Research has previously been conducted into laser cladding methods and techniques on Ti-6Al-4V, and how this impacts its feesability as a repair method [24]. In this process hypothetical damaged areas were removed via milling and then repaired with laser deposited material with a TRUMPF TruDisk 2.0 kW Yag laser. It was identified that smaller laser cladding tracks have faster cooling times which equates to smaller grain sizes and also require less shielding gas [24]. Titanium alloys have a high affinity to atmospheric gases and therefore any reduction in shielding gas requirements is beneficial. It has been shown that grain size and texture is the result of thermal conditions that exist early in the solidification of the laser clad, whilst fine-scale microstructure is affected by post-solidification cooling rates [25]. Research has conducted analysis into observed microstructures from Nd:YAG and CO2 laser cladding systems with average grain widths of 120 and 750 $\mu$m, respectively. The overall direction of growth of the grains was attributed to direction of laser travel and the direction of heat removal [25]. In the Nd:YAG deposits, the heat flow direction was affected by the laser movement, which was attributed to columnar grains in longitudinal sections of deposits; $CO_2$ deposits are not impacted by this and demonstrated grains perpendicular to the substrate (Figure 2.1). Laser power and traverse speed were significant contributors to grain width in deposited Ti-6Al-4V [25]. Grain width decreased with increasing traverse speed and increased with higher incident energy, which is expected as grain size is highly dependent on cooling rate (high power and

low speed results in high incident energy, which would give a low cooling rate; low power and high speed creates a high cooling rate) [25].

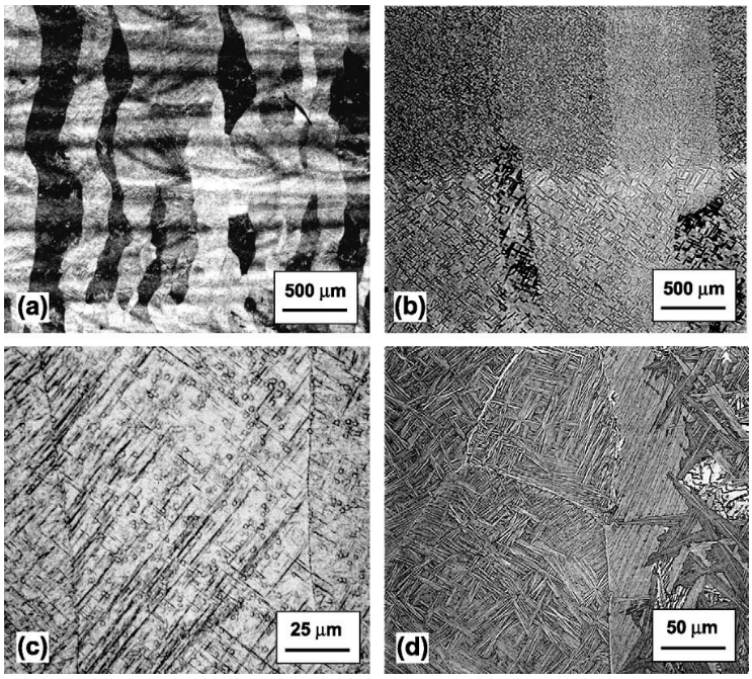


Fig. 2.1. Micrographs showing the (a, b) macrostructures and (c, d) microstructures of the Nd:YAG (a, c) and CO2 (b, d) laser deposits [25]

## 2.2 Residual Stress on Fatigue Crack Growth

Working of a material during repair or manufacture can lead to residual stresses embedded in the material, this change in residual stresses influences the fatigue behaviour of the material [26]. Residual compressive stresses improve, in general, the overall fatigue properties of service components, this is due to compressive stresses contributing to crack closure at the fatigue crack tip [27]. Methods to induce these beneficial compressive stresses have been studied [13, 28] with common methods used across general aviation repair being shot peening, an industry standard, and vibro-strengthening a more recent development, as examples [28]. Both these methods

utilize small granular particles impacting the surface to relieve/introduce near surface residual stresses. These techniques impact the surface and spread the material against the resistance of the adjacent material creating sub-surface residual stresses, often in compression. This initial compressive layer is followed by tension deeper into the material before returning to an equilibrium state [29]. It should also be noted the impact of such techniques when comparing different materials; softer material such as aluminum alloys can experience the plastic zone of peening being several times greater than the size of the particle impact; conversely higher strength steels will maintain a more consistent plastic zone relating to the particle impact size [30]. The benefit of the sub-surface compressive stresses and associated crack closure ef-

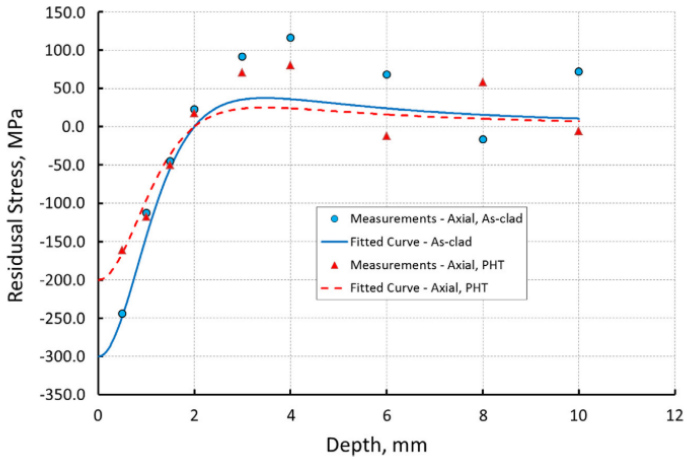


Fig. 2.2. Aermet 100 Residual Stress Example [13]

fect are generally considered to outweigh the tensile stresses experienced further into the material throughout an entire components fatigue life. This was highlighted by research into vibro-strengthening techniques concluding that compressive residual stresses introduced to a material can greatly increase fatigue life when compared to an unprocessed material which contain low levels of varying residual stresses from oscillation and machining [28]. Other research was done to separate whether the effects of working the material, and hence increasing hardness (strain hardening), being

the influential factor in increasing fatigue life; this research concluded that crack closure from residual stresses is the probable cause of life extension and not the strain hardening phenomena [27]. Additionally location of these stresses is crucial in their impact on crack closure; research found that shot peening regions ahead and adjacent to the crack tip had the greatest effect on retarding crack growth [27]. Research has also uncovered the significant role surface damage caused by peening can play in fatigue life, with such damage having the potential to reduce or reverse the benefits of residual stress imparted [29]. The advantage of laser clad repairs being that residual stresses can be introduce with much greater control of the surface finish, as cracks primarily nucleate from surface flaws.

As discussed, laser cladding is a laser surfacing technique with the primary aim to enhance the properties and/or regenerate the surface of a component [16], in the case of laser clad repairs the focus being to regenerate and return as much of the mechanical properties and geometry to the component as possible. Research has agreed on the impact and variability of laser clad fatigue performance based on the residual stresses formed during cladding and whether they are tensile (reduced fatigue life) or compressive (increased fatigue life) and their impact on initial crack growth rates [13, 16]. Research into laser cladding has identified that the process of heating up the substrate and applying powdered material via focused laser beam can leave residual stresses in the surface material and clad itself. In laser clad T-6Al-4V tensile residual stresses has been observed in the clad/substrate interface [31], and for Selective Laser Manufactured (SLM) specimens, it was considered likely that tensile residual stresses would occur in the clad specimen impacting fatigue [32]. Other research on Aermet 100 with laser clad repairs identified compressive residual stresses that significantly increased component fatigue life when compared to specimens that have been heat treated to reduce these same compressive stresses [13, 17]. Whilst residual stresses and their impact on fatigue has a dearth of research, understanding of how this transfers to a Ti-6Al-4V component that has undergone laser clad repair is still not completely explored.

## 2.3 Damage Tolerance for Laser Clad Designs

Management of aviation structures has been an ever evolving process based on lessons learnt post aviation accidents. Early methodologies focused on a Safe Life approach that relied on components which were either over-engineered for the task and considered to have an infinite life, or redundancies built into a structural system in order to carry catastrophic component failure and still operate with adequate safety. These methods had limited accountability for components which were introduced into service with manufacturing defects or material defects. During the 1960's a more comprehensive damage tolerance approach was introduced into mainstream aviation, with a focus on fracture mechanics principles [33]. These principles accounted for the expectation that crack nucleation was an assured outcome in each and every component regardless of expected life, with reliance being left solely on the ability to inspect, monitor and repair/replace any significant cracking before it became critical.

Laser cladding is a result of the damage tolerance approach, fulfilling the role of a modern repair technique for when damage is identified as being unacceptable for continued operations. Research by Defence Science and Technology (DST) Group has provided evidence of the effectiveness of the damage tolerance of laser clad repairs in Aermet 100 steel. During this study damaged AerMet 100 base-line material was tested to failure in a fatigue regime. Other damaged components had their defect removed and a clad layer was applied to return the geometric shape of the specimen. The result of this clad layer was to remove the surface damage, which as we have seen acts as a stress concentrator and a nucleation point for crack initiation. Further fatigue testing was performed on the repaired specimens and it was discovered that the laser-clad repaired components experienced a life more than four times longer than the damaged components [13, 17]. This was attributed to the ability to not only remove the the damage and associated stress concentrators, which currently is done in aviation as a primary repair, but to also introduce beneficial residual stresses and return the original component geometry [13, 17].

Laser cladding was reviewed regarding its use as a repair technique for aluminum alloy in corrosion and fatigue regimes [12]. Initial discussion in this research concerns the damage tolerance of laser cladding if the technique is not refined and understood. Using poor cladding parameters, primarily regarding laser power and scan speed, defects including cracks and porosity's can occur due to mechanical, thermal or metallurgical influences in the process. Additionally poor understanding of the impact of the HAZ in the substrate can lead to lower strength and brittleness [12]. Regarding the corrosive environment, the study provided evidence that HAZ was more susceptible to corrosion than the substrate, however the clad layer was more resistant to corrosion than both the HAZ and the substrate. Regarding the strength of clad specimens it was 79% of the substrate, while the fatigue life was much lower than that of the substrate [12]. The lower fatigue life is thought to be due to a weak interface between the clad and substrate and further work was recommended to understand these effects, and to improve the mechanical properties of clad specimens [12].

## 2.4 Marker Band Technique

Damage tolerance as discussed in the previous section, relates to the requirement to understand that components have existing defects before they are even introduced to service. Due to this, tracking of crack growth and understanding the rate at which it traverses through material based on known loads is crucial to the success of the damage tolerant design. Additionally the ability to track these crack growth rates during a fatigue experiment without interfering with the validity and consistency of said experiments is a crucial task in any experimental setup. It is not always possible to follow the progress of crack growth during a fatigue test program, and thus reliance may be heavily weighted on post-mortem analysis of crack growth. The quantitative characterizations of the fracture surface, Quantitative Fractography (QF), relies on the ability to match features discovered on the fracture surface with the loading history of the specimen [3].

A study into full cycle fatigue testing of aircraft utilised a marker-block of constant amplitude loading, in an otherwise random flight test load spectrum, in order to acquire fatigue crack growth data in aluminium alloy spar caps and wing skin rivets [34]. They found marker-blocks to be an effective method with a balance between severity of marker-blocks to gain more defined marks vs gentle enough to not impact the integrity of the tests. They recommend future research should be directed towards optimizing the clarity of the marker-blocks at acceptable crack lengths, while retaining the integrity of the loading effects [34]. SEM was used as the primary visual aid in this technique.

Comprehensive research was conducted regarding marker loads for quantitative fractography of fatigue cracks [3]. The initial consideration is how to create markers on a materials surface; this can be achieved through methods of adding overloads, underloads and/or adding varying constant amplitudes (CA) to a load spectrum in order to mark fatigue fracture surfaces. Additions of overloads can impact crack growth significantly, owing to its ability to contribute a period of retardation; an overload can add a large crack extension, however if this extension causes a change in the fracture mode, a reduction in crack closure behind the crack, or changes the damage state (plasticity) ahead of the crack, then following the period of accelerated crack growth the rate will eventually drop, resulting in a period of reduced crack growth [3].

Research conducted by NASA supports this overload argument; they tested pre-cracked 2024-T3 Aluminium Alloy under fatigue comparing overload stress vs constant amplitude stress ($S_{ol}/S_{max}$). Constant amplitude ($S_{ol}/S_{max} = 1.0$) failed, on average, at 30,700 cycles, increasing this ratio to 1.125 increased the average life to 52,800 (70% increase). This trend continued with an average fatigue life of 2,090,000 cycles at $S_{ol}/S_{max} = 2.0$, up until immediate failure at a ratio of 3.4 due to the considerable spike in load during the initial overload [35].

Research into underloads identified the initiation of complex fracture surfaces including ridges, depressions and fissures [36]. These features impact the formation

of slip bands which change the direction of the crack tip (Figure 2.3) which can either increase or slow the progression of the crack growth, making crack growth unpredictable [36].

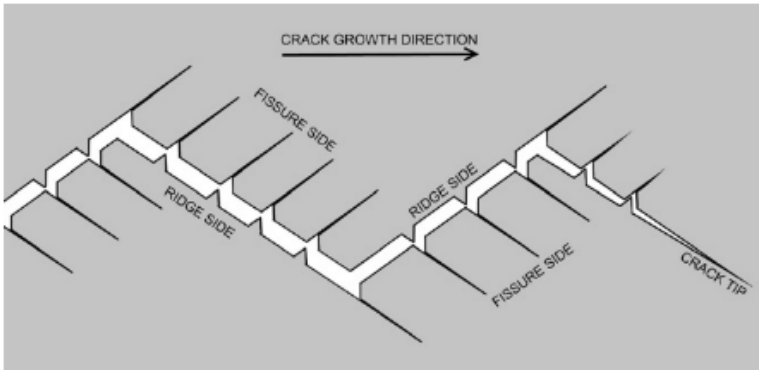


Fig. 2.3. Diagram of fissures created during underloads. Fissures and crack surface always point toward the crack tip [36]

For CA testing an effective overall strategy was grouping CA loads of differing R-values; if the R-value of a group is significantly different to the basic CA loading then this can be an effective strategy, as it provides the best visibility of marker bands [3]. Research of this effect into Ti-6Al-4V utilised marker bands of R = 0.65 - 0.85, it was determined titanium required higher R values than aluminium (R=0.5-0.7) for success, the Ti-6Al-4V produced occasional short segments across the crack front, whereas aluminium consistently produced markers across the entire crack front (Figure 2.4) [37]. This was attributed to relatively fewer available slip planes in Ti-6Al-4V crystalline structure and therefore providing fewer favourably orientated grains susceptible to marking [37]. Regarding impact on sample life, it was determined when comparing the total life of specimens marker-band vs specimens without marker-bands that there was not statistically significant difference for Ti-6Al-4V [37]. Another consideration into marker loads is that of the quantity of markers. Too little marks and crack growth rate cannot be confidently or accurately measured, too many and the detail can be too difficult to separate into quantifiable growth. This is dependent on the size of crack growth, size of component, and type of material i.e.

the finer the micro-structure the harder to distinguish markers as they deflect over the local fracture surface when cracks cross grain boundaries [3].

The next critical path is the ability to read these overloads/underloads off of the fracture surface. To be successful this can be done with macro-photography, high magnification optical microscopes or Scanning Electron Microscopes (SEM), depending on the markings size, spacing and contrast [3].

Another study [38] looked into using the marker band technique to determine short crack growth from a notch in 7449 alloy. The marker-band technique used in this study utilized blocks of low amplitude, high R-ratio cycles with a short sequence of overload and underload cycles during this block. The marker band crack front was irregular and the distance between the bands not constant, however by averaging the distance between fronts they were able to identify crack growth rates comparable to the macroscopic growth rate measured by optical methods on the specimen surface [38]. Crack growths were determined by measuring the distance between marker bands and then dividing by 10,000 (the amount of cycles between underloads) in order to identify distance/cycle. SEM was used as the primary visual aid in this technique.

DST Group conducted their own study on marker band techniques for AA7XXX alloys; they developed a CA test using two varying ranges of R to produce optical reflectors whilst ensuring the crack growth increment for each was below a desired 5% reduction in fatigue life or damage [39]. This formed the basis for previous studies on laser clad fatigue tests on Aermet 100 clad steel [13, 17] which produced successful and highly usable qualitative fractography results and shall be used in this study.

## 2.5 Fatigue Crack Growth Through Welds

Considerable research into the impact that welds have on the fatigue properties of materials has been conducted; aside from weld quality, research focuses on the heat

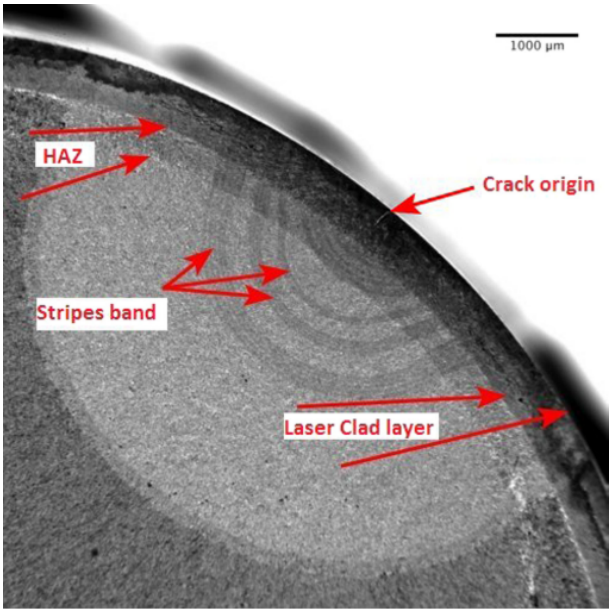


Fig. 2.4. Aermet 100 Marker Band Example [13]

effected zone (HAZ) produced from a weld, and the residual stresses and stress risers created through the welding process [40, 41].

Friction stir welding (FSW) is a process that utilizes heat generated by friction between a rotating tool and the workpiece material. This leads to a softened region near the tool, which while traversing along the joint mechanically intermixes the two pieces of metal, and forges the hot and softened metal by the mechanical pressure applied by the tool. During research into fatigue properties of 2050 alloy, it was found that crack propagation is linked with the presence of compressive residual stresses in the HAZ which induce crack closure. Where-as a combination of both tensile residual stress and change in microstructure elsewhere in the welded region was attributed to an increase in crack propagation [41]. FSW testing conducted on 2024-T351 found that the nugget region had a fine re-crystalisation grain structure with grains between 5$\mu$m and 10$\mu$m with the surrounding thermo-mechanically zone containing a significantly more coarse and soft grain structure with tensile residual stresses becoming more compressive towards the HAZ/Substrate transition [40]. Regarding fatigue

crack growth the observations were consistent with a crack closure based model in which compressive residual stress fields reduce $K_{eff}$, and tensile fields increase it. The research also determined that residual stresses had the highest impact when compared to local hardness and microstructure changes, which appeared to play a secondary role [40]. Laser cladding itself falls beneath the umbrella description of a weld in so far as a weld is the bonding of two material surfaces through fusion. Traditional repair processes, such as thermal spraying, plasma spraying, and traditional arc welding have deficiencies that laser cladding can help overcome, primarily, the significant reduction of heat affected zones (HAZ). Laser cladding is both confined and controlled regarding its heat input and is therefore very beneficial for repair of damaged high-value components [13]. Research comparing the damage tolerance of integrally machined stringer panels with welded joints found that for cracks initiating at the weld joint, the tensile residual stresses in the fusion and HAZ accelerated the fatigue crack growth rate significantly, even more so than integrally machined panels [42]. This area is where the advantages of the HAZ in laser cladding are critical; due to the significantly smaller HAZ and the potential residual stresses occurring in this surface, much of these negative aspects of welding are not experienced to the same degree.

## 2.6 X-Ray Diffraction

X-ray diffraction (XRD) works through the principle of diffraction of x-ray through a metallic lattice, more specifically the x-ray energies can be utilised in order to detect the inter-atomic lattice spacing within a crystalline sample through the interaction of the incident rays with the sample. XRD utilizes the relationship between lattice spacing $d_{hkl}$ and the diffraction line $E_{hkl}$. This is based on Bragg's Law which relates the variables of velocity (c), wavelength ($\lambda$) and incident angle ($\theta$) of light with Planck's Constant (h) and wavelengths per second (v) [43]. The sample is scanned through a range of $2\theta$ angles, this assesses all possible diffraction directions of the

lattice due to the random orientation of the powdered material, post this constructive interference can be analysed and a peak intensity (diffraction peak) is output. Conversion of the diffraction peaks to d-spacings allows identification of the material as each material has a set of unique d-spacings, this is achieved by comparison of d-spacings with standard reference patterns [43]. Crystal lattices in a material are theoretically identical, regarding size and spacing, however real life materials rarely follow this definition. One reason for these imperfections can be due to distortion of the crystal lattice which is assessed as a variation of d-spacing within the lattice due to micro-strain from applied or residual stresses [44]. The calculation of the lattice strain is:

$$\epsilon_{hkl} = \frac{d_{hkl}}{d_{0(hkl)}} - 1 = \frac{E_{0(hkl)}}{E_{hkl}} - 1 \tag{2.1}$$

This enables comparison and calculation of change in lattice spacing against the strain-free parameters in order to identify residual strain.

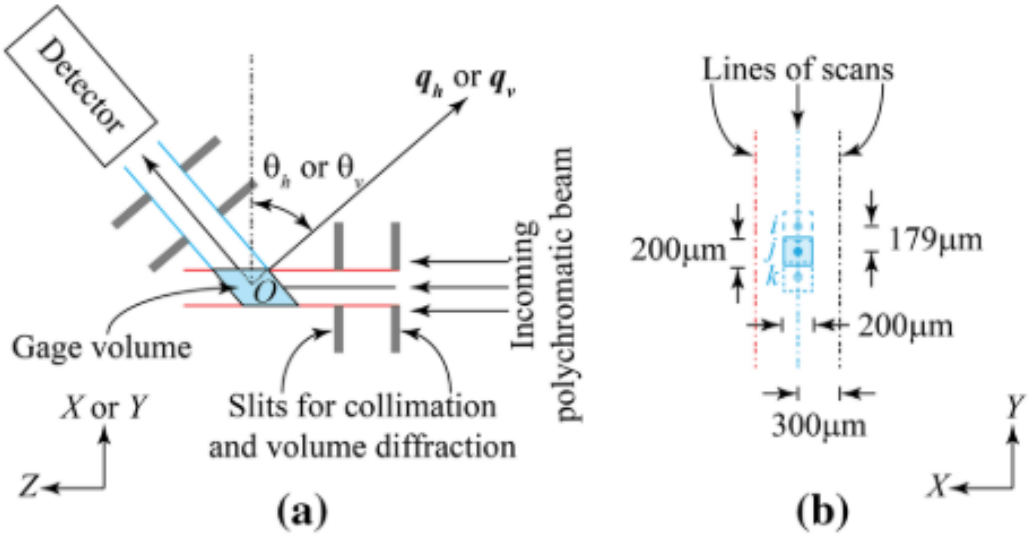


Fig. 2.5. EDD Experiment Setup [45]

Labratory x-ray diffraction equipment are a common use method for residual stress characterisation due to their ease of use and post-processing, however due to their

relative low energies, penetration on the order of tens of microns can only provide a small picture of the residual stresses occurring beneath the surface. Synchrotron x-ray sources can provide higher energies and higher brilliance providing deeper penetration, shorter collection times and finer spatial resolution [46].

Synchrotron power-diffraction experiments founded on energy dispersive diffraction techniques are around forty years old [47]; modern generation Energy Dispersive (X-Ray) Diffraction (EDD) is now in its 3rd generation and is a leading technique when it comes to residual stress analysis [47]. EDD utilizes X-rays generated by a cathode ray tube, filtered to produce monochromatic radiation, collimated to concentrate, and directed toward the sample being inspected.

EDD is of considerable benefit as a non-destructive residual stress measurement tool, this has the obvious advantage of preserving valuable specimens. Research into strain mapping experiments on bulk engineering components looked into fatigue crack in a 25 mm thick austenitic stainless-steel compact tension (CT) specimen, and in a titanium linear-friction weld (LFW), both scenarios have been considered unsuitable for other traditional techniques, such as neutron diffraction due to high spatial resolution required, and in regards to titanium specifically, as it is a relatively poor at scattering of neutron particles; EDD was able to accomplish strain mapping in both situations [48].

# 3. SPECIMEN DESIGN

## 3.1 Material Properties

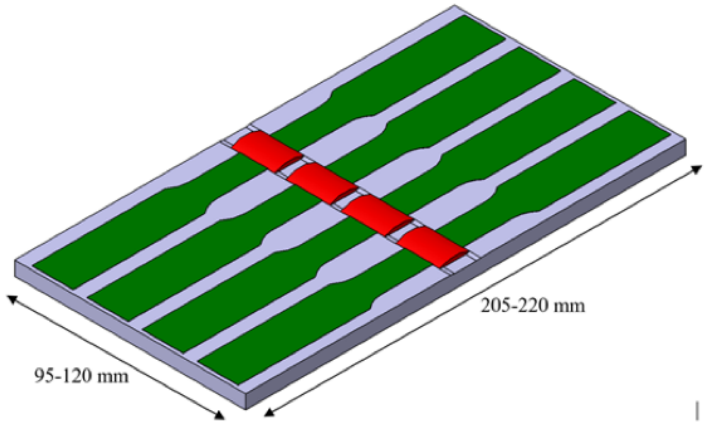


Fig. 3.1. Pre Machined Mock Up

The specimens utilized in this research were produced from a sheet of Ti-6Al-4V provided by the Royal Australian Air Force (RAAF). The supplied Ti-6Al-4V sheet was then sectioned into three separate sheets, each sheet had a groove machined into the surface in order to mimic damage removal, post this the laser clad was applied (Figure 3.1) mimicking a repair being conducted. Once the clad was applied the sheet was then cleaned up to remove excess clad and six dog-bone shaped samples were cut from each sheet. The sheet produced eighteen samples which were divided evenly into three test sets;

- set one acted as baseline; substrate material only, with three laser slots applied in the middle of the specimen,
- set two had the groove machined and the laser clad applied along with identical laser slots, and

- set three had the groove machined and the laser clad applied and then was heat treated to 480°C for 2 hours in order to relieve stress incurred during the cladding process before finally having laser slots applied to mimic a defect.

The samples were taking from various positions throughout the original sheet to reduce any influence the original sheet properties may contain.

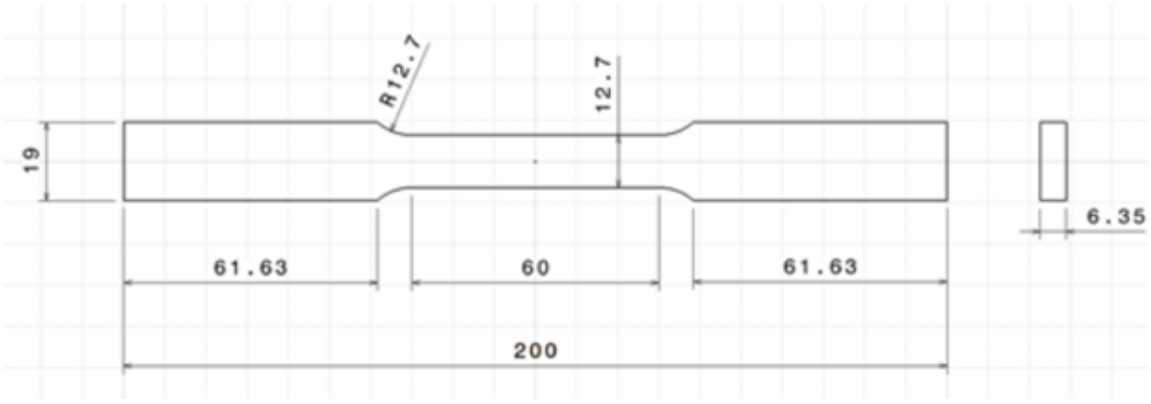


Fig. 3.2. Final Specimen Dimensions

### 3.2 Laser Clad

The laser clad was completed by Royal Melbourne Institute of Technology (RMIT) based on in-house experience. The technique utilized a TRUMPF TruLaser Cell 7020 system controlled by a Flapro CNC program which automates the pattern once mapped. The grooved surface was prepared by first sandblasting, which improves surface bonding, and then ultrasonically cleaned in order to remove surface contaminants. The powder was Ti-6Al-4V TLS TECHNIK with grain size of 45-90 $\mu$m, the carrier gas utilized was Helium (10L/min), and Argon was used as a shielding gas (16L/min) to minimize surface contamination during cladding. A 3.0 kW Fibre Beam was utilized at 8mm from the work piece with a 1.5mm beam diameter and 250mm focal length mirror. 12-Passes at 700W laser power were completed with a

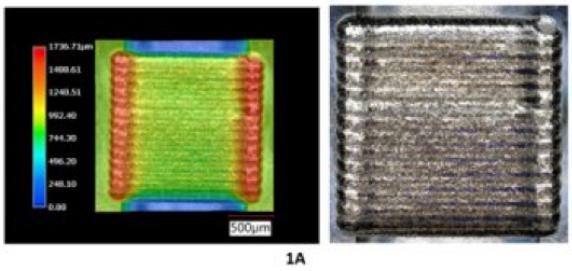


Fig. 3.3. Clad Height Map

600mm/min traverse speed and 2.3444 g/min powder flow. Between each pass the substrate was cooled to room temperate and a step over of 0.75mm was utilized as per Figure 3.4.

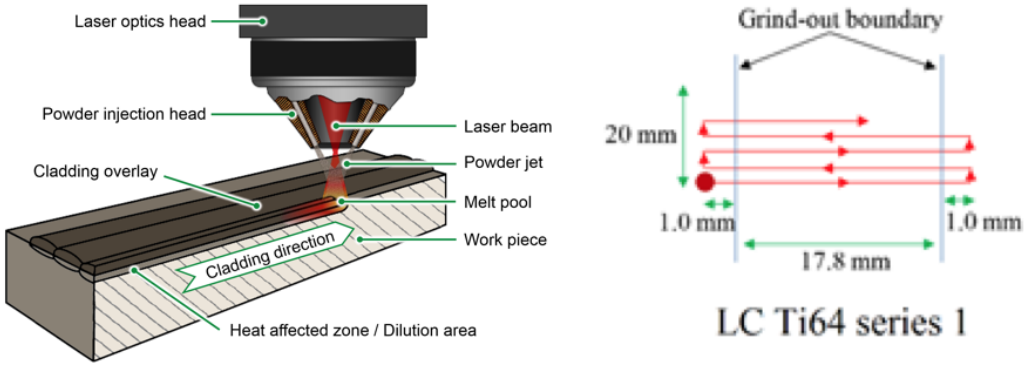


Fig. 3.4. Laser Cladding Pattern [49]

Once the cladding was complete, the excess height was machined in order to return the geometry to its original shape. There is a very small amount of gas porosities in the clad as can be seen in Figure 3.5, they are less than 50$\mu$m and sporatic throughout the clad.

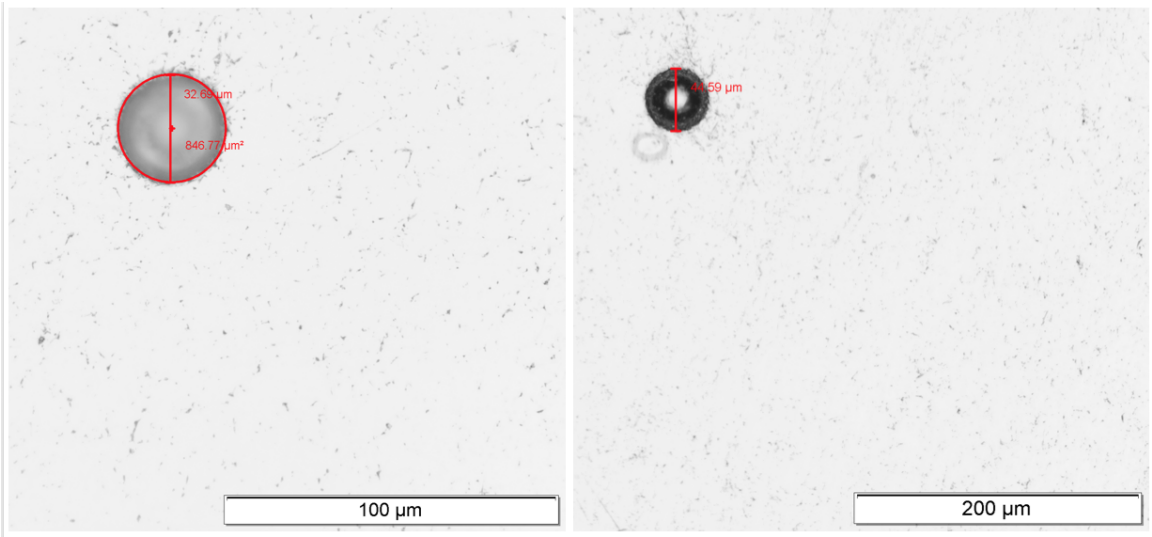


Fig. 3.5. Optical Image of clad surface - potential gas porosities

### 3.3 Laser Slot

Laser slotting was carried out at MINIFAB, a commercial micro manufacturing and prototyping facility located in Melbourne Australia. The laser used was a Coherent Industrial AVIA$^{TM}$ pulsed frequency tripled Nd-YAG laser operating at 355nm with a Q-Switched (QS) pulse duration of 2$\mu$-sec, QS period of 100 $\mu$sec and a repetition rate of 10 kHz or 1 kHz where required. This configuration produces a 10$\mu$m FWHM beam at a typical energy of 164 $\mu$J/pulse at the position of laser focus approximately 165 mm down stream of the objective lens.

The specimens were placed down stream of the objective lens with the material surface near the lens focus. To identify the optimum distance a thin foil of metal is first laser machined using a test pattern. This is repeated as a function of foil height relative to the objective lens. The optimum height for laser machining is obtained where the foil is machined through for the minimum number of passes of the laser beam. The height of the specimen to be machined is then adjusted so that the surface height of both the thin foil test piece and the specimen coincide which

results in a depth of roughly 25$\mu$m. The actual laser patterning of the specimens

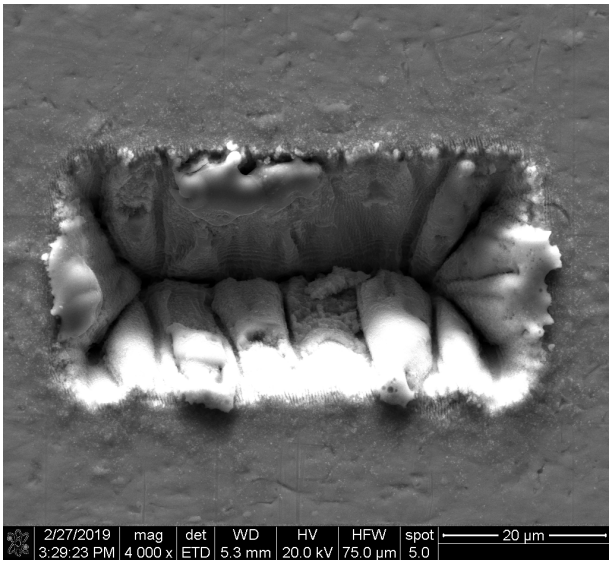


Fig. 3.6. SEM NOVA Image of Laser Notch

(ie. the pattern of slots) was facilitated by successive x-y scans of the laser beam in response to instructions given to 2 galvanometer (ScanPro Galvo-Scanner) actuated mirrors positioned up stream of the objective lens. The deep trenches were patterned on the specimen surface by successive passes of the laser beam in response to repeat galvanometer instructions. These instructions were created from the output of a CAD drawing and translated into the Hewlett-Packard$^{TM}$ graphics language (HPGL). The vector HPGL file is converted by a digital signal possessor in the laser control hardware with the addition of software correction to compensate for the non-ideal objective lens optics into a series of instructions for the motion of the galvo mirrors in unison with on/off instructions for the laser Q-switch. The resulting trench pattern is 50 by 30$\mu$m as can be seen in Figure 3.6.

### 3.4 Heat Treatment

A review of literature considering heat treatment of Ti-6Al-4V was conducted and it was determined that the majority of stress relief treatments for Ti-6Al-4V is 480°C

to 650°C for 1-4 hours [2]. There was a wide range of stress relief heat treatments for additive manufactured materials in the literature [4,5,31,50–52], from these it can be determined that Ti3Al nano-precipitates [53] start to form below 550°C [2], however approximately 4-8 hours of aging time is required to form the Ti3Al nano-precipitates and hence these are not expected to be an issue in the present study.

At 600°C, there is some slight widening of the alpha lathes observed in the micro-structure [4] and as stated in [51], 480°C for 2 hours is a common stress relief for titanium alloys with no micro-structure changes in Ti-6Al-4V occurring. To be consistent with cited references and to ensure consistent microstructure between samples, a stress relief of 480°C for 2 hours was chosen.

# 4. RESIDUAL STRESS ANALYSIS

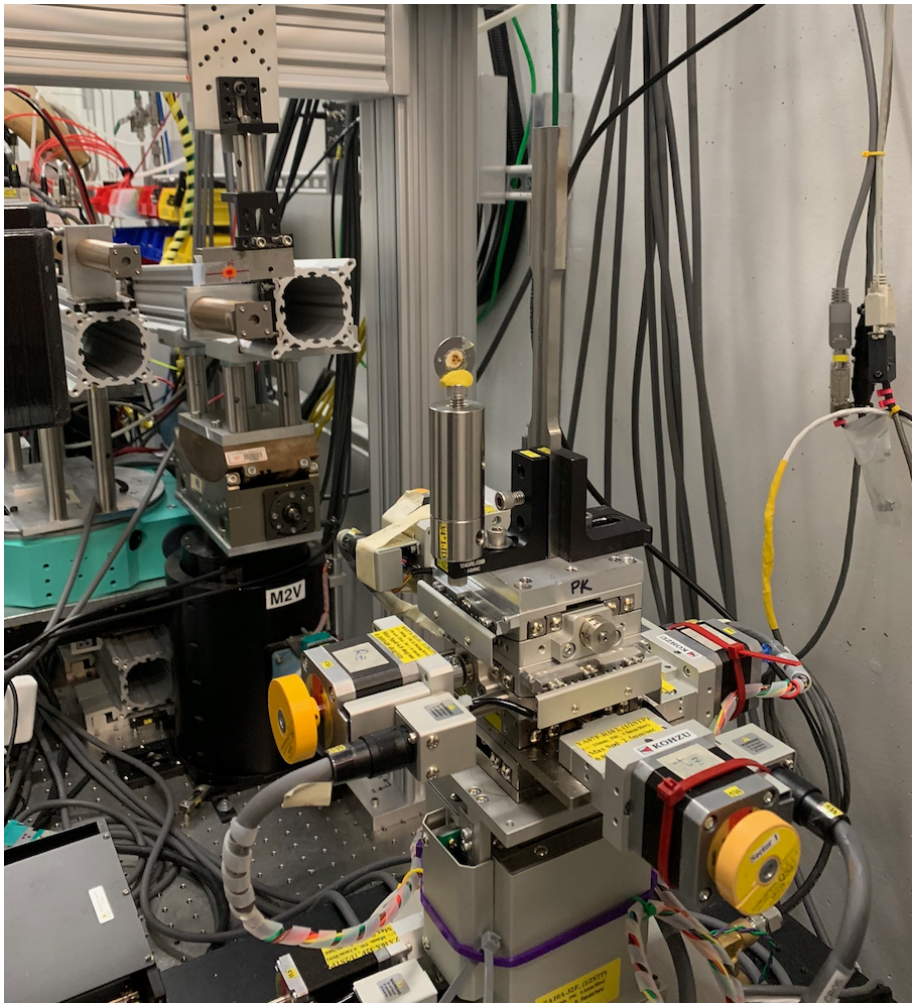


Fig. 4.1. Experiment Setup

X-ray Diffraction experimentation was undertaken at the 6-BM-A end-station of the Advanced Photon Source (APS), Argonne National Laboratory, Illinois. The sample was placed incident with the incoming polychromatic beam with germanium detectors placed downstream which are cooled by liquid nitrogen to prevent overheat-

ing from the incoming beam. The size of the beam itself was controlled by slits upon exiting the source to provide a final gauge volume of detection. The two germanium detectors placed downstream from the specimen were on the YZ plane and XZ plane respectively; the detector placed on the YZ plane is referred to as the vertical detector with $d_v$ the corresponding scattering vector associated with the strain measurement direction. The detector placed on the XZ plane is referred to as the horizontal detector with $d_h$ the corresponding scattering vector. The vertical and horizontal detectors and associated slits were positioned such that $2\Theta_v$ were 4.74° and 4.82° respectively based on crystalline structure and beam energy spectrum.

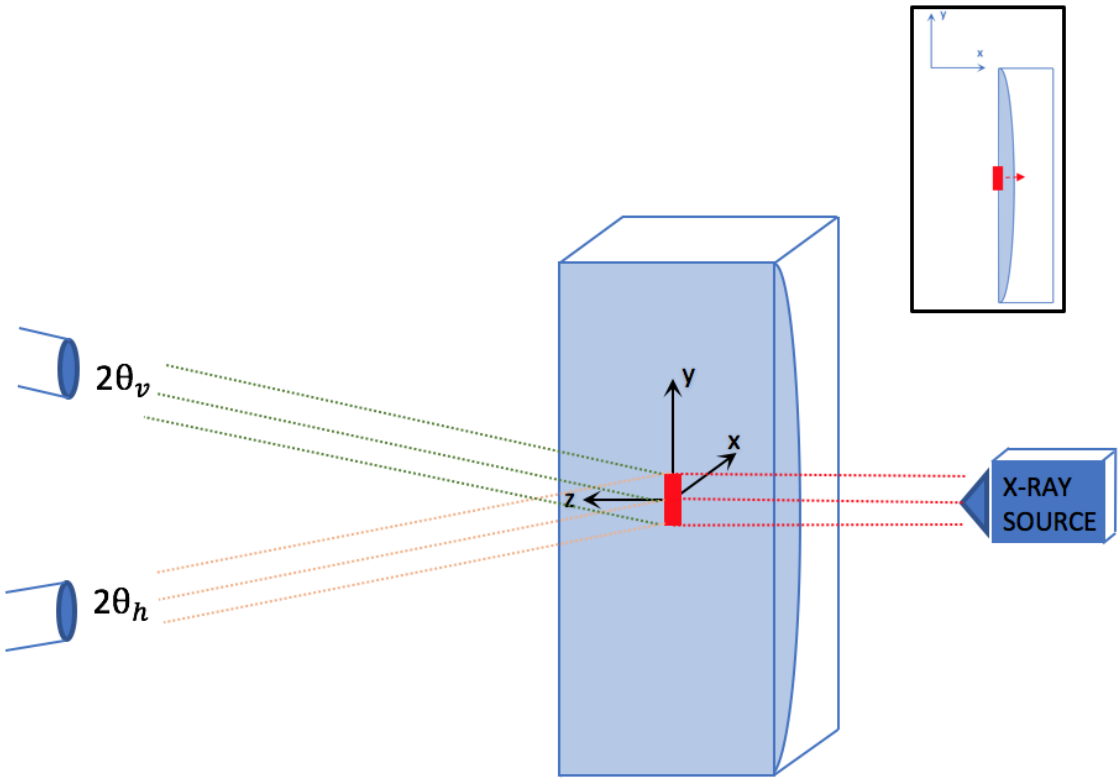


Fig. 4.2. EDD Path through gage section

The sample was positioned downstream from the beam on a translation and rotation table to ensure the gauge section was incident with the beam as per Fig-

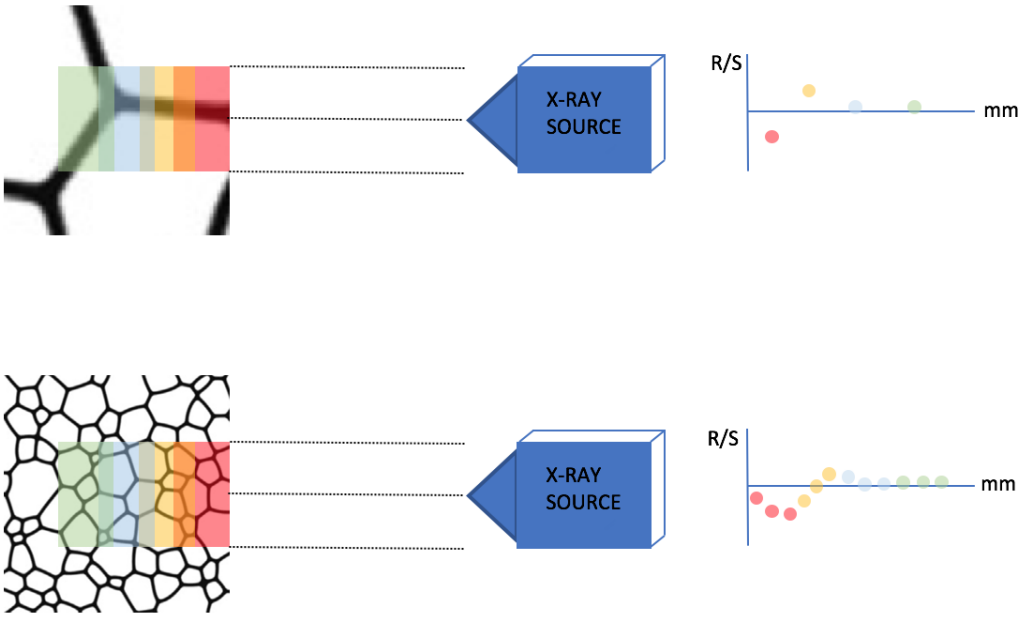


Fig. 4.3. Course vs Fine Residual Stress EDD Example

ure 4.2 and 4.1; the sample itself is aligned through pre-positioned lasers. In order to collect as many possible diffraction directions of the lattice, the specimen was rotated about it's y-axis from 0°, 15°, 30° and 45°. Rotations about the z-axis were also carried out at -8°, 0°, and 8°. These two sets of rotations were conducted individually at each position along the x-axis as the beam scanned through the specimen; the scanning along the x-axis proceeded from the free surface up to 2.5mm through the clad into the material substrate. Regarding the area scanned, in the initial setup the slits were adjusted to allow 200 x 50 $\mu$m box with a 50 $\mu$m step size and 6 lines per specimen; however, during this scan, there was a lack of resultant intensity and therefore ability for any significant diffraction peaks to be related to its family of lattice planes. This was assumed to be due to course grain structure, with grains potentially larger than the 200$\mu$m gauge box section being utilised, due to this the slits were adjusted to create a 500 x 50 $\mu$m box with a 50 $\mu$m step size and 3 lines per

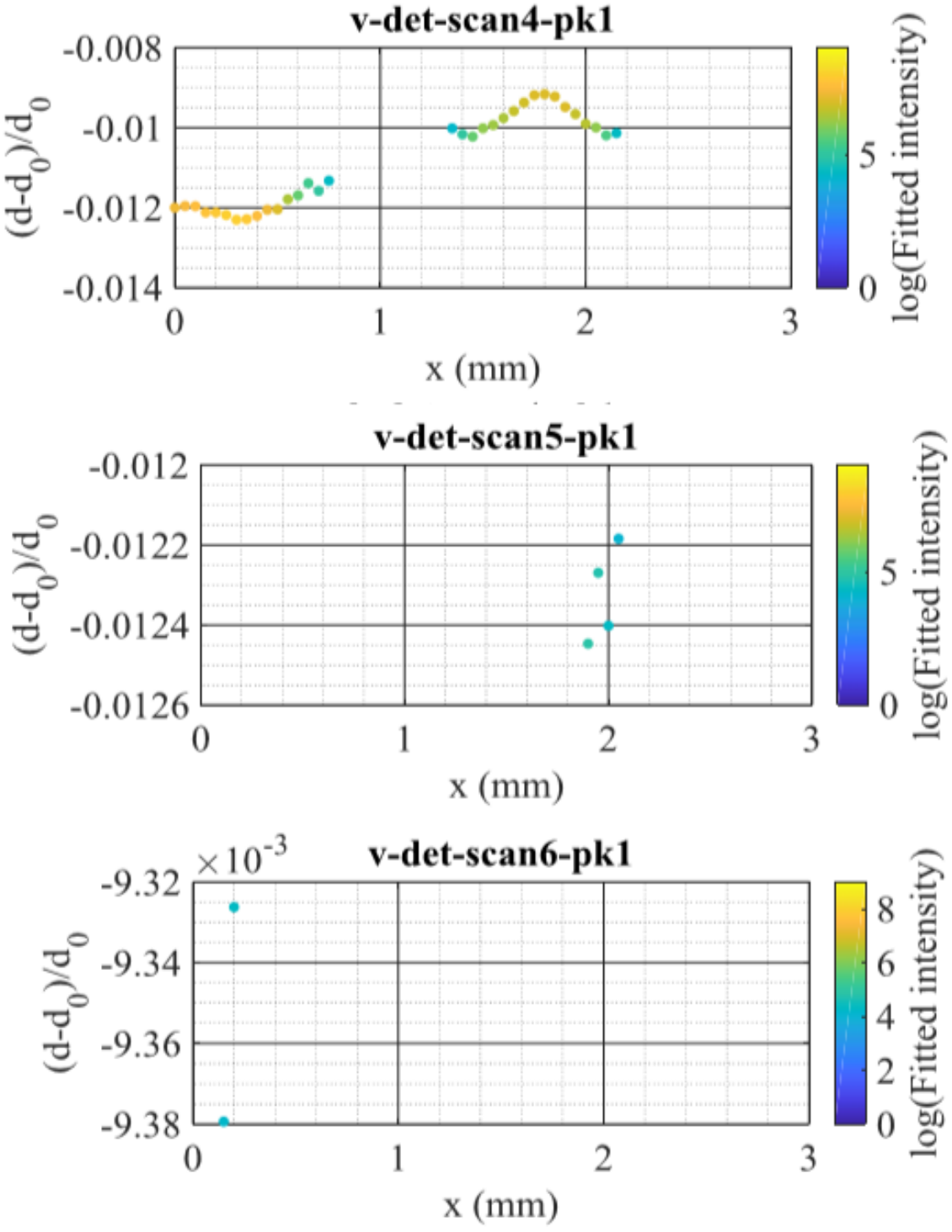


Fig. 4.4. Example of inconsistent lattice strains

specimen. Whilst outputted intensities did improve, and therefore peak intensities could be better evaluated, inconsistency amongst these peaks resulted in lack of any residual strain data.

In an ideal sample it is expected that the trend of any component of strain to be independent of the choice of the peak as the grains within the gauge volume, which are associated with a particular peak, are expected to be well-distributed within the entire gauge volume. In our case, this was not achievable, therefore it is more likely that the grain size is large enough to consume the majority of the gauge section and therefore provide a very poor average representation of lattice strains throughout the specimen microstructure; Figure 4.4 and 4.3 provides an example representation.

Further work in the future will look at alternate techniques to improve quality and usability of residual stress results.

# 5. MICRO-STRUCTURE ANALYSIS

The microstructure of Ti-6Al-4V consists of a low temperature hexagonal close-packed (HCP) $\alpha$-phase, which is stabilized by Aluminum, and a high temperature body-centered cubic (BCC) $\beta$-phase, which is stabilized by Vanadium. Depending on the thermal processing history of the alloy, the microstructure could be fully lamellar, fully equiaxed, or a combination of the two, denoted as bi-modal [2]. As-cast Ti-6Al-4V typically has a lamellar microstructure with fine colonies of alpha, and mill-annealed condition Ti-6Al-4V typically has an equiaxed microstructure with coarsened colonies of alpha [2].

## 5.1 Specimen Mounting and Polishing

Two specimens, one clad and one clad post heat treatment, were sectioned through the gauge section to ensure a cross-section of subtrate, HAZ and clad were view-able. The sectioned material was then mounted in Bakelite. Polishing was then conducted as follows:

- 400 grit (ANSI) polishing pad, 30 mins, semi-auto polish, 1 pound (4.45N) of polishing force selected, with 0.5 micron colloidal silica;
- 600 grit (ANSI) polishing pad, 30 mins, semi-auto polish, 1 pound (4.45N) of polishing force selected, with 0.5 micron colloidal silica;
- NAPPAD polishing pad, 30 mins, semi-auto polish, 1 pound (4.45N) of polishing force selected, with 0.5 micron colloidal silica;
- MICROPAD polishing pad, 8 hrs, vibration polisher with 2 weighted inserts, with 0.5 micron colloidal silica.

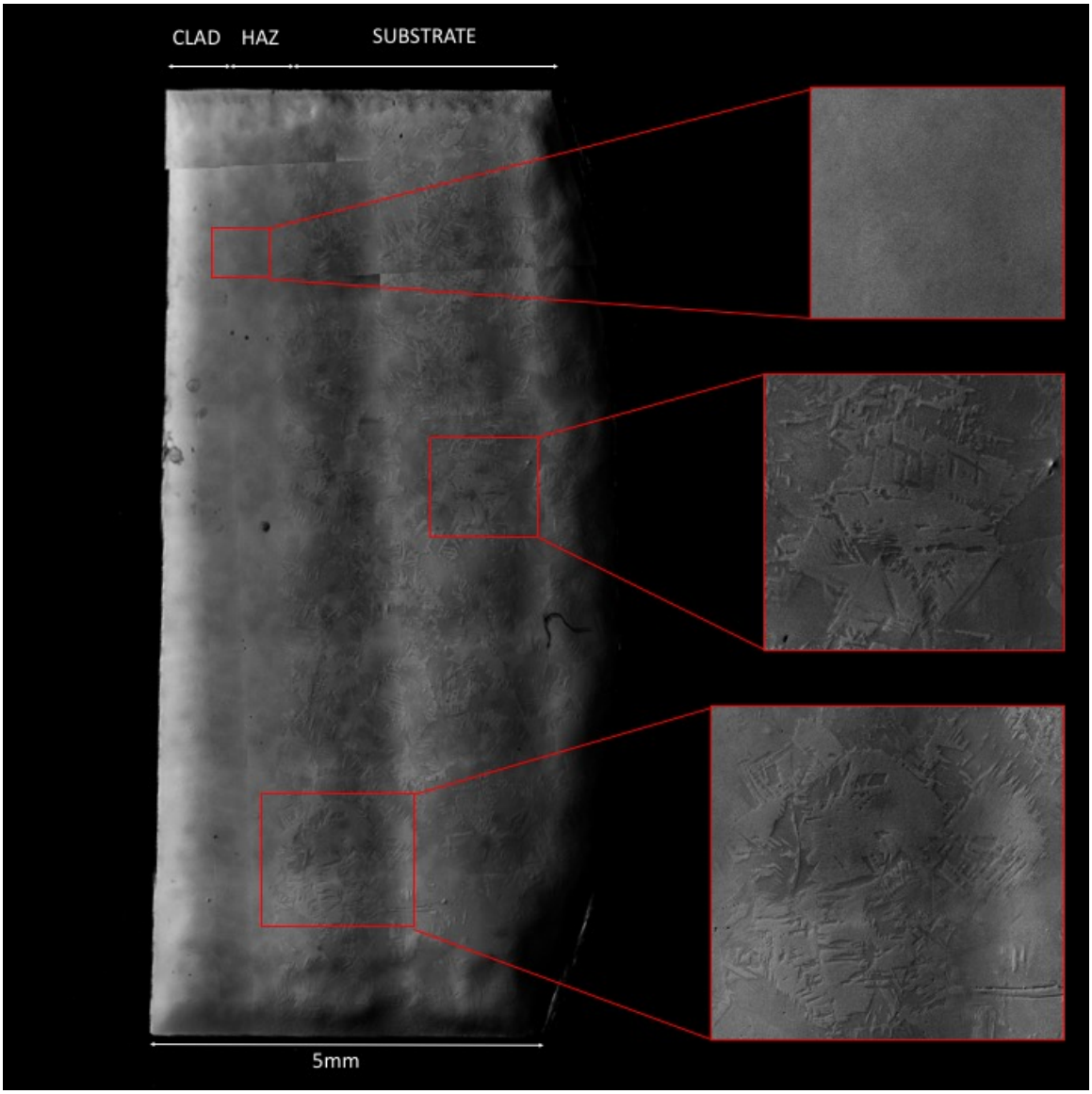


Fig. 5.1. 7A As Clad Polished Cross Section under optical microscope 5x - measurements and locations of Clad/HAZ/Substrate at this stage are for illustrative purposes only

This was conducted until a mirror polish was identified, then cleaned with sonic cleaner using distilled water, Isopropyl Alcohol, Acetone and Methanol in that order. The resulting polish can be seen in Figure 5.1, taken under an optical microscope with post image processing to reveal some of the visible microstructure.

## 5.2 BSE Imaging

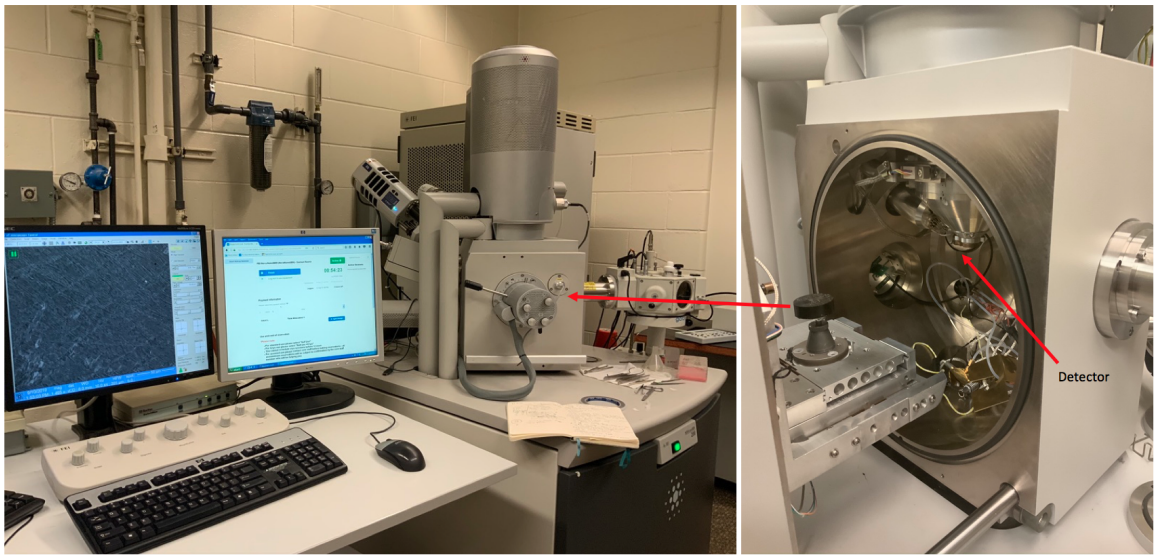


Fig. 5.2. FEI NOVA SEM Overview (left), internals (right)

Back Scatter Electron (BSE) imaging was conducted at Purdue Life Sciences using the FEI NOVA NanoSEM (Figure 5.2). BSE imaging is conducted by emitting high energy electrons at the surface of a material, the electron beam interacts with the materials atomic nuclei which scatters the emitted beams electrons. The amount of scattered electrons is directly related to the atomic number of the material, i.e. the heavier the element (atomic number), the brighter the contrast due to the increased amount of electrons scattered back to the materials surface and thus absorbed by the detector. The detector used in the FEI NOVA was a four-quadrant semiconductor placed above the sample (Figure 5.3). Settings for the images were as follows;

- Accelerating Voltage: 10.0 kV
- Spot Size: 5.0
- Working Distance: 5-12 mm

- Aperture: 100$\mu$m

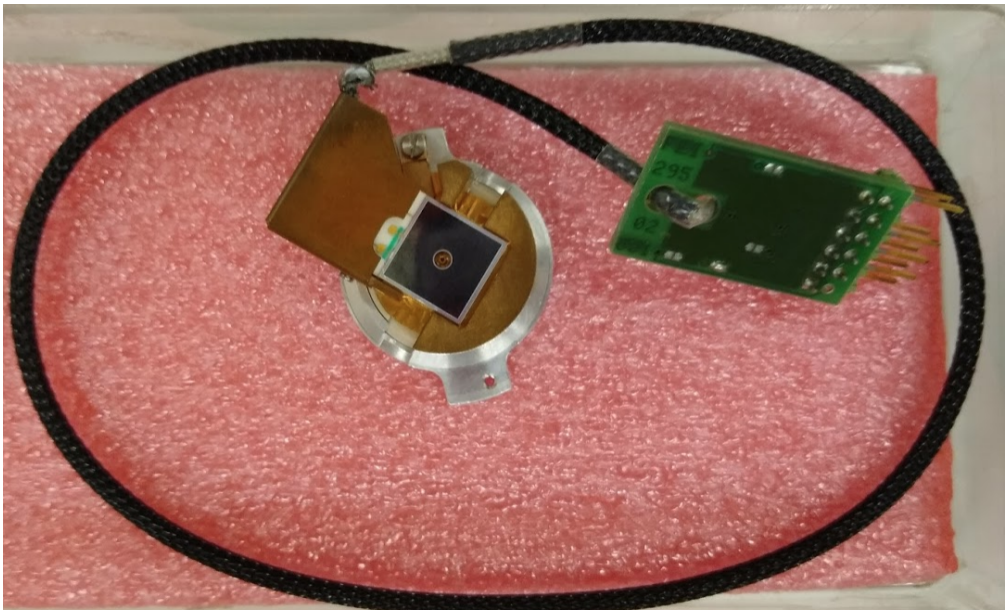

Fig. 5.3. BSE Detector

As can be seen from the substrate sections of each BSE image, there is a fine lamellae structure ($\alpha$ + $\beta$) forming on the prior $\beta$ grain boundaries and growing perpendicularly to the existing lamellae structures within the grain (Figure 5.4 (d)). This is considered a result of low to moderate cooling rates which lead to creation of a lamellar microstructure consisting of $\alpha$ + $\beta$-phase lamellae within large $\beta$-phase grains [54], as can be seen consistently in the substrate. There is also the appearance of potential Widmanstatten structure with basketweave morphology evident in Figure 5.4 (b); Widmanstatten is a common micro-structure in slow cooling rate mil-annealed Ti-6Al-4V alloys [55].

The clad itself appears as a very consistent $\alpha$' martensite needle like structure (Figure 5.4 (e)), this is likely due to the fast cooling rate of laser cladding [20]; the cooling rate is driven by the clad being applied to the cool metallic substrate with each pass being allowed to cool back down to room temperature before a new layer of clad is applied. This microstructure continues throughout, up until transition into the

substrate; appearance of grain boundaries throughout the clad gives the impression of long $\beta$ wavy grains common in Nd:YAG deposits, with the heat flow direction affected by the laser movement [25].

The martensitic microstructure formed after rapid cooling leads to a greater likelihood of higher hardness values then that of the lamellae/Widmanstatten substrate; this is seen during hardness testing of the sample which is covered later. Research regarding the microstructures of selective laser melted (SLM) Ti-6Al-4V was dominated by a typical hierarchical martensite structure with a high density of dislocations and twins, including primary, secondary, tertiary and quartic martensites within columnar prior $\beta$ grains [56]. Experimentation with Ti-6Al-4V martensitic microstructure displayed good strength properties but reduced tensile elongation stiffness; this can be altered with the use of heat treatment to relax dislocations [57]. The heat treatment conducted on the specimens in this thesis was for 2hrs at 480°C. This temperature was chosen (as discussed earlier) to promote relaxation of any tensile residual stresses produced from the cladding process whilst ensuring no significant microstructure changes are present. Research has shown that certain heat treatment of additive laser manufactured components has the potential effect of decomposing the martinsitic microstructure into fine lamellae, which has the effect of creating a more ductile response whilst maintaining high yield strength in fatigue [57]; however martensitic structure appears to have remained throughout all clad regions in both the pre and post heat treated specimens as originally intended. Whilst the harder, less tough clad may not provide the optimum fatigue response, it should allow a greater comparison of residual stress effects without concern for microstructure variability. There appears no obvious transition from clad to HAZ (clad depth expected at around 0.7mm), however clear and consistent transition to the substrate is apparent at 1.5mm (Figure 5.4 (b)), this can been seen with a change from a fine martensitic microstrucutre to that of a lammellae structure. There is also the appearance of a subtle basket-weave in this region which is supported in literature as evidence of HAZ where the temperature in the HAZ exceeds the $\beta$ transus temperature of 994°C and cools rapidly [19]. Cladding

of the specimens in this thesis was expected to have exceeded this temperature based on other research conducted by DST Group and RMIT [49]; the technique used is directly comparable to that conducted in RMIT research, during their research thermal camera images were taken which identified a peak temperature of 1100°C. There is a strong level of confidence regarding the depth of the clad, as only 0.7mm of material was removed from the substrate during machining (Figure 5.6) in order to apply the laser clad repair, it is therefore considered the HAZ is a similar depth of at least 0.7mm.

## 5.3 Hardness Testing

The mounted samples were tested in a Leco LM Series Microindentation Hardness Tester using a Vickers turret with a 25 gram weighted force and a dwell time of 13 seconds. The Vickers Hardness testing followed ASTM E384-17, with the use of a line of ten indentations at 30$\mu$m apart [58]. The indents were taken between 60-140 $\mu$m from the free surface. Regions chosen were clad, substrate, clad heat treated and substrate heat treated, with the results as per Figure 5.7. The clad region is notably harder then the substrate, this is likely caused by the much courser grain structure in the substrate material and supports the previous chapters analysis of the harder martensitic clad region.

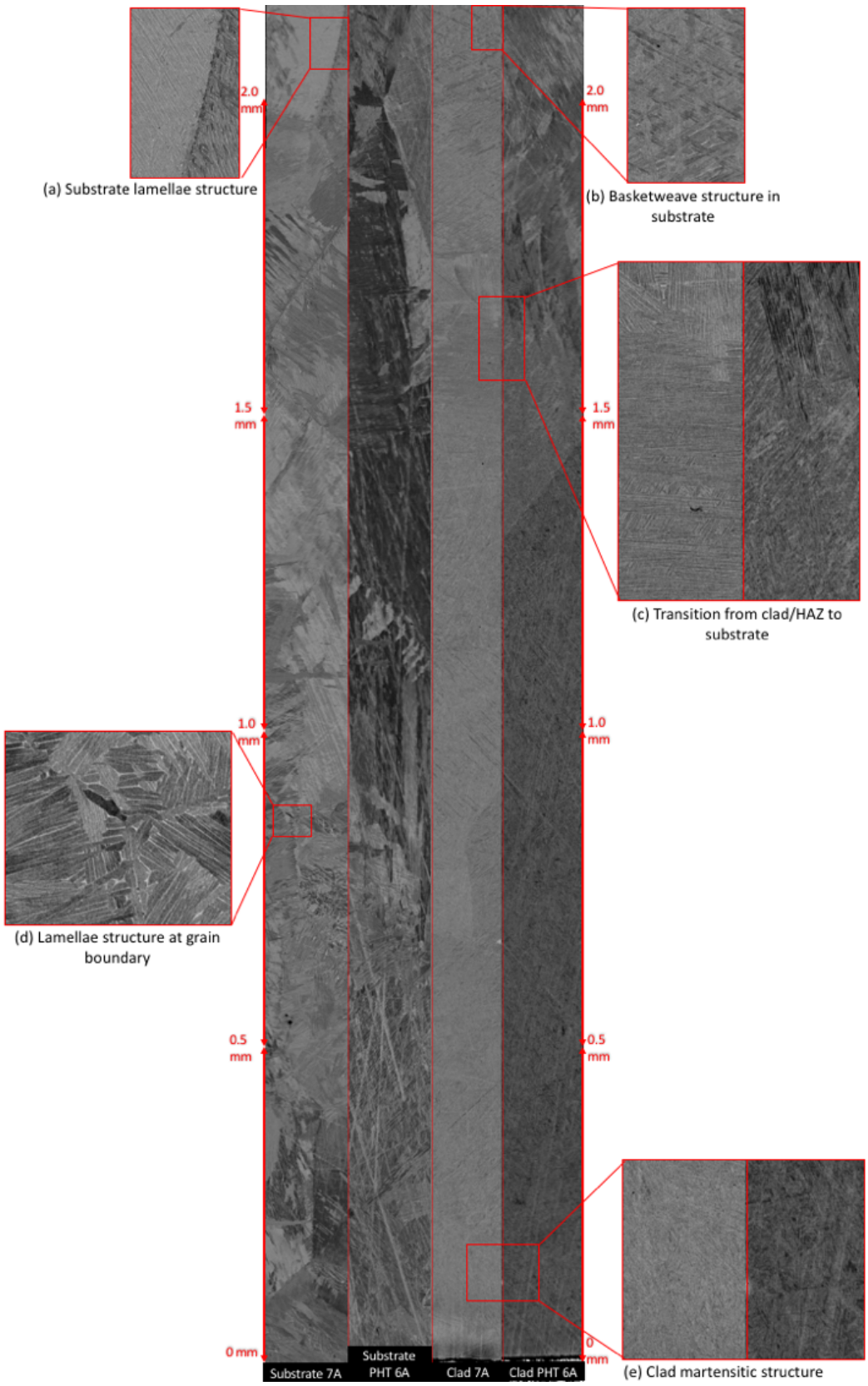


Fig. 5.4. Baseline vs Clad vs PHT 50micron

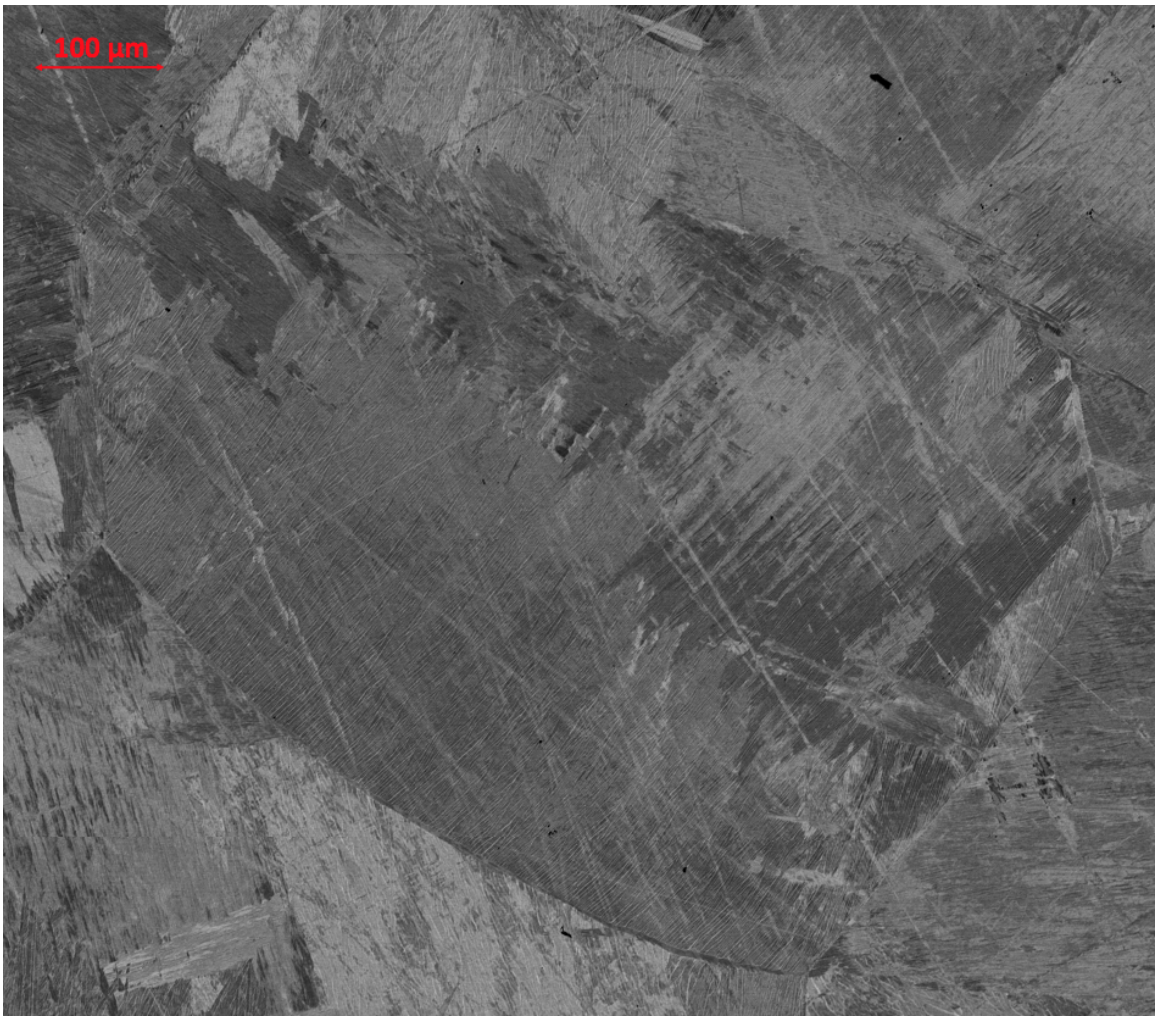


Fig. 5.5. 6A PHT Grain Baseline

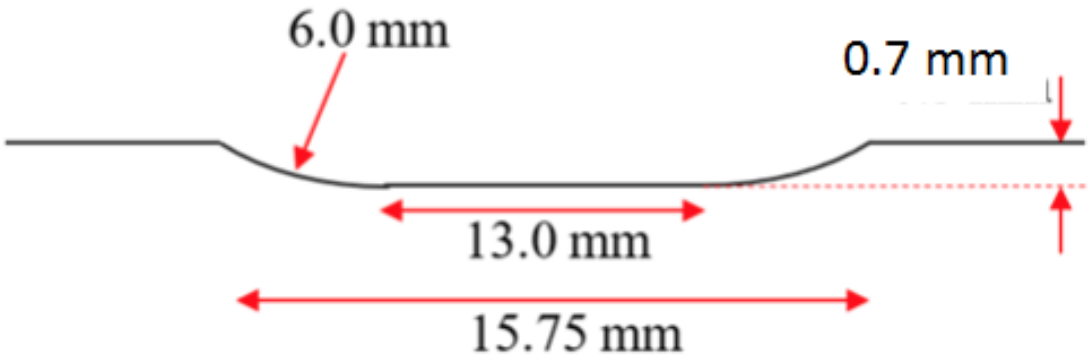


Fig. 5.6. Clad Depth

| Specimen | 7A CLAD | 6A CLAD PHT | 7A SUBSTRATE | 6A SUBSTRATE PHT |
|---|---|---|---|---|
| Mean HV | 320.2 | 337.4 | 285.3 | 281.4 |
| Median HV | 319.5 | 336.5 | 292.0 | 277.0 |
| SD | 0.3 | 10.9 | 5.1 | 11.1 |

Fig. 5.7. Hardness Test

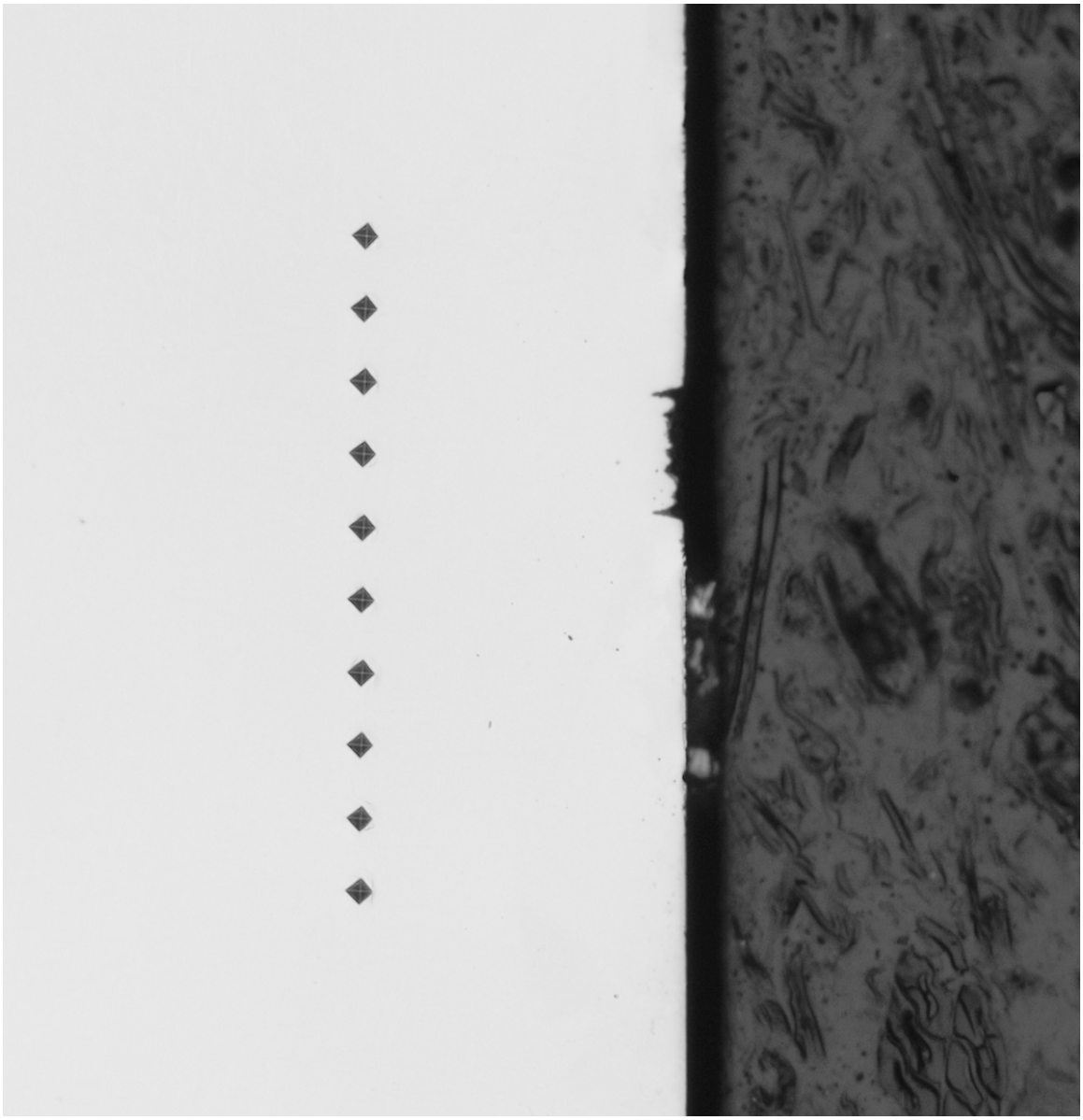

Fig. 5.8. Hardness Test Example

# 6. FATIGUE TESTING

## 6.1 Tensile Test Machine Setup

An MTS Tensile Load Frame was utilized for this experiment, consisting of;

- MTS model 632.41B-01 Load Frame rated to 50kN
- MTS model 661.20E-03 Force Transducer with 100kN capacity
- MTS model 647.10 Hydraulic Grips with serrated wedge inserts rated to 100kN
- MTS model 609.10 Force Alignment cell rated to 100kN

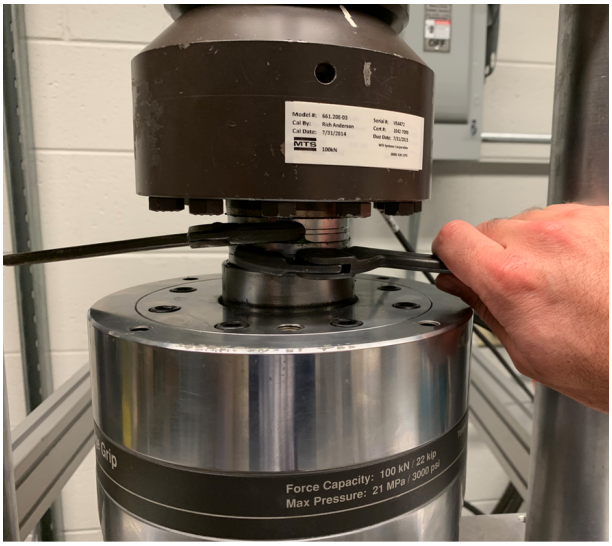


Fig. 6.1. Locking Collars

In order to assemble this load frame the previous load cell and associated grips were removed. This was conducted by applying a load in tension to a dummy specimen under displacement control to assist with reducing locking compression on the collars

(Figure 6.1); load was slowly increased until force was raised high enough for the collars to be loosened. After this, the load may be reduced to zero, and each component (grips, force transducer, alignment cell and associated adapters) can be unwound, removed, and new components reassembled in reverse order.

Due to the MTS test frame's load chain being re-built, a re-calibration was required in order to assess the amount of bending exerted upon application of tensile load. This utilized a Strain Gauge Alignment Transducer (which needed to be designed and manufactured), Switch and Balance Unit and Wide Range Strain Indicator.

Alignment guidance was provided by ASTM E1012 [59] for alignment of tensile and fatigue tests. The Alignment Transducer is effectively a test specimen that can be monitored under load with the use of strain gauges, this required selection of a specimen with similar mechanical properties to that of the experimental specimens (Ti-6Al-4V). In accordance with ASTM, it is common to select a generic material to be used across varying experiments and calibrations, due to this Steel 1045 was selected as it covered the range of tensile loads that would be applied to Ti-6AL-4V, has high stiffness and would be applicable to other high strength materials in future tests.

Once the specimen was identified strain gauges as small as practical were selected to avoid any strain averaging effects with adjacent gauges. A standard two-by-four gauge setup was chosen (Figure 6.3) to enable accurate assessment of bending moments when using a thin rectangular specimen [59]. Gauges, preparation tools, and adhesives were supplied by Micro-Measurements$^{TM}$ and applied to the specimen in accordance with supplied Micro-Measurements$^{TM}$ procedures.

This involved surface preparation of the steel specimen in order to develop a clean surface with appropriate roughness and correct pH for strain gauge bonding. This was completed by first degreasing the surface with isopropyl alcohol, then the surface was abraded with 400 grit silicon-carbide paper. Once complete the surface was indicated with the location and the dimensions of chosen gauges. The surface

is then conditioned with a diluted solution of phosphoric acid until no debris or discolouration is noted on the cotton tipped applicator. In order to maintain the correct pH for bonding the surface is neutralised with ammonia water with single use cotton applicators. Strain gauges were then applied, first by aligning using

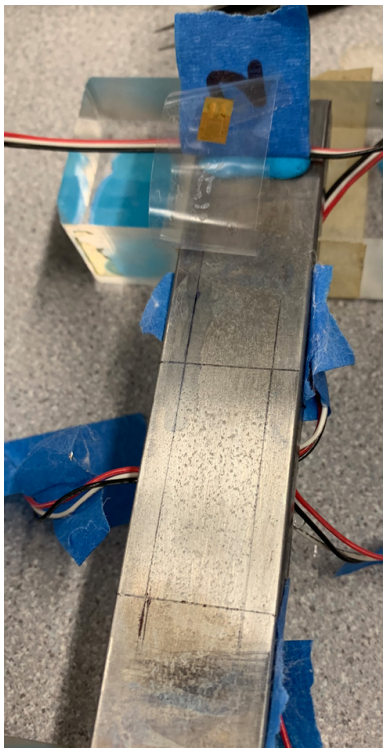

Fig. 6.2. Alignment of Strain Gage

cellophane tape as per Figure 6.2, once satisfactory alignment is achieved, the gauge and surfaces are coated with a bonding catalyst which is allowed to dry before a drop of adhesive is applied. The gauge is then wiped onto the surface using the cellophane tape under tension and the tape is then removed after one minute of pressure has been applied to the adhered gauge. Once all strain gauges were applied, lead wires were then attached to the positive and negative terminals of each strain gauge using careful soldering techniques. The strain gauge alignment transducer was then connected via lead wires to a switch and balance unit with wiring completed in order to produce a quarter-wheatstone bridge (Figure 6.4). The wheatstone bridge is able to identify

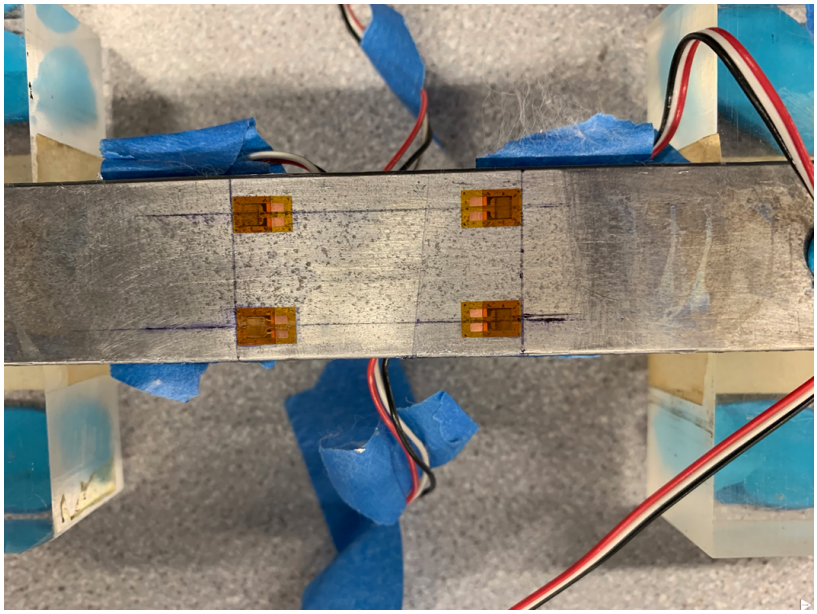

Fig. 6.3. Stain Gauge Orientation

change in resistance through the deformation of the strain gauge foils on the specimen, this deformation creating a resistance $R_x$. Identifying a value for $R_x$ (i.e. strain) is achieved by first adjusting variable resistor $R_2$ until the potential between D and B is zero. Since resistors $R_1$ and $R_3$ are known (they are attached to the rear of the Switch and Balance unit) and the potential between D and B is zero, therefore the ratio of the resistors $R_2$ and $R_1$ are equal to $R_x$ and $R_3$; we can then calculate for the only unknown $R_x$ ($R_x/R_3 = R_2/R_1$). Each resistance/strain for each individual strain gauge can then be displayed on the wide range strain indicator.

ASTM guidelines [59] provides procedures to calculate the pure bending moment (PB) based on strain in each of the four strain gauges on each face ($e_{1-4}$) along

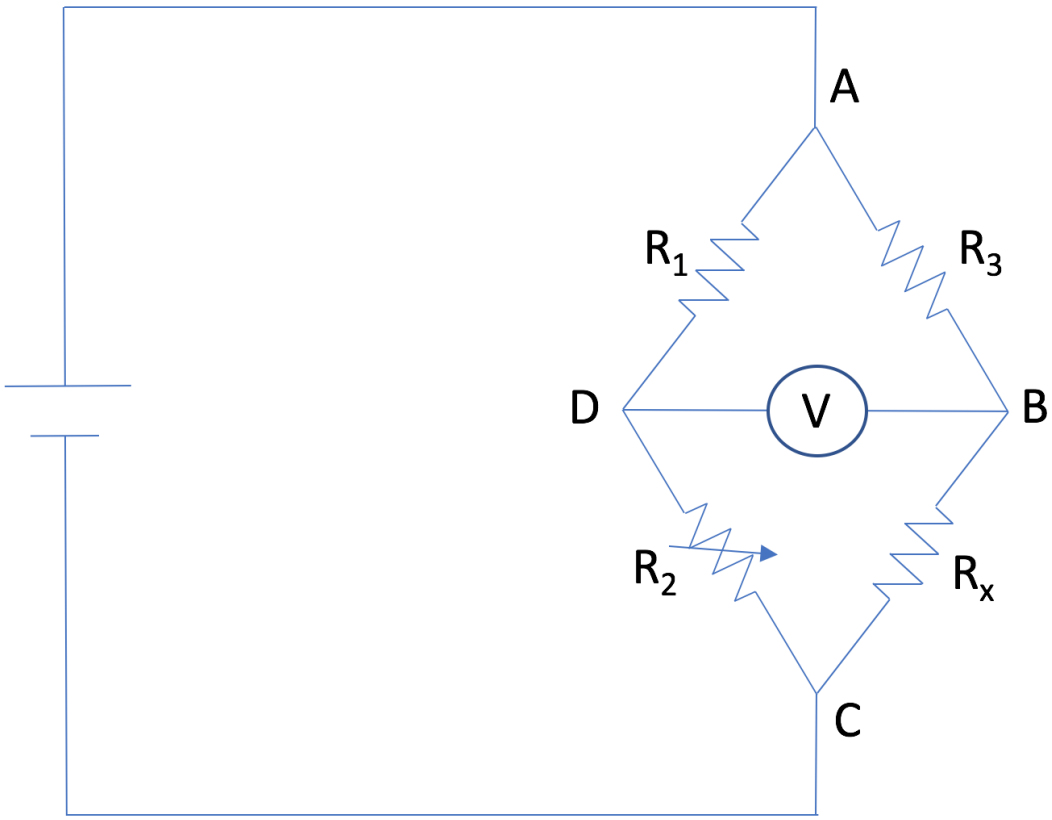


Fig. 6.4. Wheatstone Bridge Setup

with local bending strain (b) and maximum bending strain (B). These values are determined by the following set of equations:

$$a = \frac{(e_1 + e_2 + e_3 + e_4)}{4}$$

$$b_1 = e_1 - a$$

$$b_2 = e_2 - a$$

$$b_3 = e_3 - a$$

$$b_4 = e_4 - a$$

$$B = \frac{1}{2}\sqrt{(b_1 - b_3)^2 + (b_2 - b_4)^2}$$

$$PB = (\frac{B}{a}) * 100$$

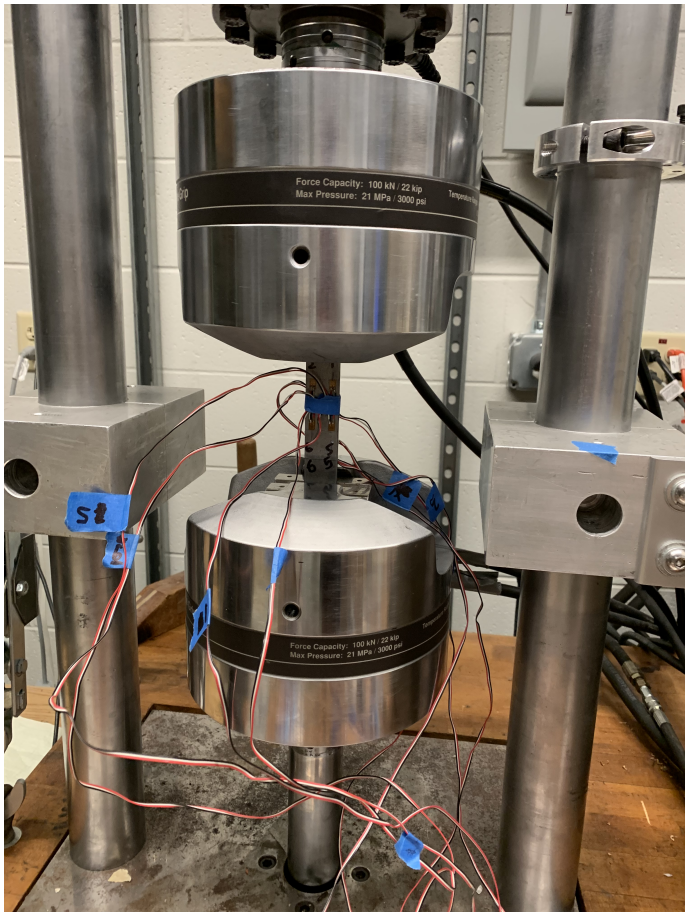


Fig. 6.5. An image of calibration setup

Once the bending moment is understood, the readings can then be compared to a chart (Figure 6.6) regarding the required concentric and axial adjustment dependent on the location of compressive and tensile strains, in order to reduce the relevant bending moment. Then the entire process is repeated until consistent results at various loads is achieved.

During calibration consistent results of less than 2.5% bending moment in initial configuration was achieved; however it was identified that the specimen itself had a slight bend that revealed itself when conducting verification with the specimen rotated 180° from its initial configuration. Upon consulting MTS technicians this is not uncommon and can be accounted for with further calibration through averaging out the initial strain with zero load on the specimen in both the initial configura-

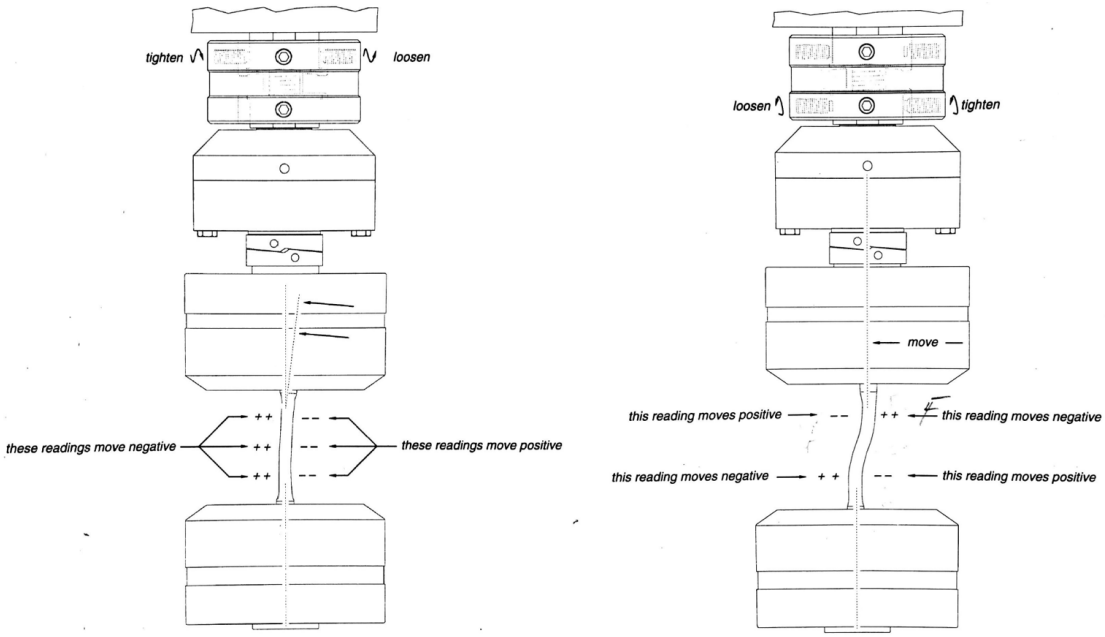


Fig. 6.6. Concentric and Axial Adjustment [60]

tion and when rotated 180°. Once this was conducted consistent results were again achieved with a slight increase; all bending moments were below 3.85% throughout the tested load range and in all orientations. The calibration was later confirmed by MTS who provided a free demonstration of their modern, semi-automated calibration service, using a Model 609 Alignment Figure (cylindrical strain gauge) and Model 609 Alignment Software (Figure 6.7); MTS considered the calibration of good quality considering the scale of equipment and setup being used.

## 6.2 Sensitivity/Frequency Analysis

Sensitivity analysis was conducted next in order to ensure an accurate force was generated throughout the fatigue test when compared to that commanded by the system. The first step was to ensure the MTS Load Chain was tuned to produce an ideal output post re-build and calibration of the system. In order to do this the

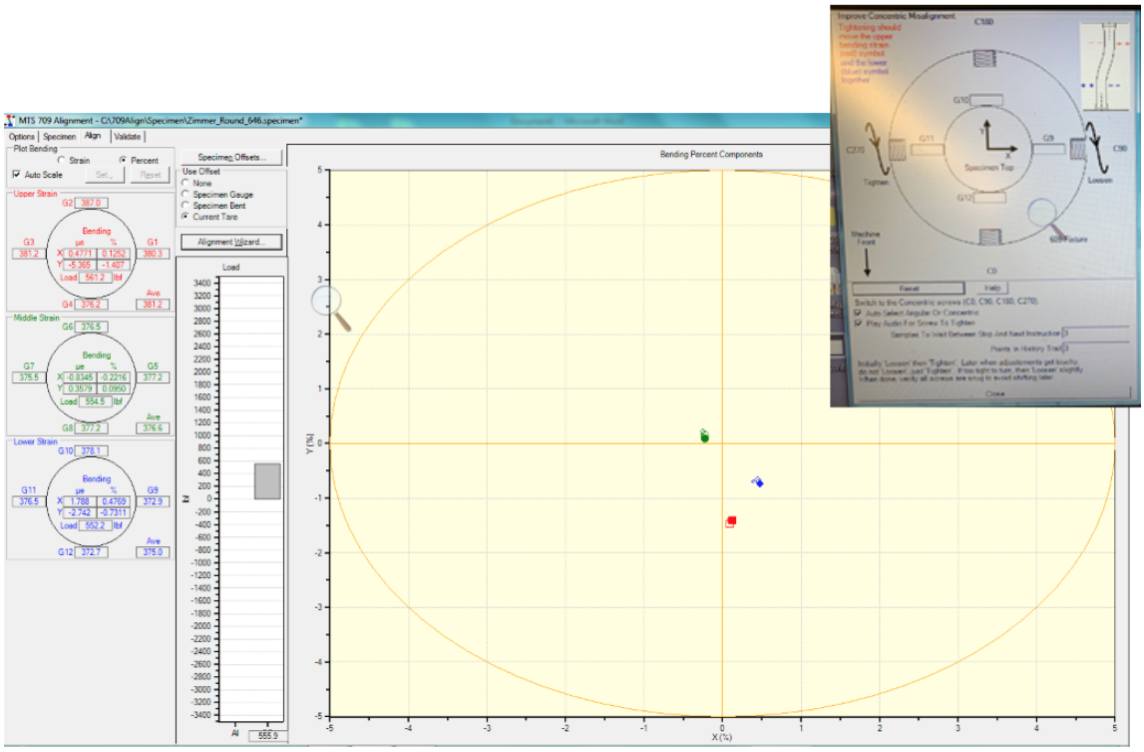

Fig. 6.7. 609 Alignment Software

MTS Controller software must be transitioned to CONFIGURATION MODE and the procedure in "MTS Series 793 Tuning and Calibration" carried out. This requires adjustment of Proportional (P) Gain, Integral (I) Gain and Derivative (D) Gain;

- P-Gain amplifies the systems error signal in order to control the system, i.e. the change in power is proportional to the error;
- I-Gain is the integral of the error signal i.e. error signal multiplied by time, increasing system response during static or low-frequency operation;
- D-Gain indicates the change in acceleration in the error signal and can anticipate the rate of change of the feedback and slows the system response at higher rates of change.

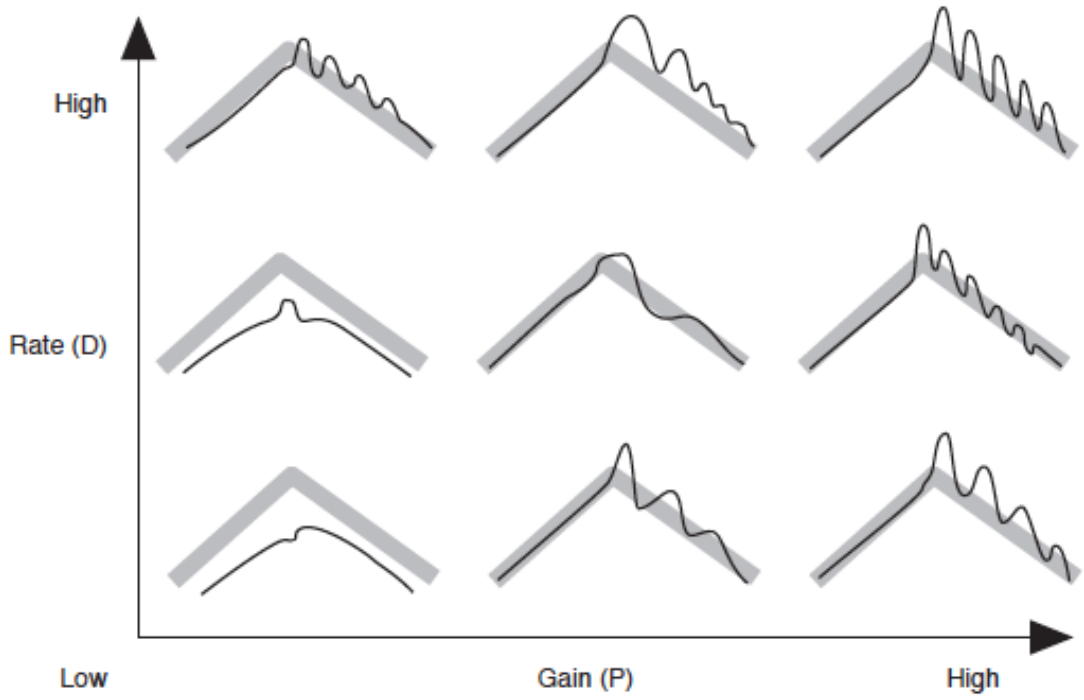


Fig. 6.8. P- and D- Gain Tuning Profiles [60]

The system was tuned and adjusted using a dummy sample of Ti-6Al-4V; an actual test specimen is not recommended to be used as extremely high frequency and uncontrollable loads are likely to and did occur during MTS tuning, which could damage or alter the test specimen.

Tuning was completed by starting with zero PID gain; each PID value was then slowly increased in a specific order to achieve a highly responsive cyclic signal with as little noise as possible, whilst also keeping the system from going unstable. During this process the absolute error was reduced by over 100% when compared to baseline sensitivity tests conducted before tuning.

Once tuning was complete, a test specimen was inserted into the load frame and tested over a sample fatigue range of varying CA in order to mimic the fatigue experiment.

The test frequency was then determined after evaluating a range of frequencies using the Mean Square Error percentage (Equation 6.2) between the command load and the measured load to quantify how accurately the MTS could fatigue the specimen at a given frequency. Based on Figure 6.9, 3.0Hz was considered a good balance between error and test length. This was determined based on majority of error being related to lag of cycle in the transverse direction (time) and not due to max/min values which were consistently met and the primary consideration during fatigue experimentation.

$$MSE = \frac{1}{N}\Sigma(F_{actual} - F_{commanded})^2 \tag{6.1}$$

$$MSE\% = \frac{MSE}{F_{commanded}} \tag{6.2}$$

## 6.3 Experimental Setup

To conduct the experiment in a semi-automated fashion, MTS test software Multi-Purpose Elite was utilized; this allowed a simple coded program to manage the experiment and the variations in amplitude required throughout, as can be seen in Figure 6.10 (an extract from an actual test). In the main section is the flow chart where individual programs can be applied which control the frequency, load magnitude and cycles required at each stage of the experiment. Running concurrently to these programs is a parallel path with a program setup for data acquisition. The data recorded in this experiment was force, displacement and number of cycles.

In order to capture any crack initiation at the notches, a camera with a Mitutoyo 10x optical micro lens was setup focused on an individual notch (Figure 6.11). At certain intervals, dependent on the test being run, the experiment was paused, max load was applied, and an image of each notch recorded. Live recording was not possible due to the movement of the specimen during fatigue creating unusable images.

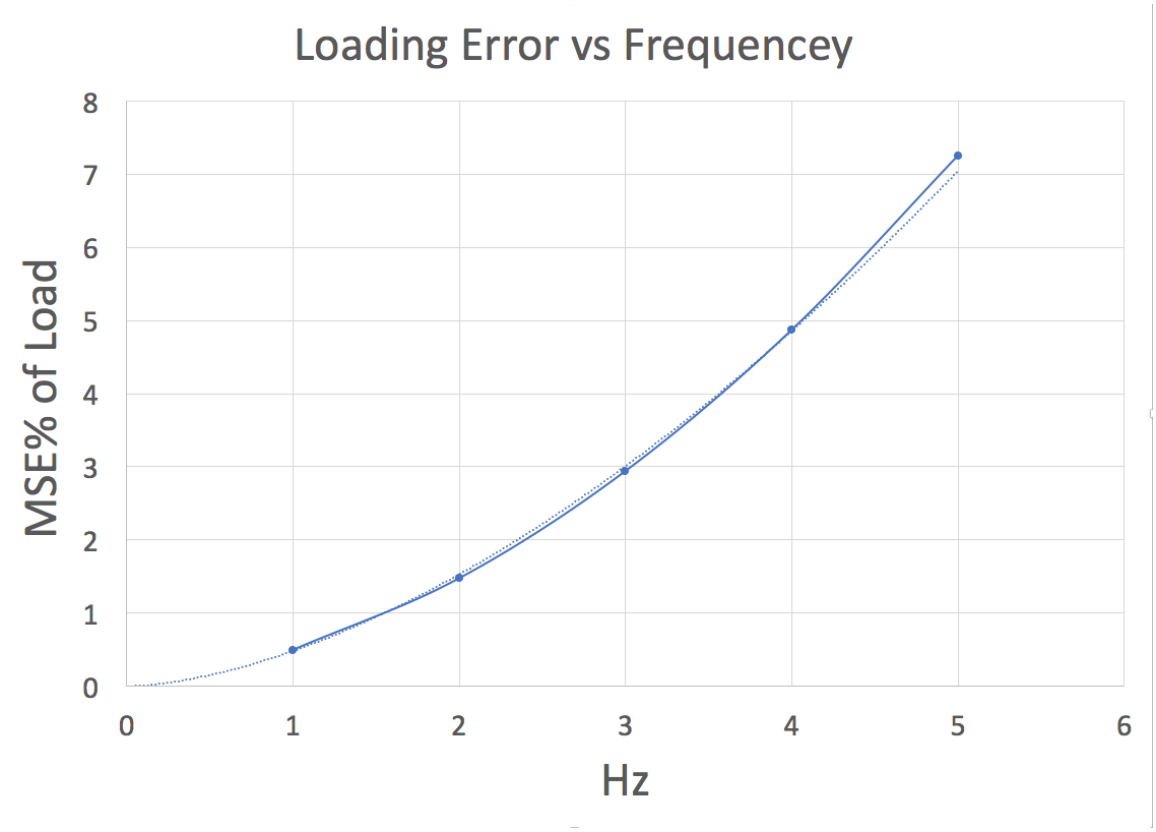


Fig. 6.9. MSE vs Frequency

## 6.4 Fatigue Experiment

The marker-band technique chosen is based on previous research conducted by Defence Science and Technology Group (DST Group) Australia [13, 17, 39]. Initially a maximum load of 42KN was selected based on a stress of 500 MPa (R=1.0), with a minimum load at 4.2KN and 50 MPa (R=0.1). This load is based off DST Group modeling the crack as a semi-circular surface flaw at the centre of the specimen, initial depth is 25$\mu$m and tip-to-tip surface length (2c) is 50$\mu$m. Loading was constant amplitude with max stress of 500 MPa, with simulated failure occurring at 99,663 cycles.

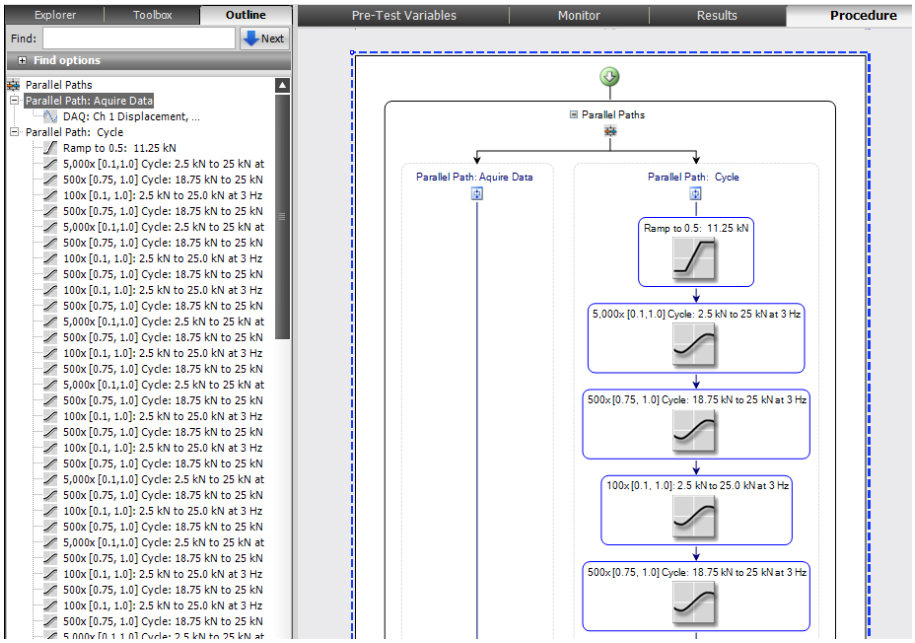


Fig. 6.10. Example of MTS Multipurpose Elite test program

Fig. 6.11. Camera Setup

Unfortunately during pre-test calibration it was discovered that even though the load cell and load frame were rated to 100kN the hydraulic actuator could not produce

Fig. 6.12. EDM Specimen - Design 1 (bottom) and 2 (middle and top)

greater than 25kN of force. Due to this, re-machining of the specimens was required. This was conducted at Purdue Kepner Labs on the Electronic Discharge Cutting (EDM) machine. The cross-section was reduced by roughly 50% as per Figure 6.12. The final cross-section of design 2 (D2) gauge section was 5.70x6.35mm. This reduced the required max load to 18kN (R=0.1) in order to exert 500MPa stress through the gauge section.

Regarding the marker bands themselves an M1 / M2 sequence was utilized based on previous research and experimentation [13, 39], these are as follows;

- (M1) 10000 cycles at 50 MPa to 500 MPa (R=0.1),
- (M1) 500 cycles at 375 to 500 MPa (R=0.75),
- (M1) 100 cycles at 50 MPa to 500 MPa (R=0.1),
- (M1) 500 cycles at 375 to 500 MPa (R=0.75).
- (M2) 10000 cycles at 50 MPa to 500 MPa (R=0.1),

- (M2) 500 cycles at 375 to 500 MPa (R=0.75),
- (M2) 100 cycles at 50 MPa to 500 MPa (R=0.1),
- (M2) 500 cycles at 375 to 500 MPa (R=0.75),
- (M2) 100 cycles at 50 MPa to 500 MPa (R=0.1),
- (M2) 500 cycles at 375 to 500 MPa (R=0.75).

Note: the above M1 and M2 are for baseline samples, clad samples will have a reduction in primary R=0.1 cycles by half.

An example of a set of marker bands is shown in Figure 6.13. The first test of a Design 2 (D2) baseline (6B) specimen resulted in failure towards the neck/gauge transition (Figure 6.14) at 51,587 cycles, less than initially anticipated by simulation data. This was attributed to extremely sharp edges along the sample post EDM machining; therefore another test was conducted, however this time the specimen (baseline 3A) was sanded and polished in order to round the edges and reduce stress risers along the specimens length. Improvement was achieved, with failure of the specimen occurring in the gauge section, and an increased life of 66,329 cycles; however the ideal failure condition, initiation at the notches, was not achieved.

In order to ensure the best possible probability of failure in gauge section further refinement of the design was undertaken. It was considered that reducing the severity of the transition from grip section, to gauge section be the priority. Therefore a specification was drawn up to ensure a constant radius be produced from the grip up until the clad/repair region, maximising the failure in the notches/clad for future testing. Lafayette Tool and Die were commissioned to complete EDM work to ensure consistency and efficiency with the final design seen at Figure 6.14 and Figure 6.15; each sample was smoothed by hand to reduce any likelihood of stress risers.

Due to the adjusted cross-section of the Design 3 (D3) specimens now at 8.5x6.35mm, the load regime was again adjusted. Due to the shorter life than anticipated in previ-

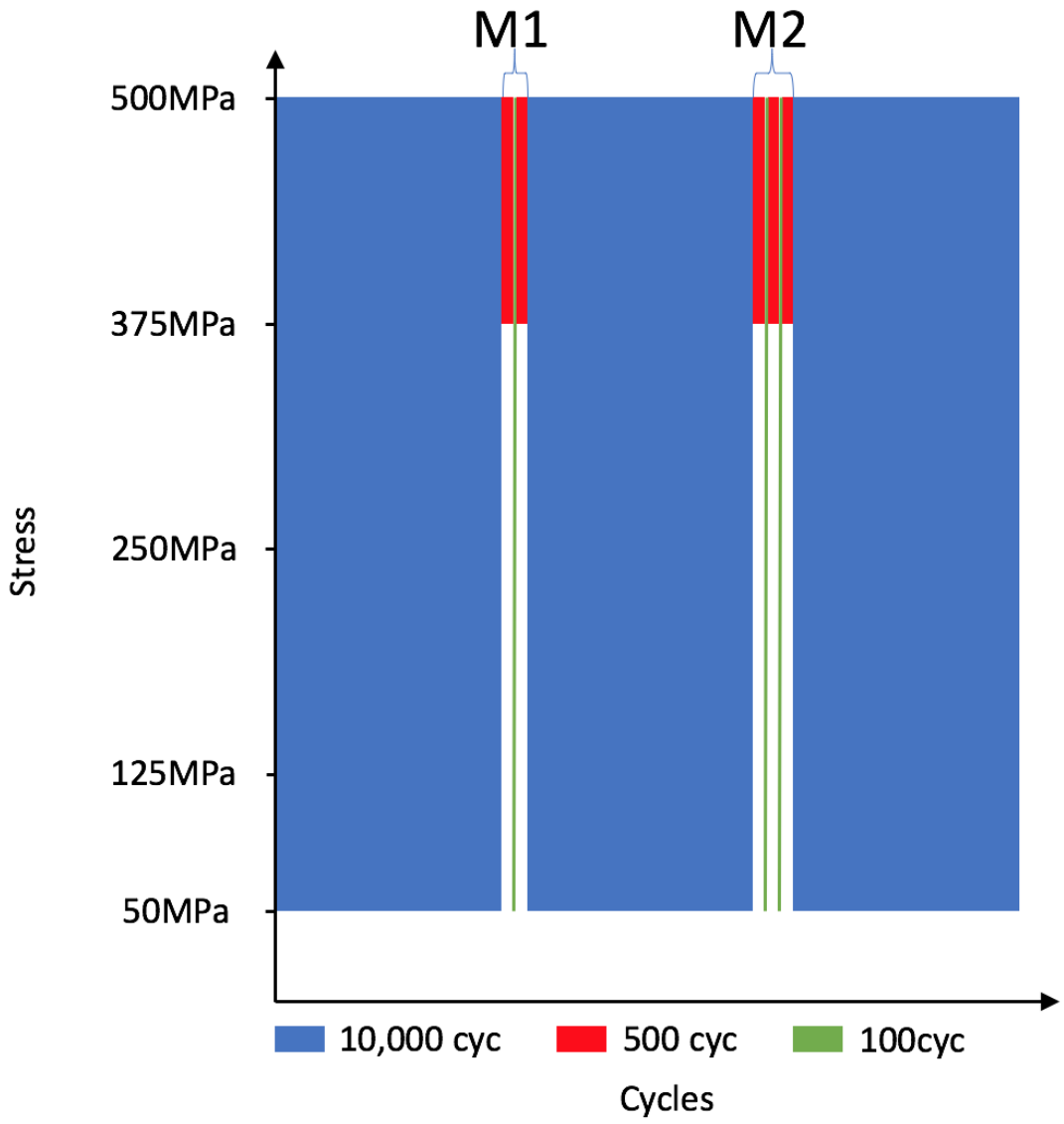


Fig. 6.13. Example of a set of Marker Band fatigue cycles

Fig. 6.14. From top to bottom: design 1 (baseline 5A), design 2 (baseline 6B), design 2 (baseline 3A), design 3 (PHT 9B)

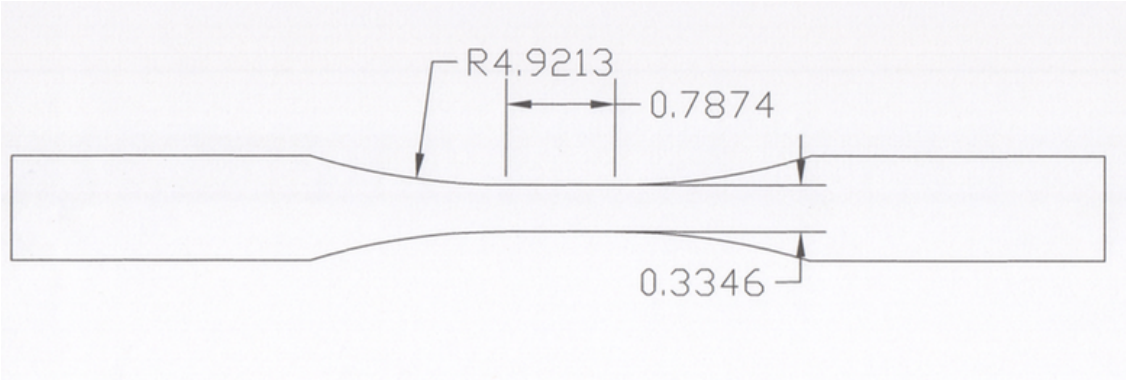


Fig. 6.15. Final Design (3) Dimensions - dimensions in inches

ous tests, the stress was also reduced to around 460 MPa (R=0.1) with a maximum load of 25KN, and final CA Marker Band sequence below:

Note: the below M1 and M2 are for baseline samples, clad samples will have a reduction in primary R=0.1 cycles by half. This cycle will be repeated until failure.

- (M1) 10000 cycles at 46 to 460 MPa (R=0.1),

- (M1) 500 cycles at 347.25 to 460 MPa (R=0.75),
- (M1) 100 cycles at 46 to 460 MPa (R=0.1),
- (M1) 500 cycles at 347.25 to 460 MPa (R=0.75).
- (M2) 10000 cycles at 46 to 460 MPa (R=0.1),
- (M2) 500 cycles at 347.25 to 460 MPa (R=0.75),
- (M2) 100 cycles at 46 to 460 MPa (R=0.1),
- (M2) 500 cycles at 347.25 to 460 MPa (R=0.75),
- (M2) 100 cycles at 46 to 460 MPa (R=0.1),
- (M2) 500 cycles at 347.25 to 460 MPa (R=0.75).

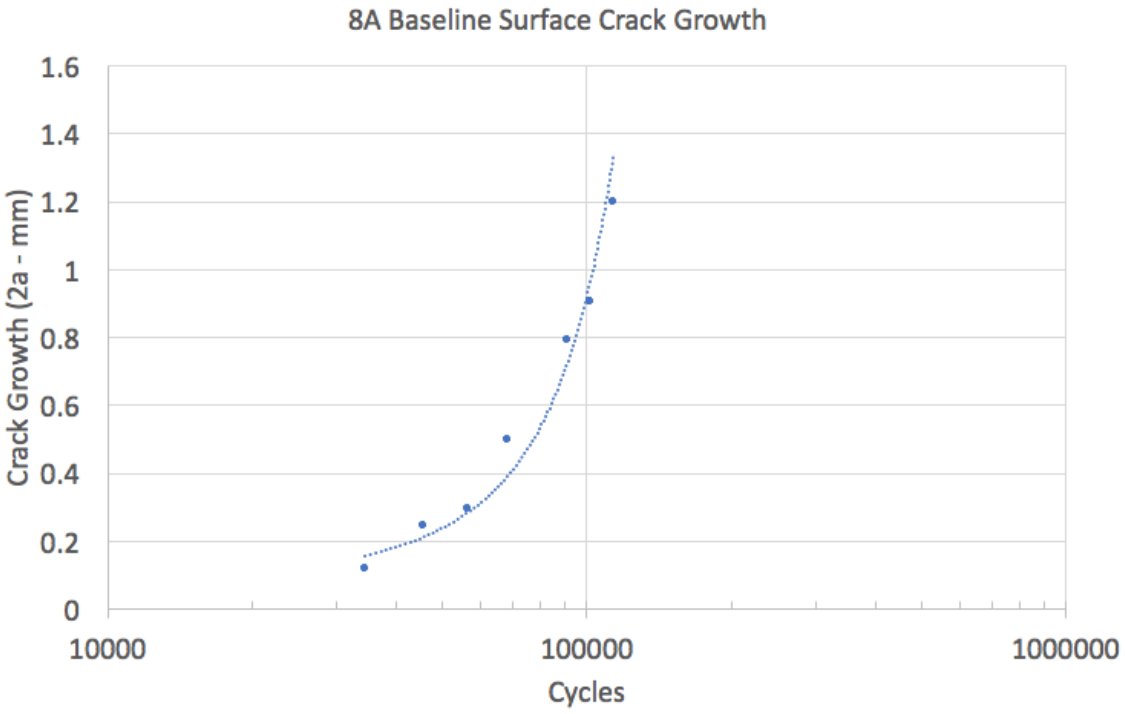


Fig. 6.16. Surface Crack Growth Rate - 8A Baseline

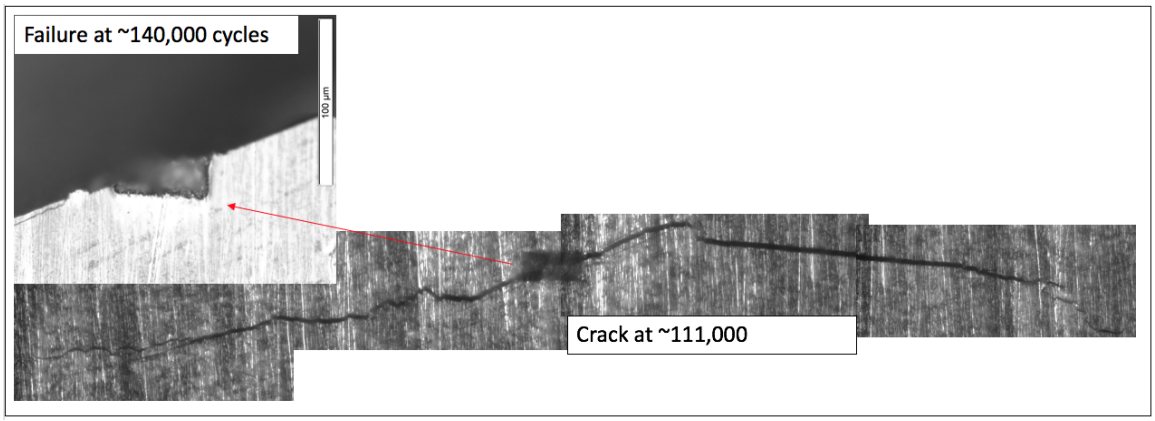


Fig. 6.17. Failure at bottom notch - 8A Baseline

During this test failure occurred (specimen 8A Baseline) at the bottom notch (Figure 6.17). Tracking of the crack front was observed on the surface with images taken roughly every 10,000 cycles (each M cycle); Figure 6.16 is the crack growth tracked from initiation until around 110,000 cycles, failure occurred at 141,939 cycles (the final stages of crack growth were missed due to recording issues).

Due to these promising results, testing was moved onto the clad sample 2B, the first clad sample to be tested. 2B was fatigued until failure at 705,061 cycles, significantly exceeding expectations based on previous tests.

Since more data was required and a greater comparison between each of the specimen conditions, the next test was conducted on a heat treated sample 9B, which failed at 1.28 million cycles, again a significant life increase. Unfortunately crack growth was not tracked from the surface as failure did not occur at the notch and therefore no imagery was available of either 2B or 9B.

A final test was conducted on a further baseline sample 1B, due to the considerable short life of initial baseline test (8A) when compared the repaired samples. 1B failed at 882,808 cycles, unfortunately it failed low on the gauge section at what appears to be the exact point of transition (Figure 6.18). The fractured cross-section was measured to be around 8.65mmx6.35mm (possibility of measurement error due transitional

zone); Figure 6.19 represents the stress vs number of cycles at failure based on failure cross-section.

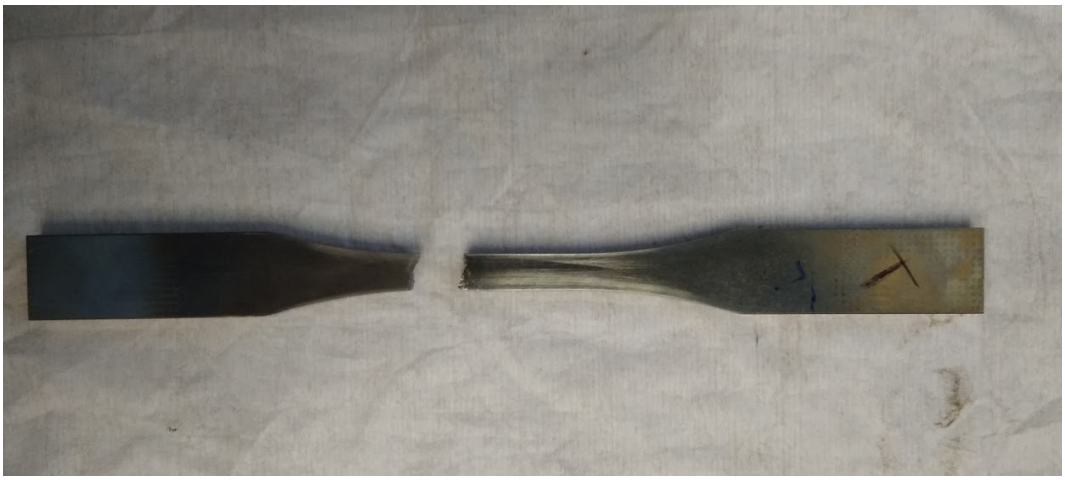

Fig. 6.18. 1B Failure

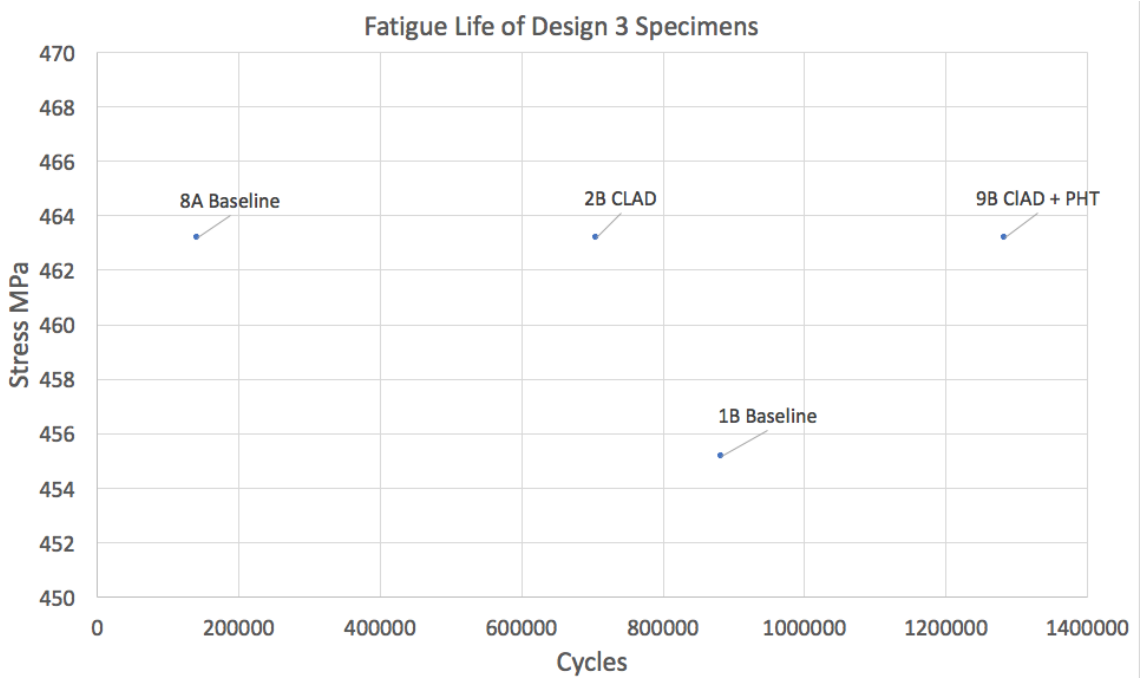


Fig. 6.19. Fatigue Results of D3 Specimens

| Specimen Number | Location of origin within bar stock – 600x60x25 mm | Type | Design | Condition/Tests | Failure Location | Fractography |
|---|---|---|---|---|---|---|
| 1A | Bottom Layer, Edge 1 | As-clad | 1 | | | |
| 1B | Bottom Layer, Edge 1 | Baseline | 3 | Failed - 882808 cyc | Neck/Gauge Transition Below Notches | Potential |
| 2A | Bottom Layer, Centre | PHT | 1 | | | |
| 2B | Bottom Layer, Centre | As-clad | 3 | Failed - 705061 cyc | Gauge Section Below Notches | Limited |
| 3A | Bottom Layer, Edge 2 | Baseline | 2 | Failed - 66329 cyc | Gauge Section Above Notches | Unknown |
| 3B | Bottom Layer, Edge 2 | PHT | 1 | | | |
| 4A | Middle Layer, Edge 1 | As-clad | 1 | EDD | | |
| 4B | Middle Layer, Edge 1 | PHT | 1 | EDD | | |
| 5A | Middle Layer, Centre | Baseline | 1 | EDD | | |
| 5B | Middle Layer, Centre | As-clad | 1 | @Argonne(JUN) | | |
| 6A | Middle Layer, Edge 2 | PHT | Sectioned | Mounted for BSE | | |
| 6B | Middle Layer, Edge 2 | Baseline | 2 | Failed - 51587 cyc | Neck/Gauge Transition Above Notches | Unknown |
| 7A | Top Layer, Edge 1 | As-clad | Sectioned | Mounted for BSE | | |
| 7B | Top Layer, Edge 1 | Baseline | 1 | | | |
| 8A | Top Layer, Centre | Baseline | 3 | Failed - 141939 | Gauge Section Bottom Notch | Surface Cracking Tracked |
| 8B | Top Layer, Centre | PHT | 1 | | | |
| 9A | Top Layer, Edge 2 | As-clad | 1 | | | |
| 9B | Top Layer, Edge 2 | PHT | 3 | Failed - 1283568 | Gauge Section Below Notches | Marker Bands Tracked |

Fig. 6.20. Specimen Summary Table

# 7. FRACTOGRAPHY

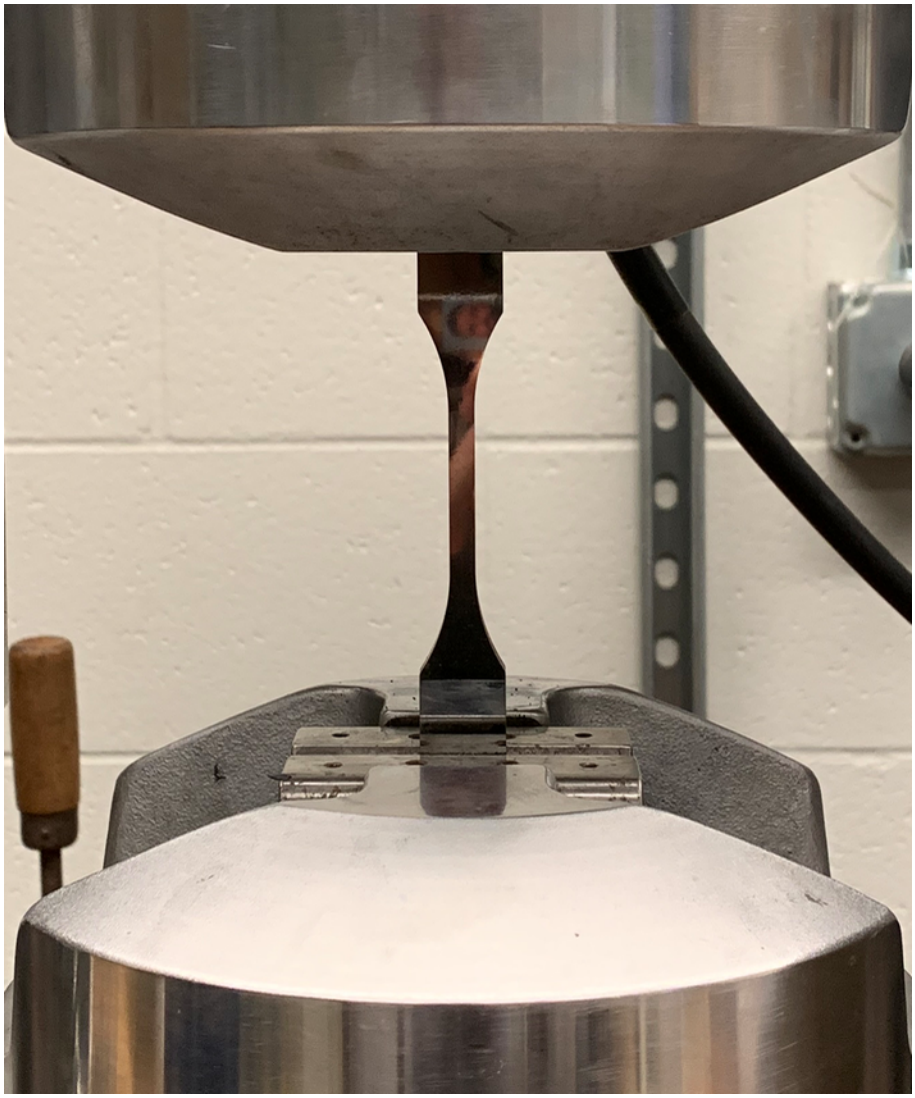

Fig. 7.1. Loaded Specimen - experimental view

Figure 7.1 is the view of a loaded specimen, and represents the perspective of the author when commenting throughout this chapter; each specimen was loaded with the notches, and any clad surface, facing outwards.

Visual analysis of the fracture surface (Figure 7.16) revealed a relatively ductile and tortuous failure mode in specimen 8A; failure occurs towards the front of the sample (at the notch) with the most brittle, planar surface visible and evidence of hinge failure along the rear of the sample with shear lips along both edges. Failure in specimen 8A failed at the bottom notch as observed in the previous chapter.

Regarding clad specimen 2B, failure appears to have occurred along the rear edge of the sample in the substrate, towards the left corner. Again rapid hinge failure was noted along the front edge (clad region) and evidence of shear lips along the right edge. The fracture surface presents a noticeably smoother fracture surface than that of 8A.

9B had the most brittle, planar surface with failure along the left edge of the sample, towards the rear (substrate), with evidence of hinging on the right edge of the sample and shear lips along the front clad edge.

The final test, which acted as a hand-over to the incoming research student, was conducted on specimen 1B. Failure appeared to occur along the left edge of the specimen; unfortunately failure occurred at the transition from the gauge section to the grip in quite a ductile fashion. This could have been due to numerous reasons which will be considered before further testing is conducted; further fractography is recommended to assist with this.

Optical and SEM imagery was conducted on each specimen primarily in search of marker bands in order to quantify crack growth rates which overall proved a significant challenge.

As discussed in the literature review, the intention behind the marker band cycles of M1 and M2 is to produce a visually obvious transition during crack growth. The primary R = 0.1 cycles will produce the largest crack growth which will be interspersed every 10,000 cycles for baseline and 5,000 for clad samples by a varied CA set of R = 0.75 / R= 0.1 amplitudes at 500 / 100 cycles respectively; this variation in CA is intended to produce a set of two stripe (M1; 0.75 / 0.1 / 0.75) and three stripe patterns (M2; 0.75 / 0.1 / 0.75 / 0.1 / 0.75). These sets of stripes are to ensure

that when counting sets of marker bands, a set of bands is less likely to be missed as the observer must ensure the 2-3-2-3 pattern is maintained. This technique replaces previous requirements of counting individual striations.

Due to the short focal range of available optical microscopes analysis of the relatively severe topography proved very challenging, causing great difficulty when it came to identifying any marker bands. To reduce the influence of focal range individual segments of the fracture surface were captured with 100 frames at differing focal lengths in order to build up an image that was post-processed in the tool Fiji-Image J. In order to do this, all 100 images were imported into Image J as an Image Sequence, then plug-in Stack Focuser was utilized which sorted through each image comparatively in order to achieve a single focused image. Some success was had with this technique in regions where smoother transitions of surface were achieved, however since much of the surface had consistently varying height amplitude processing was not always successful. An example of this is shown in Figure 7.3; part (a) is a live image from the microscope, and part (b) is 100 live image stitched together in post processing using Image J. The Olympus BX51M optical microscope has Stream Motion software which was able to perform a similar function to Image J and has produced some of the processed images in this thesis.

Initial images taken optically of the clad sample 2B uncovered what was initially thought to be marker bands; however this was later attributed to rubbing of the fracture surface during the fatigue process (Figure 7.4). This is likely to have occurred during mode 2 shearing during crack closure as the crack propagates.

SEM imagery was conducted on baseline sample 8A, focusing around the known site of crack initiation, the notch (seen in Figure 7.7). SEM settings were as follows throughout fractography imaging;

- Accelerating Voltage: 10.0 kV
- Spot Size: 5.0
- Working Distance: 5 mm (+-0.5mm)

- Aperture: 100$\mu$m

Initial impressions were of potential sites of marker bands, however this was later attributed to dimple rupture, with the lines through the sample potentially being lath acicular alpha boundaries within beta ribs (Figure 7.6). It is believed a marker band was identified near the notch site (Figure 7.5), however it is extremely faint in appearance and does not propagate far along the surface. Due to the low life and thus relatively rapid failure of this specimen, it is possible that due to the relatively small crack growth rate of the marker bands vs surrounding fatigue cycles, they did not display significant contrast (as seen in Figure 7.5)

Post test fractography of 9B PHT provided the most promising case of marker bands as can be seen in Figure 7.8. It is theorised due to the greater longevity of the fatigue experiment and a smoother, brittle fracture, the resultant surface was less severe and therefore fertile ground for observation of clear marker bands.

With initial information from optical imagery, targeted SEM imagery was undertaken with marker bands seen in the optical imagery of Figure 7.8 being identified under SEM. With this as a starting point slow, high zoom, manual scans of the surface up until the free edge was undertaken to identify any further evidence of marker bands. Six obvious sets of marker bands were identified, with more potential examples, however these potential examples were discounted due to lack of consistent pattern and confidence - the closer to the surface the more faint the banding became (as you can see in Figure 7.9). In the opposing direction beyond marker band Set 6 the fracture surface became quite rough and marker bands could no longer be readily identified.

As can be seen in Figure 7.12 a crack growth per cycle was identified by measuring pixels between each marker band using Image J, and comparing this to the pixels along the scale bar in order to gain a length scale. This value was then divided by the cycles between each marker band and a crack growth rate was then identified. In

order to calculate the $\Delta K_1$ the geometry and equation for a penny-wise surface flaw extending radially was taken [62]:

$$\Delta K_1 = \frac{M_f \Delta S \sqrt{\pi a}}{\theta} \sqrt{sec(\frac{\pi a}{2t})} \tag{7.1}$$

Where 1.12 is the front face correction factor $M_f$ for a penny-wise crack [62]. This was compared to the crack growth rate from Metallic Materials Properties Development and Standardization for a Mill-Annealed Plate of Ti-6Al-4V (Figure 7.11); as can be seen the results are quite accurate and produce a good representation of baseline Ti-6Al-4V. When looking at the ΔK comparisons between the R=0.1 and R=0.75 amplitudes, the R=0.75 is 20% of R=0.1, thus explaining the change in crack growth rate and contrast of marker bands on the surface. Marker bands themselves are produced due to a change in surface roughness as can be seen clearly in Figure 7.14. Research has shown that the differences in fracture surface appearance are caused by surface roughness with low ΔK values producing a faceted growth along specific crystallographic planes and high ΔK value producing low roughness as a result of interactions with cyclic plastic zones leading to development of striations [63]. This can be seen when the ΔK values for R=0.75 are plotted against that of R=0.1 (Figure 7.15), with the R=0.75 appearing below the suspected $R_{th}$ based on the simulated experimental data implying Stage 1 Fatigue Crack Growth (FCG). This would imply Mode 2 crack growth which is slip dominated and influenced by microstructure effects with any crack growth growing normal to applied stress (as appears to be the case in Figure 7.14(a)). The ΔK for R=0.1 is likely above $R_{th}$ and is therefore likely experiencing Stage 2 FCG. This will result in Mode 1 dominated crack growth with less microstructure effects and more evidence of plasticity effects causing the activation of alternating slip systems from cyclic tension and compression leading to striations evident on the surface between marker bands (Figure 7.14(b)).

Even though sample 9B had a less tortuous fracture surface, and was more fertile to marker band identification, it still supports other studies which conclude that the fracture surface of Ti-6Al-4V proves a difficult surface to interrogate during fractography due to its lack of available slip planes when compared to other materials [37].

This reduces the likelihood of slip planes aligning, which would have allowed for a greater region of uninterrupted crack growth; the longest uninterrupted marker bands were measured at around 0.5mm across (Figure 7.10) and were often lost in extremely tortuous changes in terrain or fractured surfaces as can be seen in Figure 7.13. The ability to identify marker bands could be eased with more freely available access to equipment such as SEM which provided a great focal range and resolution, however an optical microscope with greater focal range will present a much better combination for identifying and counting marker bands due to its ability to identify variations in fracture surface through reflections of light that an SEM cannot resolve as effectively.

Thoughts regarding why the clad samples both significantly exceeded the baseline sample are drawn from research that has shown that short crack growth is a result of interactions between the crack tip plastic zone and barriers to the plastic flow, i.e. grain boundaries / work hardening, if the stress concentration is not high enough, crack growth in that direction will cease. This could be a potential cause of differing fatigue life in the baseline samples vs the repaired samples. The substrate/baseline material is made up of very course basketweave grains, with prior-$\beta$ grains in the order of up to 800$\mu$m, this can be seen by the large facets on the fracture surface of the material (Figure 7.16) which give the impression of rapid crack growth rates through the course baseline structure with grains de-cohering from each other. Compare this to the much more dense lamellae structure of the clad, these much smaller grains could result in more dislocation growth and grain boundary strengthening preventing further crack propagation and also leading to many changes of direction regarding crack paths. Research into direct laser sintering analysed the potential that decreasing the size of $\beta$ grains in order to decrease the size of microtextured regions and thus increase the performance of the material Ti-6AL-4V by resisting slip between these microtextured regions [5]. When looking beyond the microstructure, based on literature review, the laser clad region is expected to incur tensile stresses from the repair process impacting the fatigue life, this seems to be true when comparing to the heat treated sample. Once heat treatment is applied these residual stresses should

be relaxed and thus the negative impact reduces; based on the tests so far this does appear the case, better understanding of residual stresses would be of great benefit here, a topic of future work.

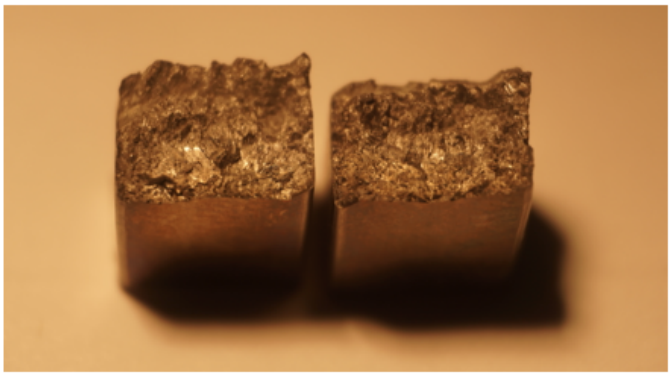

(a) 8A Baseline - 141,939 cyc

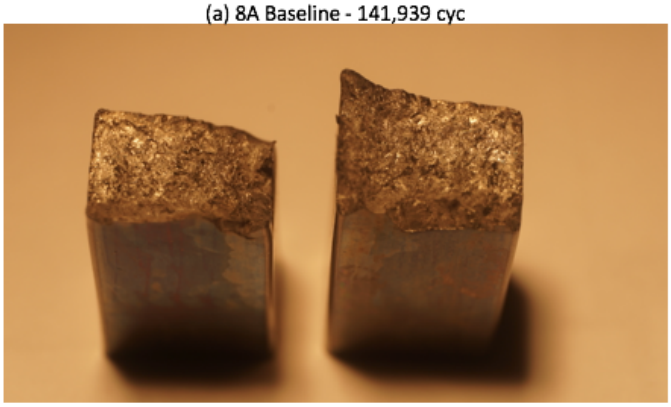

(b) 2B As Clad – 705,061 cyc

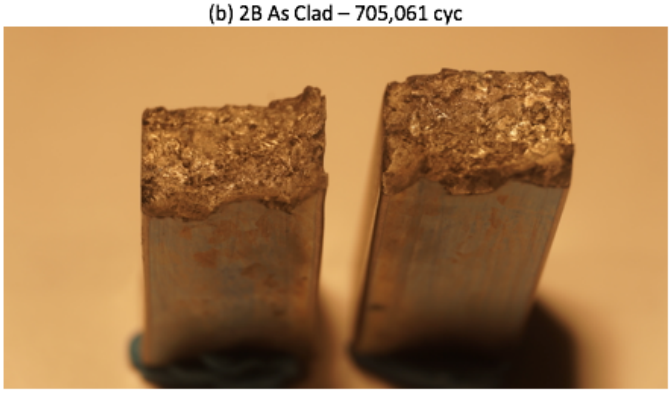

(c) 9B As Clad + PHT - 1,283,568 cyc

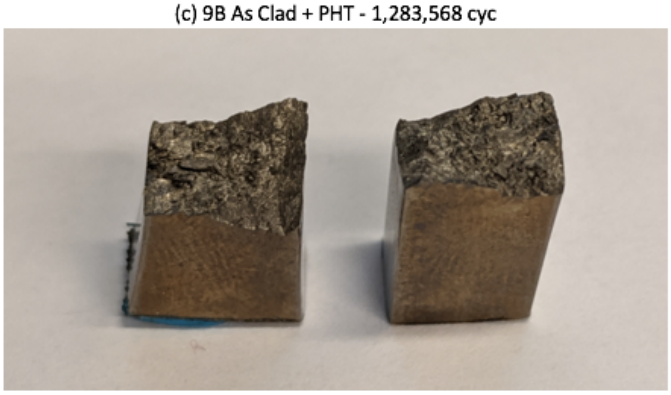

(d) 1B Baseline – 882,808 cyc

Fig. 7.2. Fracture Surface of D3 Specimens. The left sample in each image is the bottom of specimen, clad/notched side is facing forwards. Specimen fracture surface size (a-c) 8.5x6.35mm (d) 8.65x6.35mm

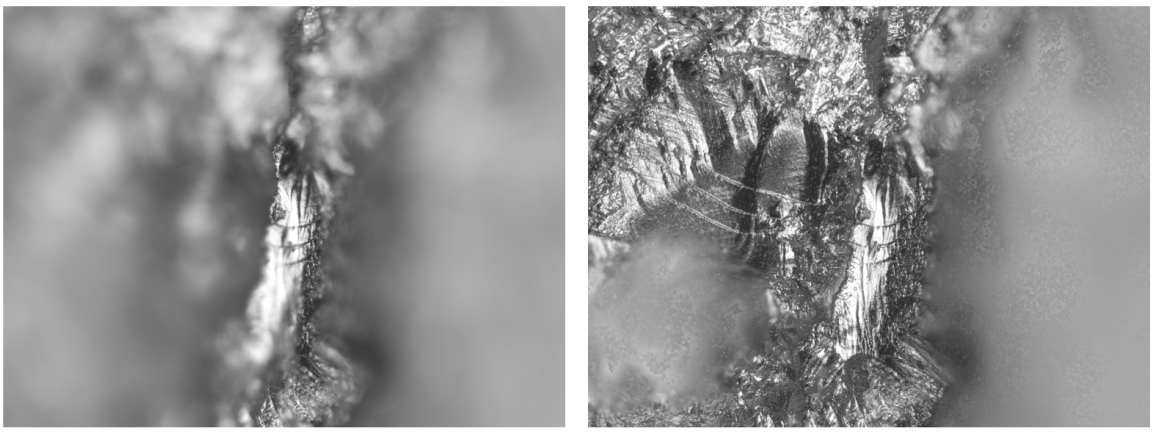

Fig. 7.3. (a) live optical image (b) 100 images stacked

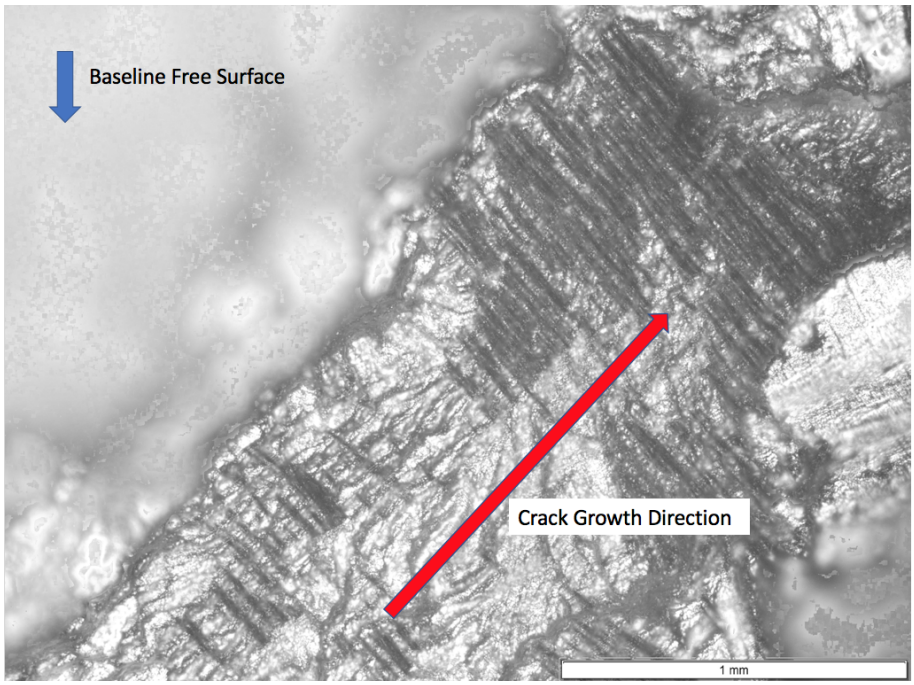


Fig. 7.4. 2B Clad Friction Striations

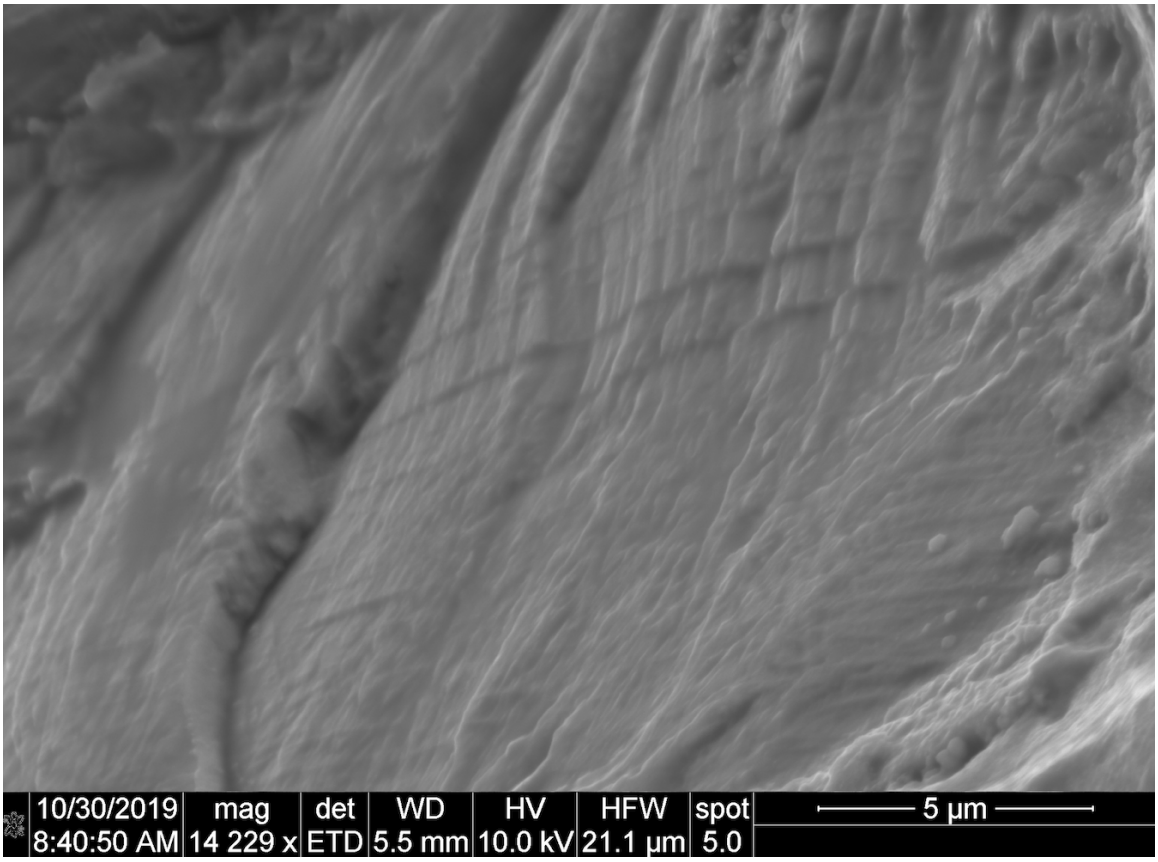


Fig. 7.5. 8A Maker Band

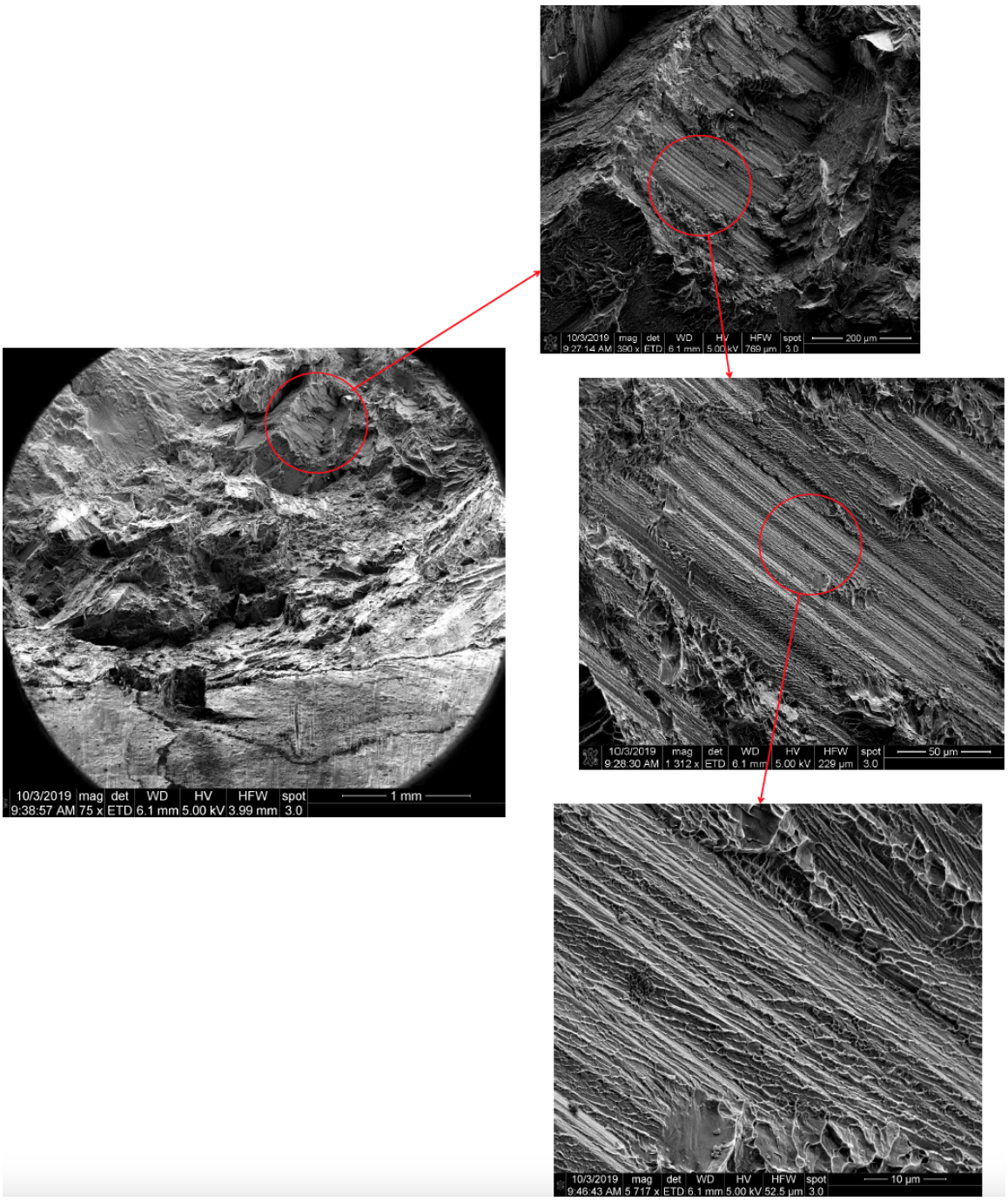


Fig. 7.6. 8A SEM Images

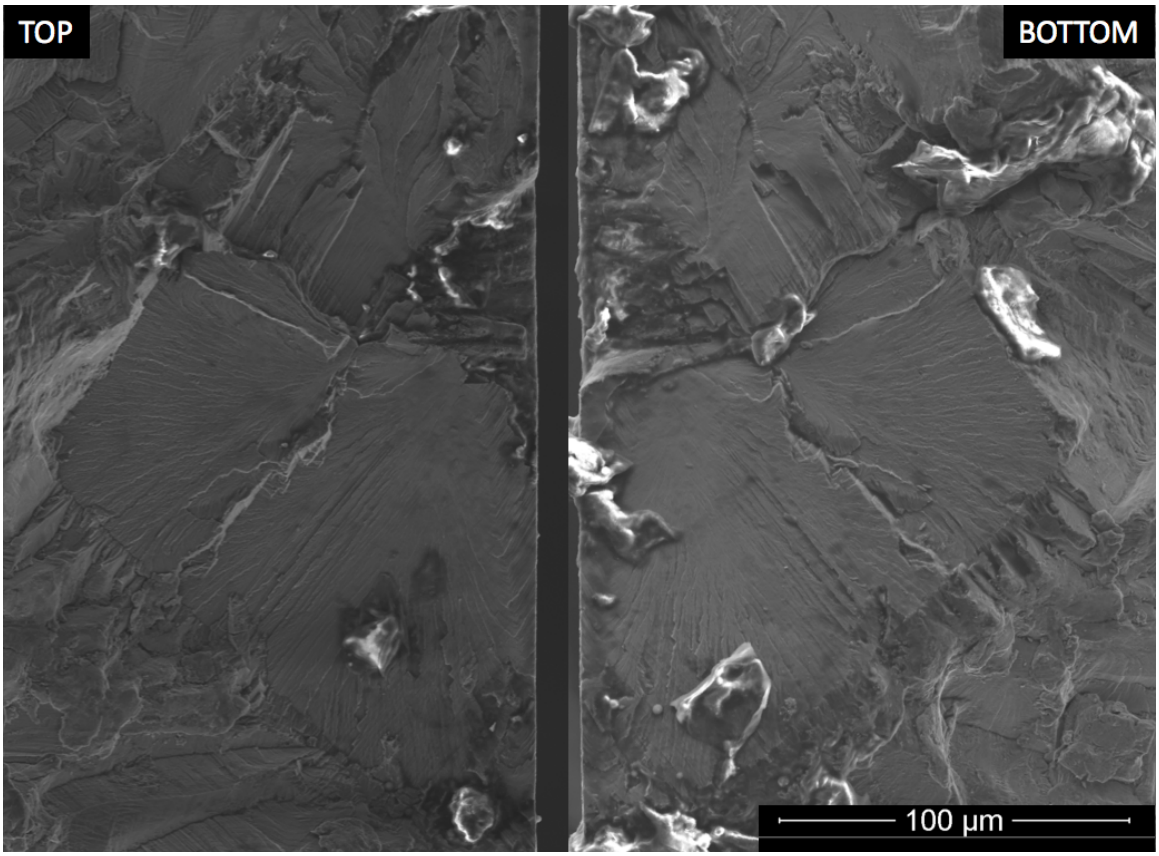


Fig. 7.7. 8A SEM images of notch, top and bottom fracture surface

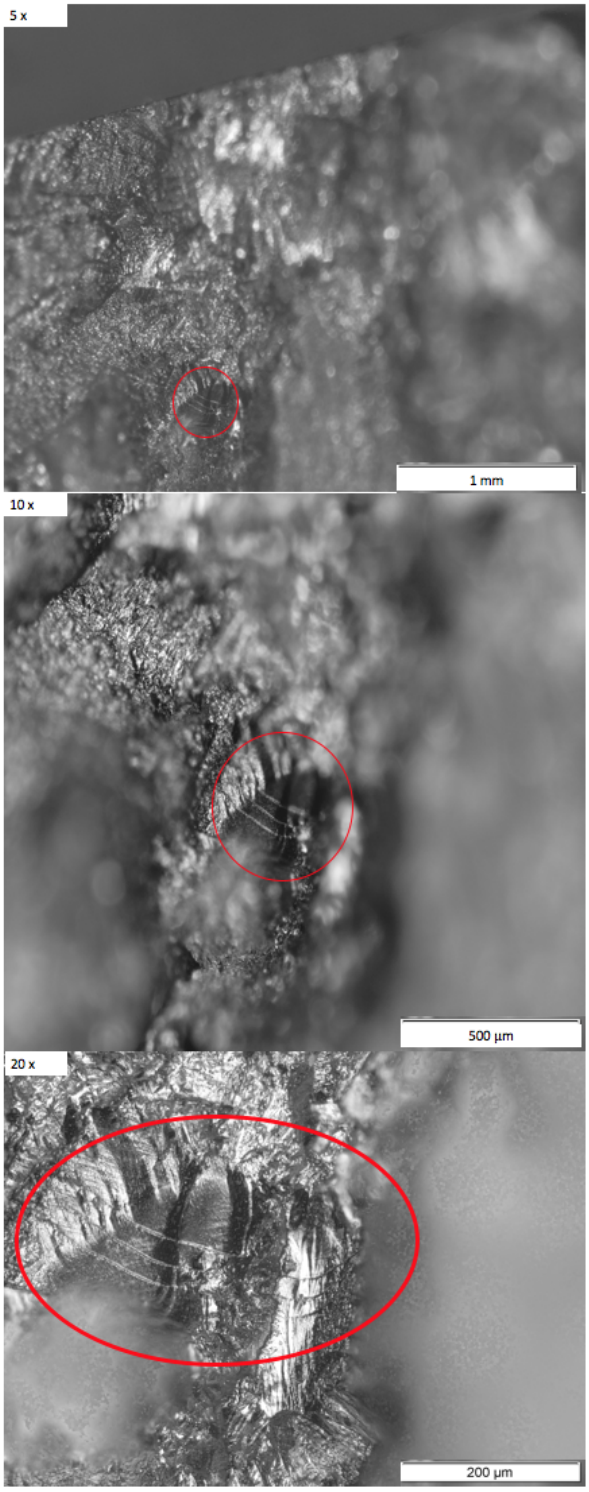


Fig. 7.8. 9B PHT Optical Images

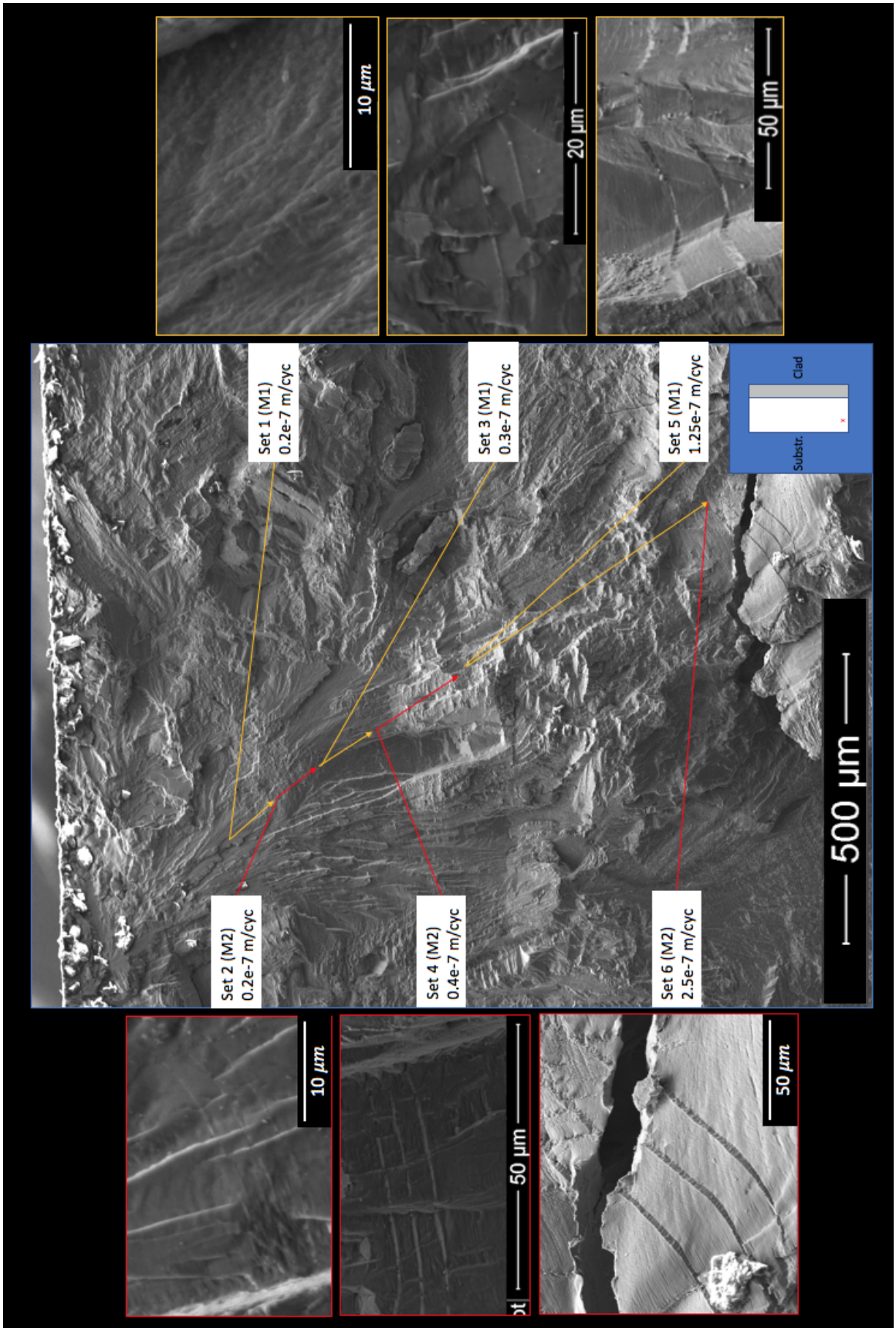


Fig. 7.9. 9B PHT SEM images outlining marker band progression

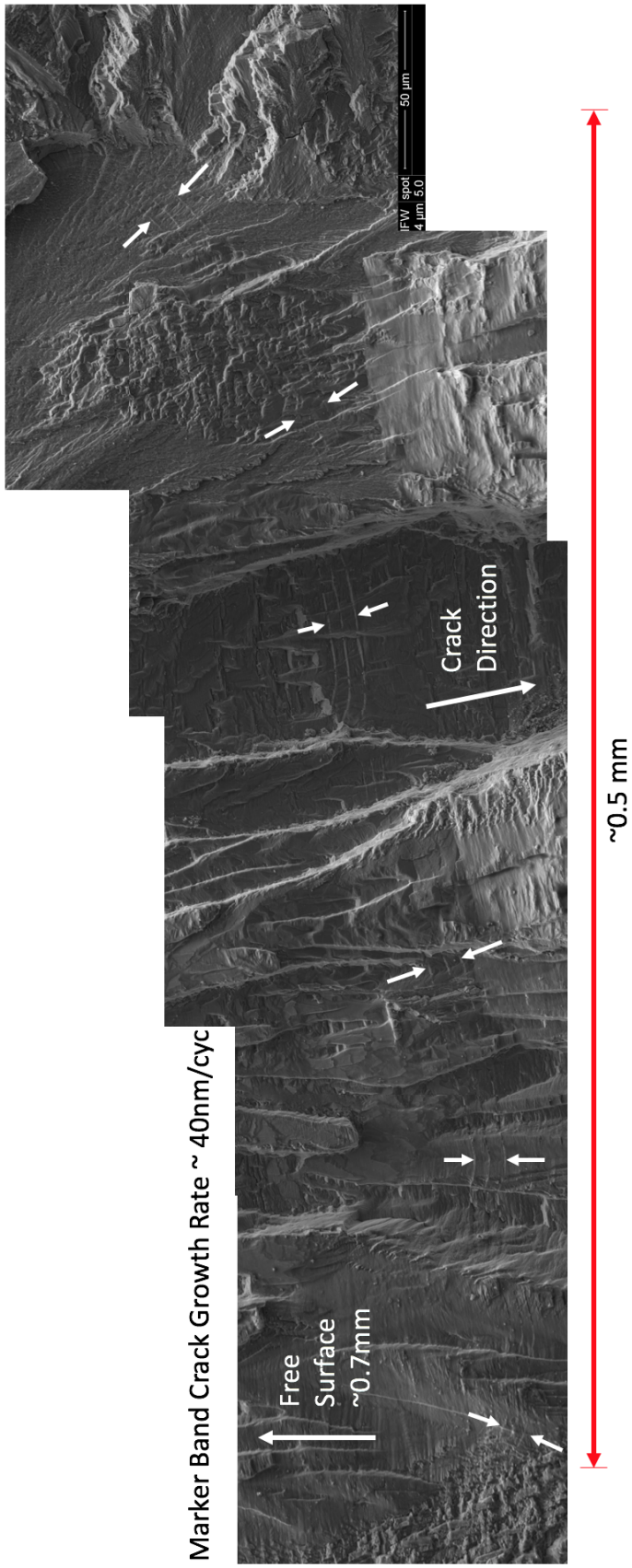


Fig. 7.10. 9B PHT SEM longest continuous marker band (set 4)

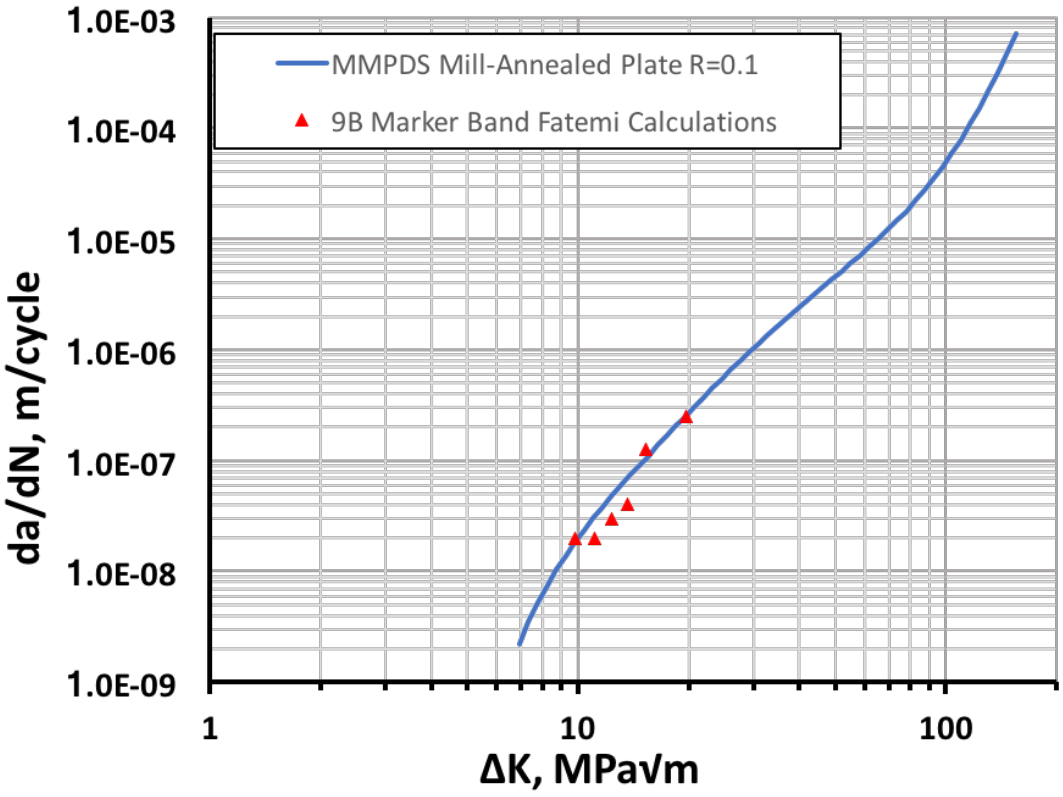


Fig. 7.11. Raw da/dN vs $\Delta$ K and MMPDS Comparison [61]

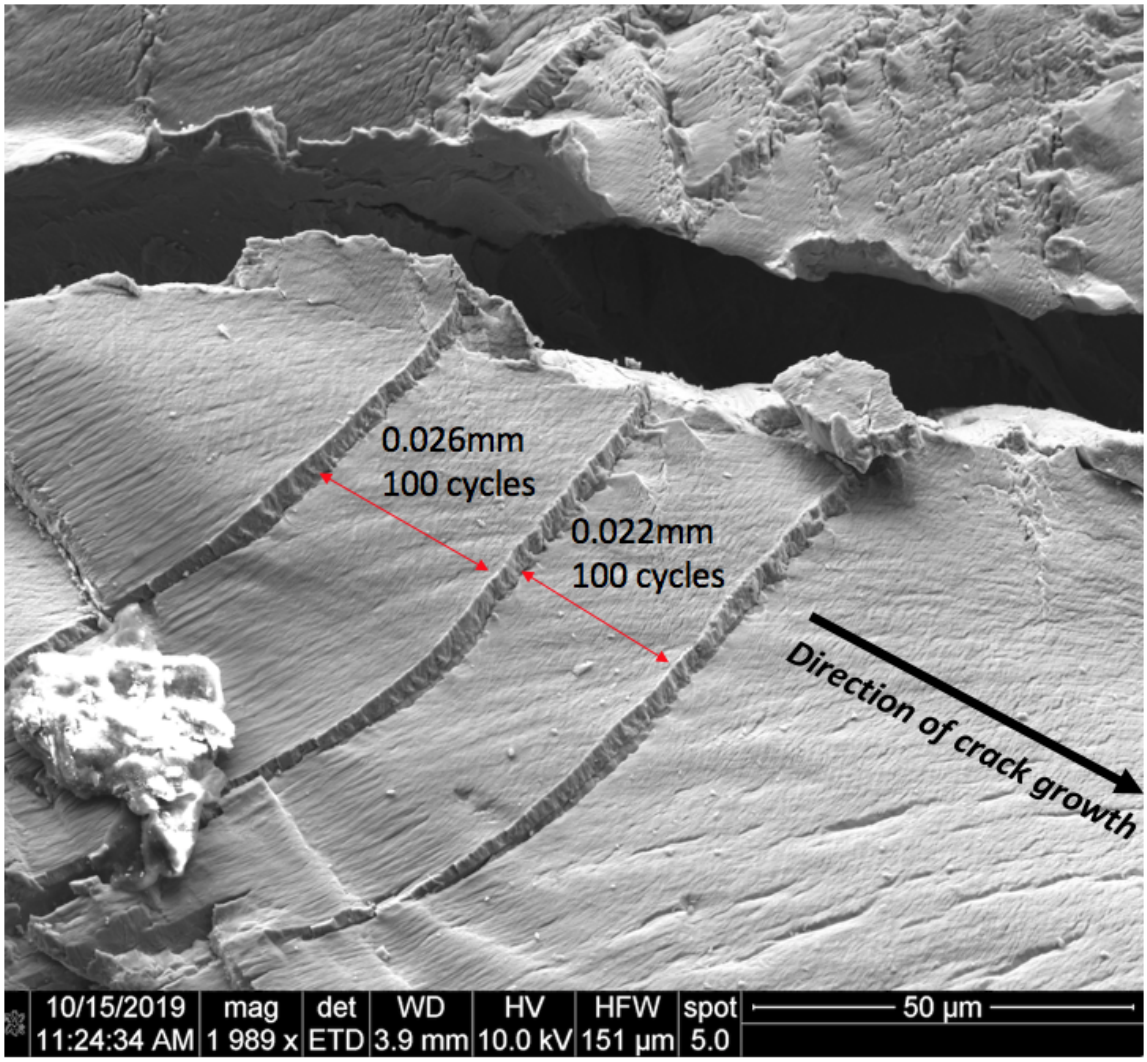


Fig. 7.12. Fuji Image J Measuring Technique

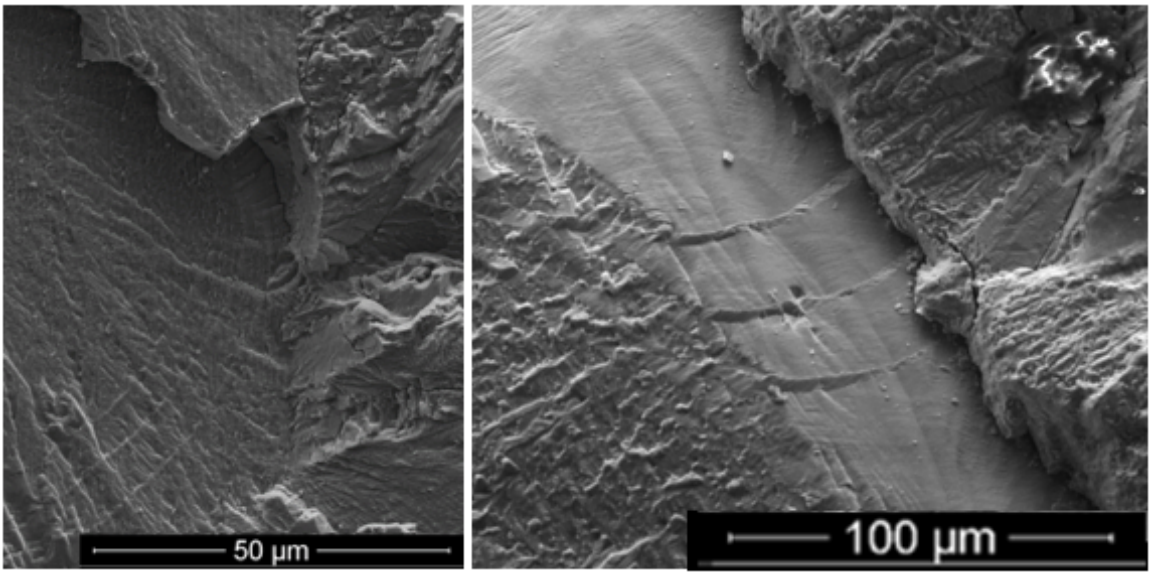


Fig. 7.13. Interrupted MB from specimen 9B [Set 3 (left) and Set 6 (right) from Figure 7.9]

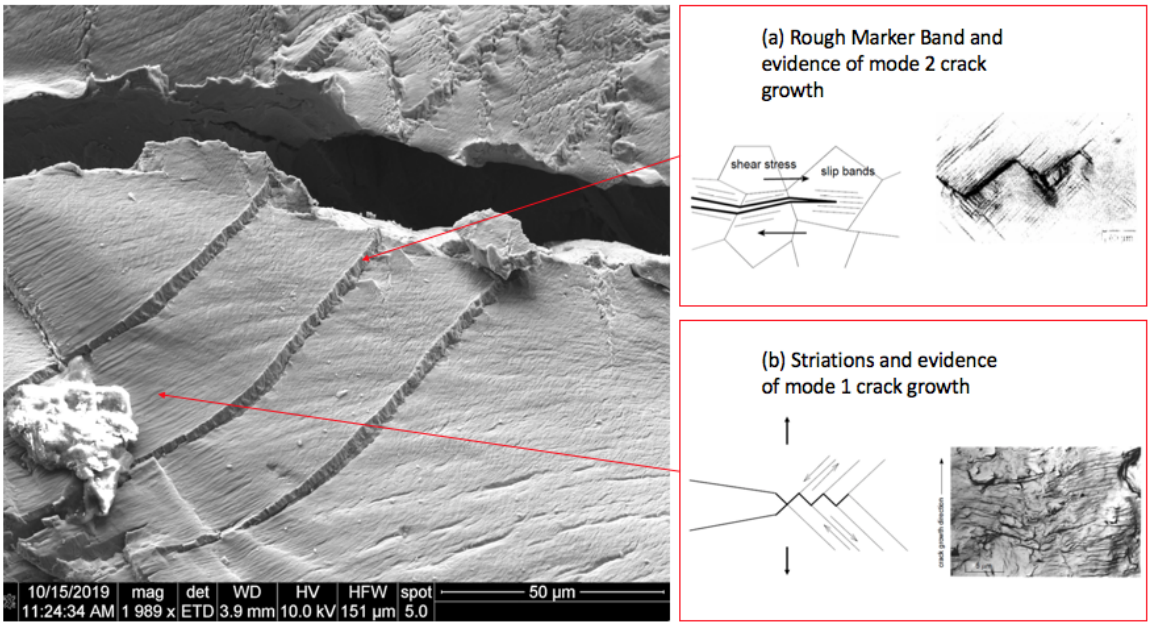


Fig. 7.14. Marker Band Formation [64]

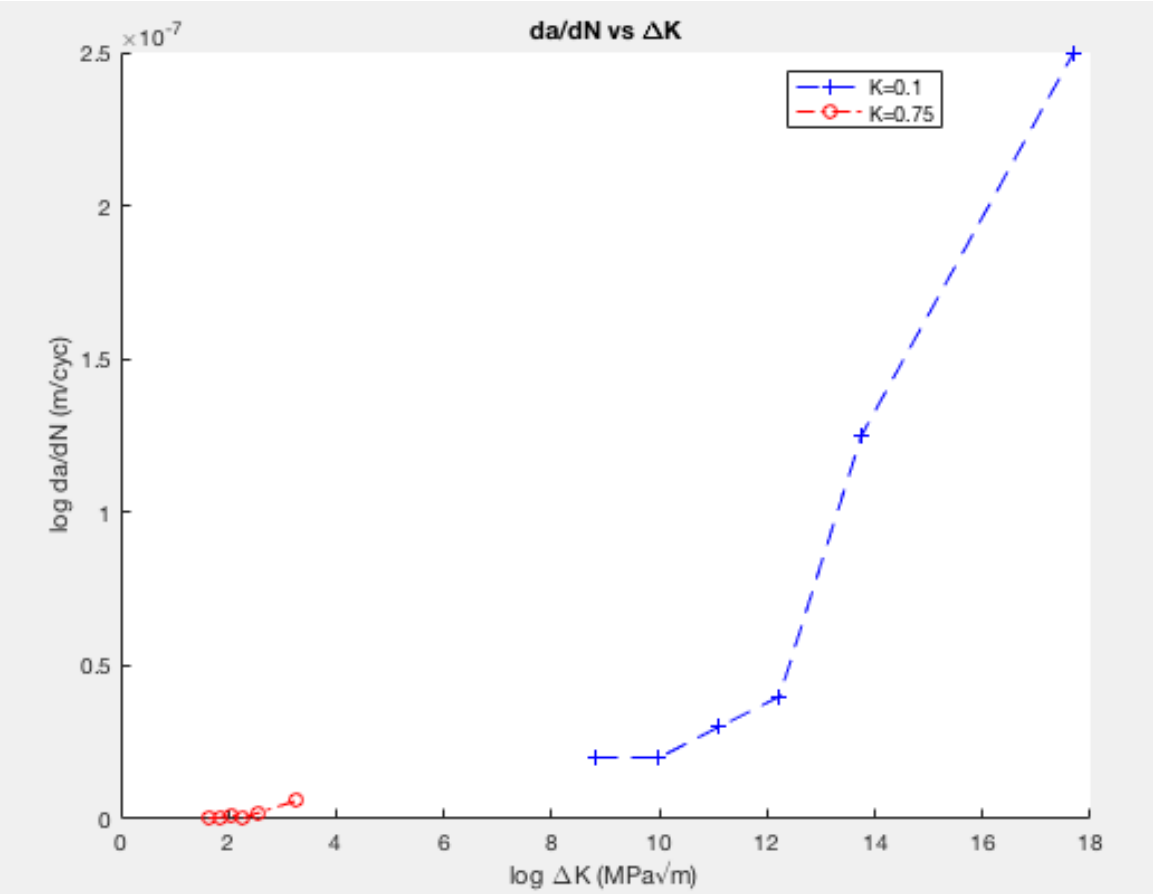


Fig. 7.15. K=0.1 vs K=0.75 of Specimen 9B

Fig. 7.16. 3A Baseline Specimen evidence of large grain facet

# 8. CONCLUSIONS AND FUTURE WORK

This research set out to further the study and understanding of fatigue performance of laser clad Ti-6Al-4V, this was undertaken through several methods; first an understanding of the microstructure was achieved by use of BSE imagery of substrate, clad region and heat treated regions. Through this an understanding of how the substrate's course grain structure compared to the fine grain structure of the clad region, and how little an impact heat treatment had on the microstructure. The second aspect was performance of specimens under tensile fatigue loading. Only four specimens were able to be tested in their final design; two baseline, one clad repaired, and one clad repaired plus heat treated specimen. The clad specimens demonstrated unexpected fatigue performance when compared to the baseline samples with the post heat treated specimen lasting significantly longer than all other specimens. It is theorised that the clad may have contributed to an increase in fatigue resilience due to its finer microstructure, when compared to the softer, more coarse grained substrate; the heat treatment is likely to have relaxed any residual stresses in the clad specimen leading to a reduction in any undesirable residual stresses. Further testing is required to provide more accurate analysis. Marker-bands were utilised throughout testing in order to assess the fracture surface and better understand the fatigue life of the specimens. It was expected, based on previous studies, that post-mortem fractography would be difficult due to titanium's ductile fracture surface and lack of aligned grain orientations due to its fewer favourable slip planes. The clad and heat treated sample, which had the longest fatigue life and most planar fracture surface, provided the best example of how useful the marker-band technique can be at tracking fracture across a surface. Lessons drawn from this process theorise that the longer the fatigue life and thus the more gradual the fracture surface, the increased likelihood of identifying marker-band formation; as this results in longer Stage 2 fatigue crack

growth, which is where marker-bands are most likely to be identified. During Stage 1 marker-bands will be difficult to form and identify due to the increased microstructure effects; during Stage 3, failure is unstable and likely to produce ductile rapid failure making formation and identification of marker-bands very challenging. Additional thoughts regard use of larger gauge sections which would provide more opportunity for marker-bands that have been interrupted by unfavourable grain boundaries to be identified elsewhere on the surface. They also tend to have more planar and less ductile fracture surfaces due to the effect of plane strain dominated fatigue, whereas thinner specimens have shear lips caused by plane stress effects which make fractography extremely difficult. Further research continuing on from this thesis will look at destructive and non destructive techniques that intend to better understand how residual stresses play a role in the specimens fatigue life. Residual stress techniques used during this research were unproductive due to the unexpected coarse microstructure. Further fatigue experiments shall also be undertaken in order to gather more data points and increase opportunity for the study of marker bands in laser clad Ti-6Al-4V.

# REFERENCES

# REFERENCES


[1] P. Swarts, "Air Force Prolongs the Life of the Venerable B-52," *Air Force Times*, 2016.

[2] A. M. Beese and B. E. Carroll, "Review of Mechanical Properties of Ti-6Al-4V Made by Laser-Based Additive Manufacturing Using Powder Feedstock," *Jom*, vol. 68, no. 3, pp. 724–734, 2016.

[3] R. W. S.A. Barter, L. Molent, *Maker Loads for quantitative fractography of fatigue cracks in aerospace alloys*, 2009.

[4] B. Baufeld, E. Brandl, and O. Van Der Biest, "Wire based additive layer manufacturing: Comparison of microstructure and mechanical properties of Ti-6Al-4V components fabricated by laser-beam deposition and shaped metal deposition," *Journal of Materials Processing Technology*, vol. 211, no. 6, pp. 1146–1158, 2011.

[5] T. A. Book and M. D. Sangid, "Strain localization in Ti-6Al-4V Widmanstätten microstructures produced by additive manufacturing," *Materials Characterization*, vol. 122, pp. 104–112, 2016.

[6] R. Cunningham, A. Nicolas, J. Madsen, E. Fodran, E. Anagnostou, M. D. Sangid, and A. D. Rollett, "Analyzing the effects of powder and post-processing on porosity and properties of electron beam melted Ti-6Al-4V," *Materials Research Letters*, vol. 5, no. 7, pp. 516–525, 2017.

[7] R. Jones, J. G. Michopoulos, A. P. Iliopoulos, R. K. Singh Raman, N. Phan, and T. Nguyen, "Representing crack growth in additively manufactured Ti-6Al-4V," *International Journal of Fatigue*, vol. 116, no. February, pp. 610–622, 2018.

[8] Q. Liu, Y. Wang, H. Zheng, K. Tang, L. Ding, H. Li, and S. Gong, "Microstructure and mechanical properties of LMD-SLM hybrid forming Ti6Al4V alloy," *Materials Science and Engineering A*, vol. 660, pp. 24–33, 2016.

[9] E. Toyserkani, *Laser Cladding*, 2005, vol. 53, no. 9.

[10] J. Mazumder and J. Singh, "Laser Surface Alloying and Cladding for Corrosion and Wear." *NATO ASI Series, Series E: Applied Sciences*, vol. 7, no. 115, pp. 297–307, 1986.

[11] F. Lusquiños, A. De Carlos, J. Pou, J. L. Arias, M. Boutinguiza, B. León, M. Pérez-Amor, F. C. Driessens, K. Hing, I. Gibson, S. Best, and W. Bonfield, "Calcium phosphate coatings obtained by Nd:YAG laser cladding: Physicochemical and biologic properties," *Journal of Biomedical Materials Research - Part A*, vol. 64, no. 4, pp. 630–637, 2003.

[12] Q. Liu, M. Janardhana, B. Hinton, M. Brandt, and K. Sharp, "Laser cladding as a potential repair technology for damaged aircraft components," *International Journal of Structural Integrity*, vol. 2, no. 3, pp. 314–331, 2011.

[13] K. F. Walker, J. M. Lourenço, S. Sun, M. Brandt, and C. H. Wang, "Quantitative fractography and modelling of fatigue crack propagation in high strength AerMet®100 steel repaired with a laser cladding process," *International Journal of Fatigue*, vol. 94, pp. 288–301, 2017. [Online]. Available: http://dx.doi.org/10.1016/j.ijfatigue.2016.06.031

[14] G. R. Desale, C. P. Paul, B. K. Gandhi, and S. C. Jain, "Erosion wear behavior of laser clad surfaces of low carbon austenitic steel," *Wear*, vol. 266, no. 9-10, pp. 975–987, 2009.

[15] C. Huang, X. Lin, H. Yang, F. Liu, and W. Huang, "Microstructure and tribological properties of laser forming repaired 34CrNiMo6 steel," *Materials*, vol. 11, no. 9, pp. 1–13, 2018.

[16] N. Hutasoit, V. Luzin, A. Blicblau, W. Yan, M. Brandt, and R. Cottam, "Fatigue life of laser clad hardfacing alloys on AISI 4130 steel under rotary bending fatigue test," *International Journal of Fatigue*, vol. 72, pp. 42–52, 2015. [Online]. Available: http://dx.doi.org/10.1016/j.ijfatigue.2014.11.001

[17] J. M. Lourenço, S. D. Sun, K. Sharp, V. Luzin, A. N. Klein, C. H. Wang, and M. Brandt, "Fatigue and fracture behavior of laser clad repair of AerMet® 100 ultra-high strength steel," *International Journal of Fatigue*, vol. 85, pp. 18–30, 2016.

[18] L. G. S. D. R.L. Sun, D.Z. Yang, "Laser cladding of Ti-6Al-4V alloy with TiC and TiC+NiCrBSi powders," *Surface and Coatings Technology*, vol. 135, no. 2-3, pp. 307–312, 2001.

[19] R. Cottam and M. Brandt, "Laser cladding of Ti-6Al-4V powder on Ti-6Al-4V substrate: Effect of laser cladding parameters on microstructure," *Physics Procedia*, vol. 12, no. PART 1, pp. 323–329, 2011. [Online]. Available: http://dx.doi.org/10.1016/j.phpro.2011.03.041

[20] H. Paydas, A. Mertens, R. Carrus, J. Lecomte-Beckers, and J. Tchoufang Tchuindjang, "Laser cladding as repair technology for Ti-6Al-4V alloy: Influence of building strategy on microstructure and hardness," *Materials and Design*, vol. 85, pp. 497–510, 2015.

[21] X. Zhao, S. Li, M. Zhang, Y. Liu, T. B. Sercombe, S. Wang, Y. Hao, R. Yang, and L. E. Murr, "Comparison of the microstructures and mechanical properties of Ti-6Al-4V fabricated by selective laser melting and electron beam melting," *Materials and Design*, vol. 95, pp. 21–31, 2016. [Online]. Available: http://dx.doi.org/10.1016/j.matdes.2015.12.135

[22] F. Weng, C. Chen, and H. Yu, "Research status of laser cladding on titanium and its alloys: A review," *Materials and Design*, vol. 58, pp. 412–425, 2014. [Online]. Available: http://dx.doi.org/10.1016/j.matdes.2014.01.077

[23] E. M. Birger, G. V. Moskvitin, A. N. Polyakov, and V. E. Arkhipov, "Industrial laser cladding: Current state and future," *Welding International*, vol. 25, no. 3, pp. 234–243, 2011.

[24] B. Graf, A. Gumenyuk, and M. Rethmeier, "Laser Metal Deposition as Repair Technology for Stainless Steel and Titanium Alloys," *Physics Procedia*, vol. 39, pp. 376–381, 2012.

[25] P. A. Kobryn and S. L. Semiatin, "Microstructure and texture evolution during solidification processing of Ti-6A1-4V," *Journal of Materials Processing Technology*, vol. 135, no. 2-3 SPEC., pp. 330–339, 2003.

[26] K. J. Kang, J. H. Song, and Y. Y. Earmme, "Fatigue Crack Growth and Closure Behaviour Through a Compressive Residual Stress Field," *Fatigue & Fracture of Engineering Materials & Structures*, vol. 13, no. 1, pp. 1–13, 1990.

[27] P. S. Song and C. C. Wen, "Crack closure and crack growth behaviour in shot peened fatigued specimen," *Engineering Fracture Mechanics*, vol. 63, no. 3, pp. 295–304, 1999.

[28] M. D. Sangid, J. A. Stori, and P. M. Ferriera, "Process characterization of vibrostrengthening and application to fatigue enhancement of aluminum aerospace components-part I. Experimental study of process parameters," *International Journal of Advanced Manufacturing Technology*, vol. 53, no. 5-8, pp. 545–560, 2011.

[29] P. K. Sharp and G. Clark, "The effect of peening on the fatigue life of aluminium alloys," *Icf 9*, 1997.

[30] S. A. Meguid, "Effect of PartialCoverage Upon the Fatigue Fracture Behaviour of Peened Components," *Fatigue & Fracture of Engineering Materials & Structures*, vol. 14, no. 5, pp. 515–530, 1991.

[31] R. Cottam, V. Luzin, Q. Liu, N. Mathews, Y. Wong, and M. Brandt, "Stress Relief Heat Treatment for Laser Cladding Repair of Ti-6Al-4V Aircraft Components," *AIAC15: 15th Australian International Aerospace Congress*, 2013.

[32] P. Edwards and M. Ramulu, "Fatigue performance evaluation of selective laser melted Ti-6Al-4V," *Materials Science and Engineering A*, vol. 598, pp. 327–337, 2014. [Online]. Available: http://dx.doi.org/10.1016/j.msea.2014.01.041

[33] T. Swift, "Damage tolerance capability," *International Journal of Fatigue*, vol. 16, no. 1, pp. 75–94, 1994.

[34] R. Dainty, "Use of Marker Blocks As An Aid in Quantitative Fractography in Full-Scale Aircraft Fatigue Testing: A Case Study," *Fractography of Ceramic and Metal Failures*, pp. 285–285, 2008.

[35] D. Dawicke, "Overload and Underload Effects on the Fatigue Crack Growth Behavior of the 2024-T3 Aluminum Alloy," 1997. [Online]. Available: http://www.cs.odu.edu/ mln/ltrs-pdfs/NASA-97-cr201668.pdf

[36] P. White, S. A. Barter, and L. Molent, "Observations of crack path changes caused by periodic underloads in AA7050-T7451," *International Journal of Fatigue*, vol. 30, no. 7, pp. 1267–1278, 2008.

[37] M. McDonald, R. Boykett, and M. Jones, "Quantitative fractography markers for determining fatigue crack growth rates in aluminium and titanium aircraft structures," *28th Congress of the International Council of the Aeronautical Sciences 2012, ICAS 2012*, vol. 6, pp. 4996–5005, 2012.

[38] N. Ranganathan, H. Aldroe, F. Lacroix, F. Chalon, R. Leroy, and A. Tougui, "Fatigue crack initiation at a notch," *International Journal of Fatigue*, vol. 33, no. 3, pp. 492–499, 2011. [Online]. Available: http://dx.doi.org/10.1016/j.ijfatigue.2010.09.007

[39] M. Mcdonald and J. Vine, "DST Group developed marker bands for AA7XXX Al alloys," pp. 1–8, 2016.

[40] G. Bussu and P. E. Irving, "The role of residual stress and heat affected zone properties on fatigue crack propagation in friction stir welded 2024-T351 aluminium joints," *International Journal of Fatigue*, vol. 25, no. 1, pp. 77–88, 2002.

[41] G. Pouget and A. P. Reynolds, "Residual stress and microstructure effects on fatigue crack growth in AA2050 friction stir welds," *International Journal of Fatigue*, vol. 30, no. 3, pp. 463–472, 2008.

[42] X. Zhang and Y. Li, "Damage tolerance and fail safety of welded aircraft wing panels," *AIAA Journal*, vol. 43, no. 7, pp. 1613–1623, 2005.

[43] N. Iwashita, "X-ray Powder Diffraction," *Materials Science and Engineering of Carbon*, pp. 7–25, 2016. [Online]. Available: https://linkinghub.elsevier.com/retrieve/pii/B9780128052563000027

[44] M. Vojta, "Reports on Progress in Physics Related content," *Rep. Prog. Phys.*, vol. 59, pp. 1665–1735, 1996.

[45] R. Bandyopadhyay, J. Rotella, D. Naragani, J. S. Park, M. Eff, and M. D. Sangid, "Residual Strain Analysis in Linear Friction Welds of Similar and Dissimilar Titanium Alloys Using Energy Dispersive X-ray Diffraction," *Metallurgical and Materials Transactions A: Physical Metallurgy and Materials Science*, vol. 50, no. 2, pp. 704–718, 2019. [Online]. Available: https://doi.org/10.1007/s11661-018-5034-0

[46] J. C. Mach, C. J. Budrow, D. C. Pagan, J. P. Ruff, J. S. Park, J. Okasinski, A. J. Beaudoin, and M. P. Miller, "Validating a Model for Welding Induced Residual Stress Using High-Energy X-ray Diffraction," *Jom*, vol. 69, no. 5, pp. 893–899, 2017.

[47] C. Genzel, I. A. Denks, J. Gibmeier, M. Klaus, and G. Wagener, "The materials science synchrotron beamline EDDI for energy-dispersive diffraction analysis," *Nuclear Instruments and Methods in Physics Research, Section A: Accelerators, Spectrometers, Detectors and Associated Equipment*, vol. 578, no. 1, pp. 23–33, 2007.

[48] A. Steuwer, J. R. Santisteban, M. Turski, P. J. Withers, and T. Buslaps, "High-resolution strain mapping in bulk samples using full-profile analysis of energy dispersive synchrotron X-ray diffraction data," *Nuclear Instruments and Methods in Physics Research, Section B: Beam Interactions with Materials and Atoms*, vol. 238, no. 1-4, pp. 200–204, 2005.

[49] Y. Choi, "Influence of cladding pattern on the fatigue properties of laser clad Ti-6Al-4V powder on Ti- 6Al-4V substrate."

[50] P. A. Kobryn and S. L. Semiatin, "Mechanical Properties of Laser-Deposited Ti-6Al-4V P.A. Kobryn and S.L. Semiatin Air Force Research Laboratory, AFRL/MLLMP, Wright-Patterson Air Force Base, OH 45433-7817," pp. 179–186, 2013.

[51] M. J. Bermingham, D. Kent, H. Zhan, D. H. Stjohn, and M. S. Dargusch, "Controlling the microstructure and properties of wire arc additive manufactured Ti-6Al-4V with trace boron additions," *Acta Materialia*, vol. 91, pp. 289–303, 2015. [Online]. Available: http://dx.doi.org/10.1016/j.actamat.2015.03.035

[52] Y. Zhai, H. Galarraga, and D. A. Lados, "Microstructure, static properties, and fatigue crack growth mechanisms in Ti-6Al-4V fabricated by additive manufacturing: LENS and EBM," *Engineering Failure Analysis*, vol. 69, pp. 3–14, 2016.

[53] A. Venkataraman, P. A. Shade, R. Adebisi, S. Sathish, A. L. Pilchak, G. B. Viswanathan, M. C. Brandes, M. J. Mills, and M. D. Sangid, "Study of Structure and Deformation Pathways in Ti-7Al Using Atomistic Simulations, Experiments, and Characterization," *Metallurgical and Materials Transactions A: Physical Metallurgy and Materials Science*, vol. 48, no. 5, pp. 2222–2236, 2017.

[54] M. Paridah, A. Moradbak, A. Mohamed, F. a. t. Owolabi, M. Asniza, and S. H. Abdul Khalid, "We are IntechOpen , the world s leading publisher of Open Access books Built by scientists , for scientists TOP 1 %," *Intech*, vol. i, no. tourism, p. 13, 2016.

[55] T. Ahmed and H. J. Rack, "Phase transformations during cooling in $\alpha + \beta$ titanium alloys," *Materials Science and Engineering A*, vol. 243, no. 1-2, pp. 206–211, 1998.

[56] J. Yang, H. Yu, J. Yin, M. Gao, Z. Wang, and X. Zeng, "Formation and control of martensite in Ti-6Al-4V alloy produced by selective laser melting," *Materials and Design*, vol. 108, pp. 308–318, 2016.

[57] W. Xu, M. Brandt, S. Sun, J. Elambasseril, Q. Liu, K. Latham, K. Xia, and M. Qian, "Additive manufacturing of strong and ductile Ti-6Al-4V by selective laser melting via in situ martensite decomposition," *Acta Materialia*, vol. 85, pp. 74–84, 2015.

[58] A. Standard, "Standard Test Method for Microindentation Hardness of Materials," *The Biology of the Xenarthra*, 2019.

[59] ASTM, "Standard practice for verification of testing frame and specimen alignment under tensile and compressive axial force application." *E1012 - 14*, vol. i, pp. 1–18, 2013.

[60] M. T. S. Series, "MTS Series 793 Tuning and Calibration."

[61] R. C. Rice, J. L. Jackson, J. Bakuckas, and S. Thompson, "Metallic Materials Properties Development and Standardization (MMPDS)," no. January, pp. 1–58, 2013.

[62] R. I. R. I. Stephens and H. O. H. O. Fuchs, "Metal fatigue in engineering," p. 472, 2001.

[63] D. Petersen, C. Ragazzo, R. Hertzberg, and R. Jaccard, "A Method for Generating Fatigue Marker Bands Using a Constant Kmax Test Procedure," *Journal of Testing and Evaluation*, vol. 23, no. 1, p. 19, 1995.

[64] D. Socie and G. Marquis, "Multiaxial Fatigue." SAE International, 2000, p. 502.